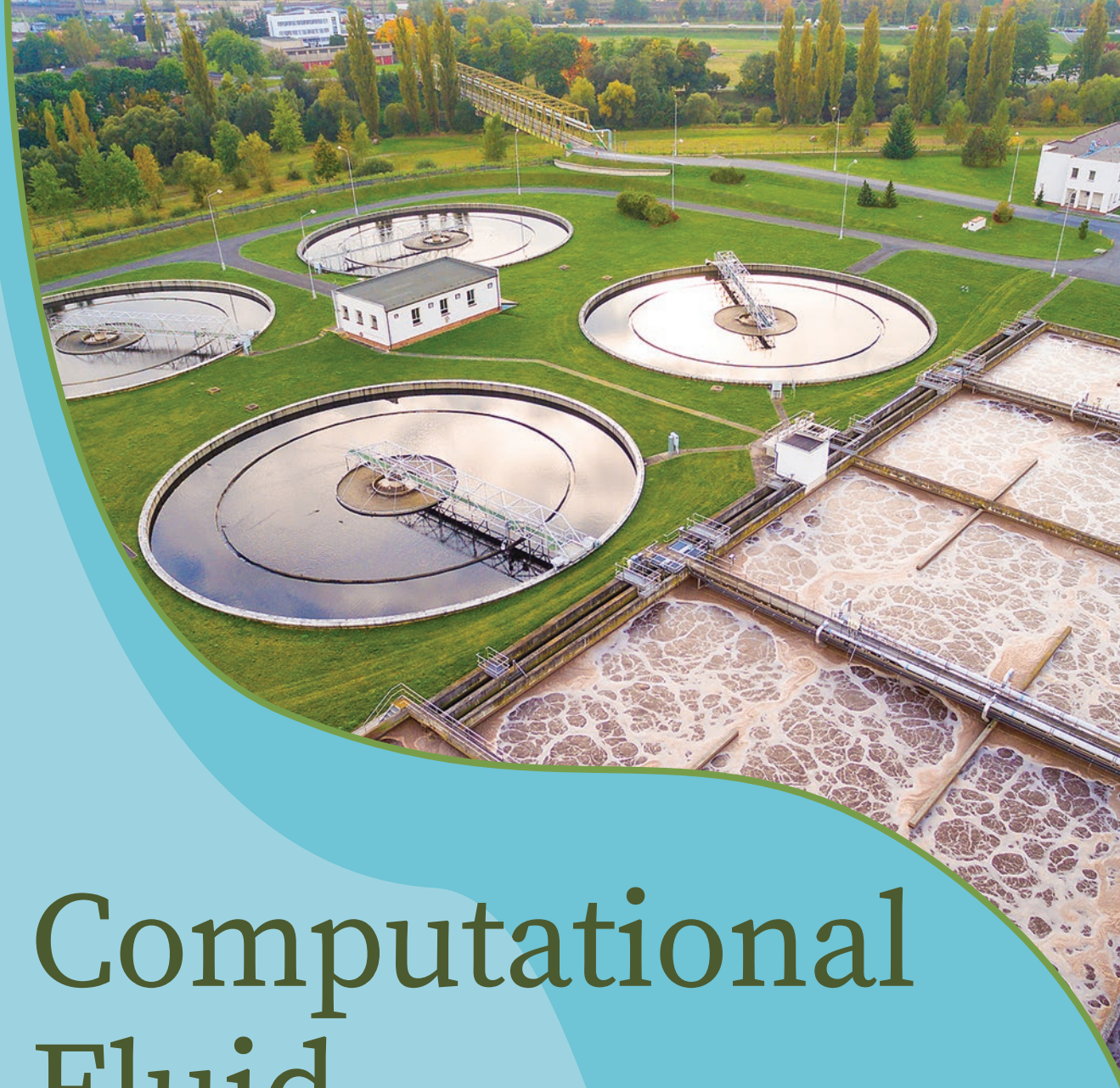

Computational Fluid Dynamics

Applications in Water, Wastewater, and Stormwater Treatment

Computational Fluid Dynamics
Task Committee

EDITED BY

Xiaofeng Liu, Ph.D., P.E. and Jie Zhang, Ph.D.

ASCE

EWRI
ASCE
ENVIRONMENTAL & WATER RESOURCES INSTITUTE

Computational Fluid Dynamics

Applications in Water, Wastewater, and Stormwater Treatment

EWRI Computational Fluid Dynamics Task Committee

Edited by
Xiaofeng Liu Ph.D., P.E.
Jie Zhang Ph.D.

Sponsored by
Water Supply, Treatment and Distribution Engineering Committee and
Water, Wastewater & Stormwater Council of the
Environmental and Water Resources Institute of the
American Society of Civil Engineers

Published by the American Society of Civil Engineers

Library of Congress Cataloging-in-Publication Data

Names: Liu, Xiaofeng, 1977– editor. | Zhang, Jie, 1986– editor.
Title: Computational fluid dynamics : applications in water, wastewater, and stormwater treatment : EWRI computational fluid dynamics task committee / edited by Xiaofeng Liu, Ph.D., PE, Jie Zhang, Ph.D. ; sponsored by The Water Supply, Treatment and Distribution Engineering Committee and The Water, Wastewater & Stormwater Council of The Environmental and Water Resources Institute of The American Society of Civil Engineers.
Description: Reston, Virginia : American Society of Civil Engineers, [2020] | Includes bibliographical references and index.
Identifiers: LCCN 2019007194 | ISBN 9780784415313 (print : alk. paper) | ISBN 9780784482216 (pdf)
Subjects: LCSH: Environmental hydraulics–Fluid dynamics–Data processing. | Computational fluid dynamics. | Sewerage–Fluid dynamics–Data processing. | Storm sewers–Fluid dynamics–Data processing.
Classification: LCC TC163.5 .C67 2020 | DDC 628.1/62–dc23
LC record available at https://lccn.loc.gov/2019007194

Published by American Society of Civil Engineers
1801 Alexander Bell Drive
Reston, Virginia 20191-4382
www.asce.org/bookstore | ascelibrary.org

Errata: Errata, if any, can be found at https://doi.org/10.1061/9780784415313.

ISBN 978-0-7844-15-31-3 (print)
ISBN 978-0-7844-8221-6 (PDF)

Manufactured in the United States of America.

25 24 23 22 21 20 19 1 2 3 4 5

Contents

Preface

Background and History

Computational fluid dynamics (CFD) has proven to be a valuable and sometimes indispensable tool for designing new and retrofitting existing water and wastewater systems. The availability of ever-increasing computing power further spurs the adoption of CFD in engineering practice and academic research for water infrastructure. However, traditional design methods, which heavily depend on empirical formulas and scaled physical models, still prevail in most engineering projects. CFD models are mostly used as a side exercise to complement traditional design methods, mostly because of the culture of relying on proven methods in a traditional field, such as water and wastewater treatment. This situation occurs also because of the lack of proper training of engineers, at school and on the job alike, thus resulting in fewer CFD experts in the water and wastewater community than in other fields, such as mechanical engineering and the aerospace industry. Therefore, the purpose of this book, which we refer to as a primer, is to introduce CFD to the water and wastewater engineering community and to provide a general overview of what it is and how it can be used.

Promoting CFD in the water and wastewater treatment community, as in many other traditional fields, is a challenge. I have been teaching water resources engineering and environmental hydraulics at several institutions for the past 10 years, and I have observed that typical civil and environmental engineering programs do not include advanced computational fluid modeling in their undergraduate curricula. At most, students are only exposed to basic numerical techniques, such as the finite difference method. CFD courses in civil and environmental graduate programs are also rare. Even after school, engineers do not have many opportunities to find training on CFD since there are not many training and educational opportunities available.

Despite the slow pace of the adoption of CFD in the water and wastewater industry, people are beginning to realize the value of such computational tools. CFD is being used more often in practice; therefore, there is a need for training in and promotion of CFD in the water community. With this backdrop, a group of researchers and practitioners conceived the idea of forming a technical committee within ASCE's Environmental and Water Resources Institute. One of the goals of the committee was to produce this book to be used by water engineers and designers.

The content and the level of detail in the primer went through several iterations of revisions, based on input from members of the technical committee and others who participated in several workshops. Workshops were held

concurrently at two EWRI World Congress conferences and one at ASCE headquarters. The committee reached the consensus that the primer, as its name implies, should include general procedures for conducting flow, transport, and reaction simulations using CFD and specific examples in water and wastewater treatment applications. Considering the training that most water engineers acquired in school, this book assumes prior knowledge of numerical analysis and computational methods as a minimum. On the other hand, sufficient details and references are included to facilitate the proper use of CFD.

A signature characteristic of this primer is that examples are provided, including the input files and part of the results. Engineers can follow the detailed examples and ultimately be able to adapt one or more of these examples to solve their own problems of interest. The original plan was to use open-source or public domain CFD codes exclusively for this book. The reason is obvious: Not everyone has access to commercial CFD software, and the fee for a license can be a heavy financial burden. However, during the development of this primer, committee members, especially those who did have commercial CFD software licenses and have used them in their work, contributed their cases as examples. As a result, the application examples in this book use a mix of open-source and commercial software.

The committee hopes that this primer will grow interest and build a community. Over time, we anticipate that CFD will gain in popularity and acceptance for water and wastewater treatment design.

About the Task Committee

This ASCE EWRI Task Committee was formed in 2015 with the name Computational Fluid Dynamics Applications in Water and Wastewater Treatment under the Water Supply, Treatment and Distribution Engineering Committee and the Water, Wastewater, and Stormwater Council. Jie Zhang, a researcher at South Florida University at the time, was the chair from the beginning to 2017. Then, I became the chair in 2017. We have about 20 active members who have participated in various technical activities since the inauguration of the committee, including regular online meetings, workshops, and training courses. The composition of the committee is almost half from industry and half from academia. Many of the members directly contributed to the writing of chapters of this book or served as technical reviewers. As in many other ASCE committees, almost all members volunteered their personal time to this cause because of their passion and dedication to their profession.

This task committee aims to provide civil and environmental engineers guidance on when and how to use computational fluid dynamics in solving fluids-related problems for water and wastewater treatment design. Two objectives were proposed: (1) to develop a primer on computational fluid dynamics (CFD) applications in water and wastewater treatment, and (2) to promote CFD tools in the water and wastewater treatment community by disseminating the primer and organizing workshops and webinars. With the publication of this primer, the first objective has been met. The second objective has partially been met, as evidenced by the past workshops and planned training courses and webinars.

The following is a brief account of the committee work since the beginning, which led to the publication of this book and beyond.

- *October 2015–January 2016*: The committee identified water and wastewater treatment technologies for which CFD has been applied or has the potential to be applied through literature review, field practitioner surveys, and task committee discussions. A tentative outline of the primer was developed.
- *February 2016–May 2016*: Subtask committees were established, and members were assigned based on their interests and expertise. Subcommittee leaders were also appointed. Furthermore, a technical session on CFD applications in water and wastewater engineering was organized at the 2016 EWRI World Congress. During the congress, feedback was collected from other EWRI attendees not on our task committee.
- *June 2016–December 2016*: Regular online meetings were held involving all task committee members. Committee members communicated with engineers who have solved water and wastewater engineering problems using CFD tools. A draft primer was developed with case studies.
- *January 2017–May 2018*: The draft of the primer was submitted to the Water Supply, Treatment and Distribution Engineering Committee and the Water, Wastewater, and Stormwater Council for reviews. The primer was finalized and submitted to ASCE for publication. A workshop and panel discussion were organized at the 2017 EWRI World Congress to promote the primer and the use of CFD tools in water and wastewater treatment design. The task committee also discussed the possibility of extending the primer to a manual of practice.

The task committee has disseminated the primer by publishing a summary version through the ASCE website and by organizing webinars. The full version of the primer is available through the Civil Engineering Database of ASCE. In the future, depending on the feedback from the water and wastewater community, the task committee may further develop a manual of practice on this topic.

Organization of This Book

The book is organized into five parts, each of which has several chapters written by individual committee members. The following is a short summary of each part.

- **Part 1: Physical, Chemical, and Biological Processes in Water, Wastewater, and Stormwater Treatment.** This part provides a succinct overview of the processes occurring at most treatment facilities. These processes, ranging from physical transport to chemical and biological reactions, and the corresponding mathematical models, constitute the technical backbone of this primer. Readers are expected to know some general concepts of these treatment processes and can connect the mathematical equations with the underlying physics, chemistry, and biology.
- **Part 2: Fundamentals of Computational Fluid Dynamics.** CFD itself is an area with rich content covering fluid dynamics, numerical methods,

turbulence and modeling, software engineering, and parallel computation. The chapters in this part provide a brief introduction to the background, basic processes and steps, and analysis involved in typical CFD studies.

- **Part 3: Water Treatment Technologies and CFD Application Case Studies.** Chapters covering different water treatment processes, that is, aeration, sedimentation, ozone disinfection, pumping, and flow distribution, present example applications frequently encountered in water treatment. These processes may also be used in wastewater and stormwater treatment.
- **Part 4: Wastewater Treatment Technologies and CFD Application Case Studies.** Chapters covering typical processes in wastewater treatment, that is, activated sludge tanks, water stabilization ponds, algae raceway ponds, and UV disinfection, showcase how CFD can be used to evaluate wastewater treatment efficiency.
- **Part 5: Stormwater Treatment Technologies and CFD Application Case Studies.** Chapters were included to cover collection, filtration, particle separation, and geysering (transient) processes to promote efficiency and safety of stormwater collection, treatment, usage, and disposal.

Parts 1 and 2 are the foundations for both the treatment process and CFD; Parts 3, 4, and 5 demonstrate how CFD can be used to simulate various aspects of water, wastewater, and stormwater treatment with the presentation of case studies. The reader may review the chapters in the presented order for a more comprehensive view of the CFD field or may select chapters to review specific topics of interest.

The companion cases for Parts 3, 4, and 5 (Chapters 9 to 23) can be downloaded from https://doi.org/10.4211/hs.344350caa2e341f5a8a9eb33cbed3f78

Xiaofeng Liu, Ph.D., P.E.
Task Committee Chair

Acknowledgments

Xiaofeng Liu, Ph.D., *Task Committee Chair*
Pennsylvania State University
Jie Zhang, Ph.D., *Past Chair*
Carollo Engineers, Inc.
Carrie L. Knatz, P.E., *Secretary*
CDM Smith

Task Committee Members

Hamid Bashiri Atrabi
Tarek Aziz
Rene A. Camacho
Yovanni A. Catano-Lopera
Biao Huang
Sridhar Kamojjala
Nicholas Landes
Srinivasa Lingireddy
Kevin D. Nielsen
Faissal R. Ouedraogo
Subbu-Srikanth Pathapati
James Powell
John Joseph Sansalone
Lian Shen
Andres E. Tejada-Martinez
Subhas Karan Venayagamoorthy
Ruo-Qian Wang
Jordan M. Wilson
Tien Yee
Liqiong Zhang

Contributing Authors

René A. Camacho, Ph.D., Tetra Tech, Inc., Chapter 8
Yovanni A. Cataño-Lopera, Ph.D. Stantec, Chapters 9, 20
Biao Huang, Ph.D., Zhengzhou University, China, Chapter 23
Carrie L. Knatz, CDM Smith, Chapters 13, 14
Xiaofeng Liu, Ph.D., P.E., Pennsylvania State University, Preface, Chapters 1, 4, 10
Daniel Morse, Jacobs Engineering Group, Inc., Chapter 12
Kevin D. Nielsen, Ph.D., Jacobs, Chapter 12

Faissal R. Ouedraogo, Ph.D., University of South Florida, Chapters 6, 17
Subbu-Srikanth Pathapati, Ph.D., Mazzei Injector Co., LLC, Chapters 6, 8, 19, 21, 22
Andrés E. Tejada-Martínez, Ph.D., University of South Florida, Chapters 5, 17
Jose Vasconcelos, Auburn University, Chapter 23
Subhas Karan Venayagamoorthy, Ph.D., Colorado State University, Chapter 15
Jue Wang, Jacobs Engineering Group, Inc., Chapter 23
Ruo-Qian Wang, Ph.D., Rutgers University, Chapters 6, 7
Ed Wicklein, Carolla Engineers, Inc., Chapter 19
Jordan M. Wilson, Ph.D., CDM Smith, Chapter 15
Tien Yee, Ph.D., Kennesaw State University, Chapters 9, 12
Jie Zhang, Ph.D., Carollo Engineers, Inc., Chapters 2, 3, 9, 11, 12, 16, 17, 18

Reviewers

All contributors of the book cross-reviewed chapters written by other authors. In addition, Sri Kamojjala, P.E., D.WRE, of Las Vegas Valley Water District and Randal Samstag reviewed several chapters.

Abbreviations and Acronyms

ASM	Activated sludge model
CAD	Computer-aided design
CFD	Computational fluid dynamics
CFL	Courant–Friedrichs–Levy
COD	Chemical oxygen demand
CRTD	Cumulative residence time distribution
CT	Concentration-contact time
DAF	Dissolved air flotation
DES	Detached eddy simulation
DNS	Direct numerical simulation
DO	Dissolved oxygen
DOC	Dissolved organic carbon
DPM	Discrete phase model
EWRI	Environmental & Water Resources Institute
FDM	Finite difference method
FEM	Finite element method
FVM	Finite volume method
GIGO	Garbage in, garbage out
HS	Hydrodynamic separator
LES	Large eddy simulation
LS	Level set
MCL	Maximum contaminant level
MRF	Multiple reference frame
N-S	Navier-Stokes
NOM	Natural organic matter
ODE	Ordinary differential equation
PDE	Partial differential equation
PFR	Plug flow reactor
PIV	Particle image velocimetry
RANS	Reynolds-averaged Navier-Stokes
RCF	Radial cartridge filter
RTD	Residence time distribution
SGS	Subgrid scale
SHS	Screened hydrodynamic separator
SIMPLE	Semi-implicit method for pressure-linked equations
SIMPLEC	Semi-implicit method for pressure-linked equations—consistent
SIMPLER	Semi-implicit method for pressure-linked equations—revised
SPH	Smoothed particle hydrodynamics

SST	Shear stress transport
THMs	Trihalomethanes
TKE	Turbulent kinetic energy
UDF	User-defined function
URF	Underrelaxation factor
USBR	US Bureau of Reclamation
UV	Ultraviolet
VoF	Volume of fluid
WSP	Waste stabilization pond
WWTP	Wastewater treatment plant

Part 1

Physical, Chemical, and Biological Processes in Water, Wastewater, and Stormwater Treatment

This page intentionally left blank

CHAPTER 1
Physical Processes

Xiaofeng Liu

1.1 INTRODUCTION

In water and wastewater treatment, the key question is how to control the quality of water to an acceptable level before it is sent to the receptors, that is, a water distribution system in the case of water treatment or rivers, streams, or other water bodies in the environment in the case of wastewater treatment. The parameters for water quality can be broadly categorized as physical, chemical, and biological. Monitoring programs are in place in almost all treatment plants to measure water quality at various stages of the treatment process and to ensure compliance of the final product.

The purpose of this chapter is to provide a theoretical background on the mathematical models for the physical processes, excluding the fluid flow itself. The theory and numerical details for the computational fluid dynamics part are presented in Chapter 4. In this chapter, the fundamental physical transport processes are introduced, which include the generic transport equation and the special case of heat transfer. Other treatments related to physical processes, specifically the transport of particulate matters, are also presented.

1.2 FUNDAMENTAL PHYSICAL TRANSPORT PROCESSES

In the context of this primer, transport is defined as the movement of substances by physical means, for example, advection (or convection) and diffusion. Physical transport, in conjunction with chemical and biological processes, changes the concentration of a substance in water. Thus, to determine whether treated water complies with a quality standard, it is important for a computational fluid dynamics (CFD) modeler to understand the fundamental physical transport processes. More importantly, one needs to know how these physical processes are mathematically described and solved in computer models.

For a water quality parameter ϕ, for example, temperature or concentration, a generic transport equation has the form of

$$\underbrace{\frac{\partial}{\partial t}\phi}_{\text{temporal derivative}} + \underbrace{\nabla\cdot(\phi\mathbf{u})}_{\text{convection}} - \underbrace{\nabla\cdot(\gamma\nabla\phi)}_{\text{diffusion}} = \underbrace{S_\phi}_{\text{source/sink}} \tag{1-1}$$

where
$\mathbf{u}$ = Velocity of the carrier fluid,
γ = Diffusion coefficient, and
S_ϕ = Source or sink term, which models the production or consumption of ϕ caused by physical, chemical, or biological processes.

Examples of the source or sink terms are given in the next several chapters for chemical and biological processes. Throughout this chapter and in many places in this book, tensor notations are used. In the appendix of this chapter, a brief introduction to tensor notation is provided. Often the generic quantity ϕ represents the concentration. This generic transport equation is a partial differential equation (PDE), which is composed of differential operators. The common differential operators include temporal derivative, gradient, divergence, Laplacian, curl, as well as various source and sink terms. The functional form of the source or sink term can be simple or complex, depending on whether it is a function of ϕ itself and if so, whether it is a linear or nonlinear function.

The governing equation, Equation (1-1), is a mathematical statement of the conservation law for ϕ. Its understanding can be made easier by using a control volume while considering the change of ϕ within this volume and across its boundary (Figure 1-1). The cell P denotes the control volume under consideration, and the cell N is its neighbor. Control volume P has a volume V, and its surface is denoted as S_m. $\mathbf{n}$ is the unit normal vector of the shared surface between P and N. Since ϕ is a concentration, the total amount within the control volume is $\int\phi dV$.

The temporal derivative represents the time rate of change of ϕ within this control volume,

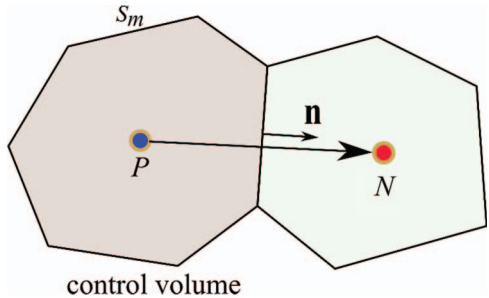

Figure 1-1. Conservation law for a control volume.

$$\frac{\partial}{\partial t}\int_V \phi\, dV \tag{1-2}$$

which can be induced by advection and diffusion across the boundary, as well as the internal production and consumption.

Advection is transport of heat or matter by a flowing fluid. In other words, it is the advective transport by the carrier fluid velocity. Assuming that the velocity at the boundary of the control volume is **u**, then the flux advected across the boundary can be evaluated as the following surface integral:

$$\oint_{S_m} \phi(\mathbf{n}\cdot\mathbf{u})\, dS \tag{1-3}$$

which can be further written as a volume integral upon invocation of Gauss's theorem,

$$\int_V \nabla\cdot(\phi\mathbf{u})\, dV \tag{1-4}$$

This term describes the transport from or to the vicinity, and it has directional information defined by the flow velocity vectors. Another commonly used term, *convection*, refers to the motion induced by heat transfer and buoyancy. In the literature, many have used *advection* and *convection* interchangeably. In this book, we use *advection* (or *convection*) for the motion induced by carrier fluid velocity.

The diffusion term represents gradient transport, which states that ϕ is transported from regions of high concentration to regions of low concentration until the concentration is uniform everywhere. Taking into account that the gradient $\nabla\phi$ points up the concentration slope and the diffusive transport is in the opposite direction, the flux across the boundary of a control volume can be written as

$$\boldsymbol{q}_s = -\gamma\nabla\phi \tag{1-5}$$

where γ is the diffusivity. Diffusion can be caused by the scattering of substance particles because of random molecular motions (molecular diffusion) or because of turbulent eddies (turbulent diffusion). By performing a surface integral with this diffusive flux, the diffusion contribution is

$$-\int_V \nabla\cdot(\gamma\nabla\phi)\, dV \tag{1-6}$$

The source or sink, that is, the production and consumption of ϕ within the control volume, can be described by a volumetric intensity S_ϕ. Therefore, the source or sink contribution within the control volume is

$$\int_V S_\phi\, d \tag{1-7}$$

Assembling all terms together, the conservation law for ϕ within the control volume can be written as

$$\int_V \left[\frac{\partial}{\partial t}\phi + \nabla\cdot(\phi\mathbf{u}) - \nabla\cdot(\gamma\nabla\phi)\right] dV = \int_V S_\phi \, dV \tag{1-8}$$

And, if the control volume is infinitely small, the integrand in Equation (1-8) should be zero. Therefore, the generic transport equation, Equation (1-1), can be derived.

Temperature is an important water quality parameter for both water and wastewater treatment. Many of the chemical and biological processes in a treatment plant are affected by temperature variations. Uneven distribution of temperature causes nonuniform fluid densities in a treatment unit. Thus, thermally induced buoyancy effects influence the hydrodynamics within these units. Gravity currents can occur such that the flow path is altered and departs from the design. Heat associated with the wastewater effluent discharged to surface water can create thermal effects on aquatic habitat. Therefore, excessive thermal discharge into rivers and streams from wastewater treatment plants is an important environmental stressor that needs to be monitored.

For a flowing fluid, the total energy is the sum of the thermal (internal) energy, kinetic energy, and the gravitational potential energy. There are three fundamental modes of heat transfer, namely conduction, convection, and radiation. These three heat transfer modes do not necessarily coexist. The governing equation for thermal energy, typically in terms of the temperature, is similar to the generic transport equation, Equation (1-1). When only conductive transfer is at work, for example, the heat transfer in a body of still water without gravity effects or a solid without radiation, the problem can be simply simulated with a diffusion equation. According to Fourier's law of conduction, the flux of thermal energy $\mathbf{q}_T$ is proportional to temperature gradient, that is,

$$\mathbf{q}_T = -k\nabla T \tag{1-9}$$

where k is the thermal conductivity and T is temperature. For simplicity, thermal conductivity k is assumed isotropic and constant. Thus, the conservation law for thermal energy gives the following conduction equation:

$$\rho C_p \frac{\partial T}{\partial t} = k\nabla^2 T \tag{1-10}$$

where ρ is the density of the carrier fluid and C_p is the specific heat. For an incompressible fluid, the thermal energy is the product of C_pT. At steady state, Equation (1-10) can be further simplified as

$$\nabla^2 T = 0 \tag{1-11}$$

which is the Laplace's equation for T.

If a fluid is moving, then the governing equation becomes more complex by adding the convection term. In this case, the unsteady convection–conduction equation has a similar form to the unsteady advection–diffusion equation. It has the form of

$$\rho C_p\left(\frac{\partial T}{\partial t}+\mathbf{u}\cdot\nabla T\right)=k\nabla^2 T+S_T \tag{1-12}$$

where $\mathbf{u}$ is the fluid velocity and S_T is the heat source or sink. Note that the advection term here is written differently than in Equation (1-1). For a viscous fluid, the viscous effect irreversibly dissipates the kinetic energy into heat. The source contribution caused by viscous heat generation can be evaluated as

$$S_T=\mu\left\{2\left[\left(\frac{\partial u}{\partial x}\right)^2+\left(\frac{\partial v}{\partial y}\right)^2+\left(\frac{\partial w}{\partial z}\right)^2\right]+\left(\frac{\partial v}{\partial x}+\frac{\partial u}{\partial y}\right)^2+\left(\frac{\partial w}{\partial y}+\frac{\partial v}{\partial z}\right)^2+\left(\frac{\partial u}{\partial z}+\frac{\partial w}{\partial x}\right)^2\right\} \tag{1-13}$$

One can observe from this equation that the viscous energy dissipation term S_T is always positive. In reality, this term has a negligible magnitude in comparison with other terms in the heat transfer equation. It may be important when the fluid shear rate is extremely high. For most water and wastewater treatment processes, the shear rate is low, and thus this term can be neglected. Other heat production or sink processes may contribute to S_T, for example, chemical reactions. In these cases, the specific formula for S_T needs to be provided.

The dimensional governing equation for the temperature can be made dimensionless with the introduction of proper scales. Let L be a characteristic length, U_o a characteristic velocity, and T_o a characteristic temperature. Using these characteristic scales, the following dimensionless variables can be defined:

$$t^*=\frac{t}{L/U_o},\ x^*=\frac{x}{L},\ y^*=\frac{y}{L},\ z^*=\frac{z}{L},\ u^*=\frac{u}{U_o},\ v^*=\frac{v}{U_o},\ w^*=\frac{w}{U_o},\ T^*=\frac{T-T_o}{\Delta T} \tag{1-14}$$

where ΔT is a known temperature differential defined as, for example, the difference between the incoming flow temperature and a fixed temperature on a boundary wall. The definitions of the characteristic scales are not unique. With these definitions, and assuming that the heat source or sink term only consists of the viscous dissipation, the temperature equation can be written as

$$\frac{\partial T^*}{\partial t^*}+\mathbf{u}^*\cdot\nabla T^*=\frac{1}{RePr}\nabla^2 T^*+\frac{Ec}{Re}S_v^* \tag{1-15}$$

where $\mathsf{Re}=U_oL/\nu$ is the Reynolds number, which is a ratio between the fluid inertial force and viscous force. The Prandtl number Pr is defined as $\nu/(k/\rho C_p)$, which is the ratio between momentum and thermal diffusivity. The product RePr

is commonly referred to as the Péclet number Pe. From the dimensionless equation, it is clear that the heat transfer is dominated by convection if Pe is high and by conduction if Pe is low. The Eckert number $\mathrm{Ec} = U_o^2/(C_p\Delta T)$ is a dimensionless number quantifying the ratio between the flow's kinetic energy and a representative enthalpy difference. Ec increases when the viscous heat generation increases. For a particular flow and heat transfer problem, the calculation of these dimensionless numbers gives a quick and easy way to appreciate the relative importance of each heat transfer mode.

In these discussions, the third mode of heat transfer, that is, thermal radiation, is not covered. Thermal radiation transmits energy through electromagnetic waves. Thermal radiation is often of secondary importance when compared with convection and conduction in water and wastewater treatment processes. However, there might be exceptions. For example, during hot summer months, the temperature of water in a treatment unit (either covered or directly exposed to sunlight) might receive a substantial amount of heat from the sun. In these cases, the emissive power of radiative heat flux from a radiation source needs to be determined first. Then, the properties of the receptive surface or fluid, including absorption, reflection, and transmission, should be quantified. On the other hand, the boundary and fluid can also act as emitting sources. Furthermore, if particulate matters are present in the fluid, scattering also needs to be considered. Thus, the radiation process is rather complicated. Reflected in the governing equation, radiation can be modeled as a flux source or sink term through the boundary of the domain. No further details are given in this introductory chapter. Interested readers can consult heat transfer references, for example, Chapter 13 in Versteeg and Malalasekera (2007).

1.3 OTHER TREATMENT-RELATED PHYSICAL PROCESSES

1.3.1 Particle Separation

One major impurity in water and wastewater is particulate matter suspended in the influent. These particles vary in size, shape, density, and biochemical composition. A major design criterion of treatment processes is to effectively remove these particulate impurities mainly with a host of physical processes, such as screening, grit removal, sedimentation (settling), flotation, and filtration (Eddy 2014). These physical separation processes might be aided by chemical and biological measures, such as coagulation and flocculation.

Screening. Screening is the physical removal of particles and debris with bars and meshes. Water is passed through the openings between the bars or meshes. Solids that are larger than the opening are retained behind the screens. As a result, screening cannot remove all solids. Its purpose is to protect downstream treatment units and equipment from blockage and abrasion. In practice, there can be other considerations regarding the design of screening. For example, water intake design should consider the protection of fish from being entrained into or impinged on

the screen (USBR 2006). The screens need to be cleaned periodically to ensure smooth passage of flow and to reduce head loss. From the point of view of CFD, modeling of the screening process depends on the type of screen and whether accumulated solids need to be considered. For bar screening, it might be possible to model the geometric details of the bars and openings. For mesh screening, it might not be so practical. An approximation is to model the screen as a permeable region that imparts a certain amount of resistance to the flow. How to quantify the resistance may be difficult. With the accumulation of debris, the resistance also changes. Most commercial CFD codes provide the capability of the inclusion of permeable zones and a variety of porous media models.

Grit Removal. In grit removal systems, dense particles such as sand and grit are removed through gravitational settling or other mechanical means of separation of the particles. Grit removal units are mostly designed for heavy particles. Light particles, such as organic biosolids, are less likely to be removed in grit removal units. Grit removal typically follows screening and precedes primary sedimentation. Several types of grit removal systems exist, based on different separation mechanisms, which include grit chambers and channels, vortex grit systems, and hydrocyclones. To model the grit removal processes using CFD, it is important that the selected CFD code can capture the removal mechanism at work. For example, in a vortex grit system, the centrifugal force on particles should be considered in the model. Since it is probably not feasible to track each of the particles, there are two alternative options. One is to model the particle concentration, also known as an Eulerian approach. The second option is to only model the trajectories of some representative particles. From the trajectories, it is possible to infer the transport and retention of the grit.

Sedimentation. Sedimentation refers to the removal of heavier-than-water particles through gravitational settling. Sedimentation typically occurs in a tank or a basin. As the flow moves through the unit, particles are carried by the flowing water and influenced by gravity. As a result, the trajectory of a particle departs from the flow path and points downward to the bottom of the unit. Heavy particles settle faster and accumulate on the bottom to form a layer of sludge, which needs to be removed. Light particles settle slower and may not have the chance to reach the bottom before exiting the unit. Thus, the size distribution of the particles in the influent needs to be considered in the design (mainly sizing) of the sedimentation tanks. Flow in a sedimentation unit is typically turbulent. The mixture of water and particles, especially in the sludge layer, exhibits non-Newtonian fluid behavior. In addition, the settling of each individual particle is affected as the particle concentration increases. The settling velocity of a particle can be hindered in the close vicinity of other particles. All these phenomena need to be considered in CFD models to evaluate settling performance. Similar to grit removal systems, the modeling of sedimentation can also use either an Eulerian approach or a Lagrangian approach.

Flotation. This process uses small gas bubbles to trap solids and float them to the surface for removal. Flotation can partially remove fine particles that might not be removable through sedimentation. Usually, flotation requires less space than

sedimentation and produces more concentrated sludge. Compressed air needs to be continuously pumped into the flow. Flotation can be used to remove oil, fat, grease, protein, and other meat waste. In CFD models, the multiphase nature of the flow caused by the injection of air needs to be considered. In addition, the entrapment of solids in gas bubbles also needs to be modeled properly.

Filtration. In the filtration process, low concentrations of suspended particles can be removed when water flows through porous media, typically made of sand. As the fluid moves through the pore space, the suspended particles may be trapped within the porous media through direct interception, Brownian motion (diffusion), inertial deposition, sedimentation, and hydrodynamic collision. The retention of particles in the porous media can gradually clog the pore space and reduce the effectiveness of the filtration. Thus, periodic backwashing is needed. The filtration process can operate under either gravity or pressure. Gravity-operated filtration is typically slow because of limited pressure head to drive the flow through the media. The filtration process can be accelerated if the flow is pressurized. A pressurized filtration unit also requires less space. In CFD models, the filter can be modeled as a zone with additional flow resistance. The filtration process is complex because of the stochastic nature of the particle entrapment in the pore space.

1.3.2 Hydraulics in Water and Wastewater Treatment

Hydraulics consists of the application of theories of fluid mechanics to practical problems in water resources. Sometimes *hydraulics* and *fluid mechanics* are used interchangeably. The hydraulics of the flowing water in treatment plants are governed by the same set of equations for the fluid flow in oceans, rivers, lakes, and even in the atmosphere. That is why a generic CFD model can be used to model the hydraulics in treatment processes. However, before the wide use of CFD models for water and wastewater treatment, simplified traditional hydraulic analysis was used extensively for the design and evaluation of treatment processes. Because of this historical reason, most design guidelines, regulations, and textbooks heavily use traditional hydraulics principles. CFD models do not completely replace their use. Instead, CFD models can be used as a tool to provide a more detailed description of the flow field when a higher level of accuracy is needed for a design.

In this section, important hydraulics concepts and phenomena in water and wastewater treatment are briefly introduced. CFD models can and have been used to analyze these phenomena. It is by no means a complete list. Interested readers should refer to hydraulics books, such as Chow (1959) and Hager (2010).

Head Loss. Head loss is defined as the loss of energy (head) when water flows through a structure. Excessive head loss increases the operational cost since more powerful pumps are needed, and therefore, more electricity. Head loss is not always a negative thing. For example, sometimes it is intentionally designed to dissipate the flow energy before the water is discharged downstream and to reduce erosion. Another example is in sedimentation tanks, where the flow velocity cannot be high enough to stir up the settled sediment. If the influent is too energetic, a certain measure of energy dissipation is needed to dampen the flow.

In hydraulics, head loss is made of two parts, that is, the global head loss caused by friction and the local head loss caused by, for example, sudden expansion, contraction, screening, grit removal bars, or filtration. A CFD model calculates the two parts of energy loss; however, it is of more practical interest to simply predict the total head loss. With the simulated pressure p and velocity field $\mathbf{u}$, the total head at any cross section in the treatment unit can be calculated as

$$H = \int_S \left(\frac{p}{\rho g} + z + \frac{|u|^2}{2g} \right) dS \tag{1-16}$$

where z is the vertical coordinate and S is the cross-sectional area. Thus, from CFD simulation results, the total head can be calculated at any two cross sections, and their difference is the head loss. The advantage of using CFD is that there is no need to assume energy loss coefficients to account for the nonuniform distribution of pressure and velocity.

Conveyance Infrastructure. Pipes and open channels (conduits) are commonly used in treatment plants to transfer water from upstream to downstream units. In pipes, the flow can fill the entire channel cross section and thus be pressurized, or the flow can partially fill the channel cross section, thereby behaving as an open channel flow. In some cases, mixed flow (part of the pipe is full and the rest open) exists. It is important for designers and operators to fully understand the flow dynamics in a treatment plant. For sewer and stormwater collection systems, the rapid inflow of a large amount of water during a storm event can quickly exceed the capacity of the system and cause damage. For example, a hydraulic transient can occur during rapid filling or sudden closure in the collection system. The fast-moving pressure surge can destroy unprotected equipment and burst pipes. CFD models are well suited to model these complex flow phenomena. To capture these processes, the CFD models should be able to predict the free surface change using certain numerical schemes. Methods to capture or model the free surface in CFD models include the volume of fluid (VoF) method and level set (LS) method.

Flow Controls. In a typical water and wastewater treatment plant, flow needs to be regulated at various points of the treatment process. Common flow-regulating devices are gates, valves, culverts, siphons, and weirs. It is often desired to evaluate the effectiveness of a flow control device and, more importantly, to provide a rating curve for operational purposes. For example, the discharge from a gate depends on the opening, among many other things. CFD simulations can be performed to accurately quantify the relationship between discharge and the controlling parameters.

Hydraulic Jumps and Drops. Hydraulic jumps form when flow transitions from a supercritical to a subcritical regime. They happen in a confined local area. The signature of hydraulic jumps is that the water depth jumps from shallow to deep in the direction of the flow. Flow is highly turbulent and energetic within the jump. Waves and rollers can be observed on top of the jump, accompanied by substantial air bubble entrainment. A large portion of the incoming flow energy is

dissipated into heat, which forms the foundation for the design of stilling basins. Hydraulic drops are the opposite of hydraulic jumps. They transition the flow from subcritical to supercritical. Often, hydraulic drops form at a brink where the bottom elevation has a sudden decrease. CFD models can be used to simulate the hydraulic jump or drop flow process and describe in detail the flow field. Such CFD models need to have the capability to capture the free surface variation. More advanced CFD studies have been carried out to study other aspects of hydraulic jumps, for example, the rate of air entrainment.

Drop Shafts. Drop shafts are used to collect and transport sewer water and stormwater where there is substantial elevation difference between the point of collection and the bottom sewer line. A drop shaft typically is made of three parts, that is, an inlet structure, a vertical pipe, and an air-regulating device. Water flows through the inlet and drops through the vertical pipe until it plunges into the bottom pool. Air entrainment and ventilation are the major design considerations for a drop shaft. If air is not supplied adequately, negative pressure can occur to induce cavitation. On the other hand, if too much air is entrained without proper ventilation, geysering can occur.

1.4 SUMMARY

In this chapter, the fundamentals of the physical processes in water and wastewater treatment are introduced. They serve as the foundation for many CFD codes. The governing equation of the generic unsteady advection–diffusion equation is solved in CFD models for contaminant concentration and temperature. It is usually solved in conjunction with the flow equations, which provide the carrier fluid velocity field and other parameters, such as turbulent diffusivity. Particle separationis unique because of the settling of individual particles. It can be modeled with an Eulerian approach, where the particle concentration is governed by a modified transport equation; or it can be modeled with a Lagrangian approach, where the trajectory of each particle is tracked. The former is most commonly used in practice. However, the latter is also useful for the description of the flow field and the qualitative prediction of particle separation efficiency.

References

Chow, V. 1959. *Open-channel hydraulics*. New York: McGraw-Hill.

Eddy, M. 2014. *Wastewater engineering: Treatment and resource recovery*. 5th ed. New York: McGraw-Hill Education.

Hager, W. 2010. *Wastewater hydraulics: Theory and practice*. 2nd ed. New York: Springer.

USBR (US Bureau of Reclamation). 2006. *Fish protection at water diversions: A guide for planning and designing fish exclusion facilities*. Denver: USBR, US Dept. of Interior.

Versteeg, H., and W. Malalasekera. 2007. *An introduction to computational fluid dynamics: The finite volume method*. 2nd ed. London: Pearson Education.

APPENDIX

TENSOR NOTATIONS

CFD codes solve the governing partial differential equation (PDEs), which are made of differential operators. To fully appreciate the mathematical models and the processes they represent, it is essential for CFD users and developers to be familiar with the tensor notations and differential operator definitions. This section provides a brief overview of these. However, it is not intended to serve as a comprehensive reference.

The description of tensor notations typically starts with the definition of a coordinate system. The most commonly used one is the right-handed Cartesian coordinate system, with the x, y, and z axes orthogonally spanning the 3D space (Figure 1-2). Other, less commonly used coordinate systems are cylindrical and spherical coordinates, which can be used when the geometry of the CFD domain is a cylinder or a sphere.

In CFD, variables and constants can be classified into scalars, vectors, and tensors. In fact, scalars and vectors can be viewed as special cases of tensors. They are called tensors with rank 0 and 1, respectively.

The following is a list of definitions for some of the differential operators approximated in CFD models:

Gradient operator: The gradient operator ∇ works on any tensor field to produce a tensor field one rank higher.

$$\nabla s = \left(\frac{\partial s}{\partial x}, \frac{\partial s}{\partial y}, \frac{\partial s}{\partial z}\right) \tag{1-17}$$

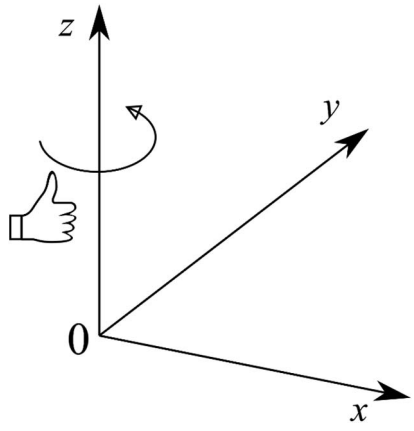

Figure 1-2. Definition of a right-handed coordinate system.

Thus, if s is a scalar field, then ∇s is a vector field, and if s is a vector field, ∇s is a second-order tensor field.

Divergence operator: The divergence operator works on any tensor field (rank 1 and above) to produce a tensor field one rank lower. For example, if $\mathbf{a} = (a_x, a_y, a_z)$ is a vector field, then

$$\nabla \cdot \mathbf{a} = \frac{\partial a_x}{\partial x} + \frac{\partial a_y}{\partial y} + \frac{\partial a_z}{\partial z} \tag{1-18}$$

which produces a scalar field. An example of the divergence of a vector field is the conservation of mass for incompressible fluid $\nabla \cdot \mathbf{u} = 0$, where $\mathbf{u}$ is the fluid velocity vector. That is the reason that the mass conservation of an incompressible is also called the divergence-free condition. If $\mathbf{T} = T_{ij}$ is a rank 2 tensor field defined as

$$\mathbf{T} = T_{ij} = \begin{pmatrix} T_{xx} & T_{xy} & T_{xz} \\ T_{yx} & T_{yy} & T_{yz} \\ T_{zx} & T_{zy} & T_{zz} \end{pmatrix} \tag{1-19}$$

then

$$\nabla \cdot \mathbf{T} = \partial_i T_{ij} = \begin{pmatrix} \frac{\partial T_{xx}}{\partial x} + \frac{\partial T_{xy}}{\partial y} + \frac{\partial T_{xz}}{\partial z} \\ \frac{\partial T_{yx}}{\partial x} + \frac{\partial T_{yy}}{\partial y} + \frac{\partial T_{yz}}{\partial z} \\ \frac{\partial T_{zx}}{\partial x} + \frac{\partial T_{zy}}{\partial y} + \frac{\partial T_{zz}}{\partial z} \end{pmatrix} \tag{1-20}$$

which produces a vector field. An example of the divergence of a tensor is the viscous force term in the fluid momentum equation $\nabla \cdot (\nabla \mathbf{u})$ (viscosity omitted for clarity), where velocity gradient $\nabla \mathbf{u}$ produces a strain tensor field and then the divergence operator on this tensor field produces a vector field (viscous force in three directions).

Laplacian operator: The Laplacian is related to diffusion of substance or momentum. The Laplacian operator transforms a tensor field into another tensor field of the same rank.

$$\nabla^2 a = \nabla \cdot \nabla a = \frac{\partial^2 a}{\partial x^2} + \frac{\partial^2 a}{\partial y^2} + \frac{\partial^2 a}{\partial z^2} \tag{1-21}$$

The Laplacian operator is equivalent to "the divergence of the gradient field."

CHAPTER 2
Chemical Processes

Jie Zhang

Chemicals are used alongside physical treatment processes to achieve various water quality standards during water or wastewater treatment. Computational fluid dynamic (CFD) modeling is valuable for predicting chemical concentration at outlets or within treatment units.

2.1 CHEMICAL REACTION TYPES

In general, the chemical reactions in water and wastewater treatment can be categorized into five groups: chemical precipitation, chemical coagulation, chemical oxidation, ion exchange, and chemical stabilization.

Chemical precipitation is the most common method for removing dissolved metals from wastewater solution containing toxic metals. To convert the dissolved metals into solid particle form, a precipitation reagent is added to the mixture. A chemical reaction, triggered by the reagent, causes the dissolved metals to form solid particles. Filtration can then be used to remove the particles from the mixture. How well the process works depends on the kind of metal present, the concentration of the metal, and the kind of reagent used.

Chemical coagulation involves destabilizing particles so that they aggregate during chemical flocculation. Fine solid particles dispersed in water carry negative electric surface charges (in their normal stable state), which prevent them from forming larger groups and settling. Chemical coagulation destabilizes these particles by introducing positively charged coagulants that then reduce the negative particles' charge. Once the charge is reduced, the particles freely form larger groups. Next, an anionic flocculant is introduced to the mixture. Because the flocculant reacts against the positively charged mixture, it either neutralizes the particle groups or creates bridges between them to bind the particles into larger groups. After larger particle groups are formed, sedimentation can be used to remove the particles from the mixture.

Chemical oxidation introduces an oxidizing agent (e.g., chlorine and ozone) to provide electrons to the target chemicals in water. The target chemicals then

undergo structural modification, becoming less destructive compounds. Alkaline chlorination uses chlorine as an oxidant against cyanide. However, alkaline chlorination as a chemical oxidation process can lead to the creation of toxic chlorinated compounds, and additional steps may be required. Advanced oxidation can help remove any organic compounds that are produced as by-products of chemical oxidation, through processes such as steam stripping, air stripping, or activated carbon adsorption.

Ion exchange is a type of technology that can be used to remove hardness and a wide range of contaminants from drinking water, such as nitrate, perchlorate, arsenic, bromide, dissolved organic carbon (DOC), cobalt, and uranium (Amini et al. 2015). For example, in water softening technology, positively charged sodium ions are introduced in the form of dissolved sodium chloride salt, or brine. Hard calcium and magnesium ions exchange places with sodium ions, and free sodium ions are simply released to the water. However, after softening a large amount of water, the softening solution may fill with excess calcium and magnesium ions, requiring the solution to be recharged with sodium ions.

Chemical stabilization works in a similar fashion as chemical oxidation. Sludge is treated with a large amount of a given oxidant, such as chlorine. The introduction of the oxidant slows down the rate of biological growth within the sludge and helps deodorize the mixture. Water is then removed from the sludge.

For more information about specific chemical reactions, refer to Crittenden et al. (2005).

2.2 CHEMICAL SPECIES TRANSPORT

The transport of chemical species in water can be mathematically represented by a general advection–diffusion–reaction equation:

$$\frac{\partial C_i}{\partial t} + u_j \frac{\partial C_i}{\partial x_j} - \frac{\partial}{\partial x_j}\left(D_i \frac{\partial C_i}{\partial x_j}\right) = S_i \tag{2-1}$$

where
u_i = Flow velocity (LT^{-1}),
C_i = Species concentration (ML^{-3}),
D_i = Effective diffusivity (combination of molecular and turbulent diffusivity) for the chemical species (L^2T^{-1}), and
S_i = External volumetric source term ($ML^{-3}T^{-1}$) including generation, consumption, and transfer to another phase.

The external volumetric source term, S_i, on the right side of Eq. (2-1), represents the chemical change rate caused by chemical reactions. For example, the commonly used source terms for ozone disinfection are listed in Table 2-1. In this table, k_d is the ozone decay constant, C_l is the concentration of dissolved ozone, k_{NOM} is the reaction rate constant for the reaction between dissolved ozone

Table 2-1. Commonly Used Source Terms in Chemical Species Transport Equations for Ozone Disinfection

Species	*Source Terms in Transport Equations*	*References*
Dissolved ozone, C_l	$S_{C_l} = -k_d C_l$	Muroyama et al. (1999); Huang et al. (2004)
NOM	$S_{[NOM]} = -k_{NOM}\,[NOM]\,C_l$	Chen (1998); Kim et al. (2002)
Bromate, C_B	$S_{C_B} = k_B C_l$	Kim et al. (2002); Tang et al. (2005)
CT (concentration–contact time)	$S_{CT} = C_l$	Zhang (2006); Zhang et al. (2014)

Note: k_d and k_B are first-order reaction rate constants (T^{-1}); k_{NOM} is a second-order reaction rate constant ($M^{-1}L^3\,T^{-1}$).

and natural organic matter (NOM), [NOM] is the concentration of NOM, and k_B is the bromate formation rate constant.

References

Amini, A., Y. Kim, J. Zhang, T. Boyer, and Q. Zhang. 2015. "Environmental and economic sustainability of ion exchange drinking water treatment for organics removal." *J. Cleaner Prod.* **104**: 413–421.

Chen, C. M. 1998. "Modeling drinking water disinfection in ozone bubble-diffuser contactors." Department of Civil Engineering, Ph.D. dissertation, Purdue Univ.

Crittenden, J., R. R. Trussell, D. W. Hand, K. J. Howe, and G. Tchobanoglous. 2005. *Water treatment: Principles and design*. 2nd ed. Hoboken, NJ: Wiley.

Huang, T., C. J. Brouckaert, M. Pryor, and C. A. Buckley. 2004. "Application of computational fluid dynamics modeling to an ozone contactor." *Water SA* **30** (1): 51–56.

Kim, J. H., R. B. Tomiak, J. L Rennecker, B. J. Marinas, R. J. Miltner, and J. H. Owens. 2002. "Inactivation of Cryptosporidium in a pilot-scale ozone bubble-diffuser contactor. Part II: Model verification and application." *J. Environ. Eng.* **128** (6): 522–532.

Muroyama, K., T. Norieda, A. Morioka, and T. Tsuji. 1999. "Hydrodynamics and computer simulation of an ozone oxidation reactor for treating drinking water." *Chem. Eng. Sci.* **54** (21): 5285–5292.

Tang, G., K. Adu-Sarkodie, D. Kim, J. H. Kim, S. Teefy, H. M. Shukairy, and B. J. Marinas. 2005. "Modeling Cryptosporidium parvum oocyst inactivation and bromate formation in a full-scale ozone contactor." *Environ. Sci. Technol.* **39** (23): 9343–9350.

Zhang, J., A. E. Tejada-Martinez, Q. Zhang, and H. Lei. 2014. "Evaluating hydraulic and disinfection efficiencies of a full-scale ozone contactor using a RANS-based modeling framework." *Water Res.* **52**: 155–167.

Zhang, J. P. 2006. "An integrated design approach for improving drinking water ozone disinfection treatment based on computational fluid dynamics." Department of Civil Engineering, Ph.D. dissertation, Univ. of Waterloo.

This page intentionally left blank

CHAPTER 3
Biological Processes

Jie Zhang

In addition to physical and chemical treating processes, biological processes are involved in water and wastewater treatment as well. In water treatment, biological treatment technology is not commonly used, but biological processes (e.g., inactivation) exist in water disinfection. In wastewater treatment, biological treatment technologies are commonly used, such as activated sludge systems and algae raceways. A common principle of biological wastewater treatment technologies is to use microorganisms such as bacteria (aerobically or anaerobically), algae, and fungi (aerobically) to consume or decompose the organic matters in wastewater and consequently clean wastewater. Since many biological processes involved in water and wastewater treatment have been well described in water treatment books (Grady et al. 2011, Crittenden et al. 2012), this primer focuses only on the biological processes that have been successfully integrated in computational fluid dynamic (CFD) models. Inactivation, the activated sludge process, and the biological process of microalgal growth are three examples of biological processes.

3.1 INACTIVATION

The commonly used disinfection agents in water and waste treatment are (1) free chlorine, (2) combined chlorine (chlorine combined with ammonia, also known as chloramines), (3) chlorine dioxide, (4) ozone, and (5) UV light. The first four are chemical oxidants, whereas UV light involves the use of electromagnetic radiation. For the chemical oxidants, the specific mechanisms of microorganism inactivation are not well understood. Inactivation depends on the properties of each microorganism, the disinfectant, and the water. In addition, the observed reaction rates can vary by as much as six orders of magnitude from one organism to the other, even for one disinfectant, and the reaction rates of the well-understood disinfection reactions (e.g., UV light) vary by one and one-half orders of magnitude.

Nevertheless, a simple and widely used kinetic model has proved to be useful in many applications. The Chick–Watson disinfection model (Droste 1997) can read as

$$\ln\frac{N}{N_0} = -k_c C^n t \tag{3-1}$$

where
N = Number of microorganisms (L^{-3}),
N_0 = Initial number of microorganisms (L^{-3}),
k_c = Inactivation rate constant (the units depends on n),
C = Concentration of disinfectant (ML^{-3}), and
t = Contact time (T).
The exponent n varies depending on disinfectant and microorganism species and is commonly assumed to be 1. The disinfectant rate constant depends on disinfectant and microorganism species as well and is sensitive to environmental conditions in water.

A general principle derived from the Chick–Watson model is that as the product of disinfectant concentration and contact time increases (CT), the inactivation of microorganism is enhanced. Practically, CT value can be used as an indicator of disinfection efficiency. Thus, in modeling inactivation, instead of solving the transport equation for microorganisms (Wols et al. 2010), which can be written as

$$\frac{\partial N_m}{\partial t} + u_j\frac{\partial N_m}{\partial x_j} - \frac{\partial}{\partial x_j}\left(D_i\frac{\partial N_m}{\partial x_j}\right) = S_{N_m} \tag{3-2}$$

where N_m is the concentration of microorganism m (L^{-3}) and S_{N_m} is the external volumetric source term for microorganism m ($L^{-3}T^{-1}$).

It is more convenient to solve the transport equation for CT (Zhang et al. 2014), which is similar to Equations (3-1) to (3-2) and can be written as

$$\frac{\partial (CT)}{\partial t} + u_j\frac{\partial (CT)}{\partial x_j} - \frac{\partial}{\partial x_j}\left(D\frac{\partial (CT)}{\partial x_j}\right) = S_{CT} \tag{3-3}$$

The source term is defined as

$$S_{CT} = C_{O_3} \tag{3-4}$$

where C_{O_3} is the concentration of dissolved ozone (ML^{-3}).

Note that Eqautions (3-2) and (3-3) can be integrated into CFD models.

3.2 ACTIVATED SLUDGE PROCESS

In a sewage or industrial wastewater treatment plant, the activated sludge process is a biological process that can be used for (1) oxidizing carbonaceous biological matter; (2) oxidizing nitrogenous matter, mainly ammonium and nitrogen in biological matter; and (3) removing nutrients (nitrogen and phosphorus).

The mainstream of modeling activated sludge process follows the series of activated sludge model (ASM) models republished by Henze et al. (2000). The three types of ASM models are named ASM1, ASM2, and ASM3. According to the review of Meister et al. (2017), although the ASM1 (Henze et al. 1987) and ASM3 (Gujer et al. 1999) models both account for the biological processes of carbon oxidation, nitrification, and denitrification, the concepts differ in the description of the heterotrophic growth and decay. For the decay concept, ASM1 uses the death–regeneration model, whereas ASM3 considers endogenous respiration. For the growth concept, the heterotrophic bacteria denoted by *XBH* directly consume the readily available biodegradable substrate *SS* in ASM1, whereas the growth is deferred by considering the storage of internal cell compounds in ASM3. ASM2 (Henze et al. 1999, 1995) distinguishes itself by including biological phosphorus removal processes in the model formulation. A combined feature of these ASM models is that the biological treatment is described by a sequence of biokinetic processes, which are expressed as a system of ordinary differential equations (ODEs). The commonly used ASM model in CFD is ASM1, which consists of 13 compounds and 8 biokinetic processes. A comprehensive description of ASM1 can be found in Henze et al. (1987) and Henze et al. (2000). The application of the CFD–ASM integrated model may refer to Glover et al. (2006), Le Moullec et al. (2010, 2011), Lei and Ni (2014), and Meister et al. (2017).

3.3 BIOLOGICAL PROCESS OF MICROALGAL GROWTH

The algae raceway is an emerging technology for treating wastewater and providing bioenergy through the cultivation of microalgae using wastewater nutrients. The process of microalgal growth is not only affected by environmental conditions such as temperature, irradiance, and nutrient concentrations but also by physical processes, such as fluid flow and particulate sedimentation.

According to the review by Park and Li (2015), the biological process of microalgal growth and the impact of various parameters have been thoroughly studied and modeled in the past decades. The Monod model and the cell-quota model have both been established as the fundamental methods to describe the nutrient limitation of phytoplankton reproductive rates, and they have further evolved into more complex forms (Klausmeier et al. 2004). Although the cell-quota model has been reported to depict nutrient-limited growth more accurately than the Monod model (Sommer 1991), difficulties of measuring the independent variables in the former have prompted model developments that use the Monod equation (Buhr and Miller 1983, Yang 2011). The effects of irradiance and its dynamics change dependent on cell concentration and suspension depth have been modeled as well (Cornet et al. 1995, Huisman and Weissing 1994) and have led to the studies of models that include the effects of both nutrients and light (Bernard 2011, Quinn et al. 2011).

To integrate the biokinetic process into the CFD model, biomass, carbon dioxide concentration, and nitrogen concentration can be modeled using the

transport equation similar to Equation (3-2) with a source term. For example, the source term of algae can be expressed as (Yang 2011)

$$\frac{dX}{dt} = \frac{F}{V}(X_0 - X) + \mu X - DX \tag{3-5}$$

where
F = Volumetric flow rate (L^3T^{-1}),
V = Volume of element (L^3),
X_0 = Influent mass concentration of algae (ML^{-3}),
X = Effluent mass concentration of algae (ML^{-3}),
μ = Specific growth rate of algae (T^{-1}), and
D = Death coefficient (T^{-1}).

The specific growth rate can be expressed as the combined product of the effects of carbon dioxide concentration (C), nitrogen concentration (N), irradiance (I), and temperature (T) (Yang 2011). The effects of CO_2, nitrogen, and irradiance can be expressed in the form of Monod-type functions (Buhr and Miller 1983, Cerco and Cole 1995, Muñoz-Tamayo et al. 2013). An example model for the specific growth rate μ can be expressed as

$$\mu = \mu_{\max}\left(\frac{C}{K_C + C}\right)\left(\frac{N}{K_N + N}\right)\left(\frac{I}{K_I + I}\right)g(T) \tag{3-6}$$

where
μ_{max} = Maximum specific growth rate (T^{-1}),
C = Effluent concentration of dissolved CO_2 (ML^{-3}),
N = Concentration of inorganic nitrogen (ML^{-3}),
I = Erradiance at a specified pond depth ($L^2T^{-1}N$).
K_C, K_N, and K_I = half-saturation constants for cell growth dependent on carbon dioxide, N, and irradiance, respectively (ML^{-3}, ML^{-3}, and $L^2T^{-1}N$, respectively), and
$g(T)$ = Function of temperature that can be expressed by assuming exponential variation caused by nonoptimal temperature (James and Boriah 2010).

$$g(T) = e^{-m(T-T_{opt})^2} \tag{3-7}$$

where
m = Empirical constant for nonoptimal temperature (dimensionless),
T = Temperature (Θ), and
T_{opt} = Optimal temperature for autotrophic growth (Θ).

A good example of an integrating biokinetic model of microalgal growth with CFD is Park and Li (2015).

References

Bernard, O. 2011. "Hurdles and challenges for modelling and control of microalgae for CO_2 mitigation and biofuel production." *J. Process Control* **21** (10): 1378–1389.

Buhr, H. O., and S. B. Miller. 1983. "A dynamic model of the high-rate algal-bacterial wastewater treatment pond." *Water Res.* **17** (1): 29–37.

Cerco, C. F., and T. Cole. 1995. *User's guide to the CE-QUAL4CM: Three-dimensional eutrophication model*. Technical Rep. No. EL-95-1. Vicksburg, MS: US Army Engineer Waterways Experiment Station.

Cornet, J. F., C. G. Dussap, J. B. Gros, C. Binois, and C. Lasseur. 1995. "A simplified monodimensional approach for modeling coupling between radiant light transfer and growth kinetics in photobioreactors." *Chem. Eng. Sci.* **50** (9): 1489–1500.

Crittenden, J. C., R. R. Trussell, D. W. Hand, K. J. Howe, and G. Tchobanoglous. 2012. *MWH's water treatment: Principles and design*. Hoboken, NJ: Wiley.

Droste, R. L. 1997. *Theory and practice of water and wastewater treatment*. Hoboken, NJ: Wiley.

Glover, G. C., C. Printemps, K. Essemiani, and J. Meinhold. 2006. "Modelling of wastewater treatment plants–how far shall we go with sophisticated modelling tools?" *Water Sci. Technol.* **53** (3): 79–89.

Grady, C. L., Jr., G. T. Daigger, N. G. Love, and C. D. Filipe. 2011. *Biological wastewater treatment*. Boca Raton, FL: CRC Press.

Gujer, W., M. Henze, T. Mino, and M. Van Loosdrecht. 1999. "Activated sludge model no. 3." *Water Sci. Technol.* **39** (1): 183–193.

Henze, M., C. P. L. Grady Jr., W. Gujer, G. V. R. Marais, and T. Matsuo. 1987. *Activated sludge model no. 1*. Science Technical Rep. No. 1. London: IAWPRC.

Henze, M., W. Gujer, T. Mino, T. Matsuo, M. C. R. Wentzel, and G. Marais. 1995. *Activated sludge model no. 2*. Science Technical Rep. No. 3. London: IAWQ.

Henze, M., W. Gujer, T. Mino, T. Matsuo, M. C. R. Wentzel, G. Marais, and M. C. Van Loosdrecht. 1999. "Activated sludge model no. 2d, ASM2d." *Water Sci. Technol.* **39** (1): 165–182.

Henze, M., W. Gujer, T. Mino, and M. C. M. Van Loosdrecht. 2000. *Activated sludge models ASM1, ASM2, ASM2d and ASM3*. London: International Water Association Publications.

Huisman, J., and F. J. Weissing. 1994. "Light-limited growth and competition for light in well-mixed aquatic environments: An elementary model." *Ecology* **75** (2): 507–520.

James, S. C., and V. Boriah. 2010. "Modeling algae growth in an open-channel raceway." *J. Comput. Biol.* **17** (7): 895–906.

Klausmeier, C. A., E. Litchman, and S. A. Levin. 2004. "Phytoplankton growth and stoichiometry under multiple nutrient limitation." *Limnol. Oceanogr.* **49** (4part2): 1463–1470.

Le Moullec, Y., C. Gentric, O. Potier, and J. P. Leclerc. 2010. "CFD simulation of the hydrodynamics and reactions in an activated sludge channel reactor of wastewater treatment." *Chem. Eng. Sci.* **65** (1): 492–498.

Le Moullec, Y., O. Potier, C. Gentric, and J. P. Leclerc. 2011. "Activated sludge pilot plant: Comparison between experimental and predicted concentration profiles using three different modelling approaches." *Water Res* **45** (10): 3085–3097.

Lei, L., and J. Ni. 2014. "Three-dimensional three-phase model for simulation of hydrodynamics, oxygen mass transfer, carbon oxidation, nitrification and denitrification in an oxidation ditch." *Water Res.* **53**: 200–214.

Meister, M., D. Winkler, M. Rezavand, and W. Rauch. 2017. "Integrating hydrodynamics and biokinetics in wastewater treatment modelling by using smoothed particle hydrodynamics." *Comput. Chem. Eng.* **99**: 1–12.

Muñoz-Tamayo, R., F. Mairet, and O. Bernard. 2013. "Optimizing microalgal production in raceway systems." *Biotechnol. Progress* **29** (2): 543–552.

Park, S., and Y. Li. 2015. "Integration of biological kinetics and computational fluid dynamics to model the growth of Nannochloropsis salina in an open channel raceway." *Biotechnol. Bioeng.* **112** (5): 923–933.

Quinn, J., L. De Winter, and T. Bradley. 2011. "Microalgae bulk growth model with application to industrial scale systems." *Bioresour. Technol.* **102** (8): 5083–5092.

Sommer, U. 1991. "A comparison of the Droop and the Monod models of nutrient limited growth applied to natural populations of phytoplankton." *Funct. Ecol.* **5** (4): 535–544.

Wols, B. A., J. A. M. H. Hofman, W. S. J. Uijttewaal, L. C. Rietveld, and J. C. Van Dijk. 2010. "Evaluation of different disinfection calculation methods using CFD." *Environ. Modell. Software* **25** (4): 573–582.

Yang, A. 2011. "Modeling and evaluation of CO2 supply and utilization in algal ponds." *Ind. Eng. Res.* **50** (19): 11181–11192.

Zhang, J., A. E. Tejada-Martínez, and Q. Zhang. 2014. "Developments in computational fluid dynamics-based modeling for disinfection technologies over the last two decades: A review." *Environ. Modell. Software* **58**: 71–85.

Part 2

Fundamentals of Computational Fluid Dynamics

This page intentionally left blank

CHAPTER 4

Overview of Computational Fluid Dynamics

Xiaofeng Liu

Computational fluid dynamics (CFD) is a computer simulation technique to describe, evaluate, and predict the motion of fluid within a domain of interest. More broadly, it may also cover processes associated with the carrier fluid, for example, heat and mass transport, chemical reactions, and biological processes. These processes are of great importance for water, wastewater, and stormwater treatment.

CFD has gained popularity in all engineering disciplines where fluids are involved. It is popular because it can substantially reduce cost and time for a new design in comparison to physical modeling, it has flexibility in simulating various conditions, it can reduce the risk associated with physical tests under hazardous conditions, and it can provide a higher level of confidence that a design can meet regulatory requirements.

The purpose of this chapter is to give an overview about CFD, the brief history behind it, the available packages and codes, the basic workflow of a typical CFD job, and some discussion on the challenges and opportunities for the CFD community in general and the uniqueness about its application in the water and wastewater treatment industry.

4.1 WHAT IS COMPUTATIONAL FLUID DYNAMICS?

4.1.1 Overview

Fluid (e.g., water and air) and the mechanics behind its motion have a long history in human civilization. Humans have long recognized the importance of fluid flow to use of water, taming of floodwater, irrigation of crops, public health, and the sustainability of the world in general. In the modern age, fluid mechanics have been infused in almost all aspects of our daily lives.

Systematic studies of fluid flow date way back in history. It is not the intention of this chapter to review all the glorious achievements and milestones in fluid

mechanics. The first chapters of many fluid mechanics textbooks contain a good account of these. Among them, the most relevant to this primer are the Navier-Stokes equations proposed by the French Claude Louis Marie Henry Navier (1785–1836) and the Irish George Gabriel Stokes (1819–1903). These equations, which add viscous effect to the Euler equations for inviscid flows, mathematically describe the conservation laws for mass and momentum.

For simplicity, the Navier-Stokes equations for incompressible flows read

$$\nabla \cdot \mathbf{u} = 0 \tag{4-1}$$

$$\frac{\partial \mathbf{u}}{\partial t} + \mathbf{u} \cdot \nabla \mathbf{u} = \frac{-1}{\rho} \nabla p + \nu \nabla^2 \mathbf{u} \tag{4-2}$$

where
$\mathbf{u}$ = Velocity vector,
p = Pressure,
ρ = Density,
t = Time, and
ν = Kinematic viscosity of fluid.

One can see that the Navier-Stokes equations are a set of four coupled, nonlinear partial differential equations (PDEs) for velocity $\mathbf{u}$ (three components in 3D space) and pressure. Velocity and pressure are coupled together, and pressure has its influence only through the term ∇p. The nonlinearity occurs mainly because of the momentum advection term $\mathbf{u} \cdot \nabla \mathbf{u}$, which is responsible for the chaotic behavior of turbulent flows. Numerical schemes in CFD models for solving the Navier-Stokes equations need to fully consider these characteristics (velocity–pressure coupling and nonlinearity).

The Navier-Stokes equations have more complex forms under other conditions, for example, when the fluid compressibility and the buoyancy effect are nonnegligible. In water and wastewater treatment, more physics (also known as terms) need to be added to the simple form equations, depending on the physical processes. The specific forms of the governing fluid equations can be found in the respective chapters of this book. Unfortunately, analytical solutions for the Navier-Stokes equations only exist under simplified conditions on a domain with primitive shapes. Approximate numerical solutions are often sought by using computers.

4.1.2 What Is Behind the Scenes of CFD Codes?

The Navier-Stokes equations are at the core of most CFD software. In a nutshell, all CFD packages solve the Navier-Stokes equations, in the full or simplified forms, with various numerical methods. Broadly, these numerical methods can be classified into mesh-based and meshless methods. Most of the application-oriented CFD software is mesh-based, which means that the simulation domain has to be divided into discrete cells, elements, or grid points. The name of the discrete unit depends on the numerical method to be used, which include finite

volume method (FVM), finite element method (FEM), and finite difference method (FDM), corresponding to cells, elements, and grid points, respectively. A brief introduction of these methods is as follows:

- **Finite Volume Method:** This method discretizes the governing equation on each control volume (Versteeg and Malalasekera 2007). The governing equation is first integrated over the volume. The divergence terms in the volume integral are converted to surface integrals using Gauss's theorem. The solution value at cell centers and the fluxes through the shared surfaces in between two adjacent cells need to be evaluated through interpolation and other means. FVM is widely used in CFD because of its guarantee of mass conservation and ease of implementation on unstructured meshes. The open-source CFD package OpenFOAM and the commercial code Fluent use the finite volume method.
- **Finite Element Method:** This method is popular in solid mechanics and structural analysis (Zienkiewicz and Taylor 1989). However, recently it is also commonly used in other physics problems, including solving the Navier-Stokes equations. In FEM, the solution of a field variable is sought at nodes that define the shape of each element. The solution at nonnodal points, that is, the interior of the elements, is obtained through interpolation (shape) functions, which are prescribed and determine how the field variables change within an element. The PDE to be solved is then converted into the so-called weak form by multiplying both sizes with a trial function and integrating over each element.
- **Finite Difference Method:** This method uses the finite difference approximation for the derivative in the PDEs (Smith 1985). The derivation of FDM formulas typically starts with the Taylor series expansion of the solution. The accuracy and order of FDM depends on how many terms are retained in the Taylor series.

Note that these methods are used to address the spatial discretization. However, finite difference approximation is also mostly used for temporal discretization, for example, for those $\partial/\partial t$ and $\partial^2/\partial t^2$ terms in the PDEs. Mesh-based methods also include the spectral method, which is highly accurate but can only be used for certain shapes of domain (Gottlieb and Orszag 1977). Thus, it is suitable for fundamental research but not very popular for real-world applications.

For all mesh-based methods, the premise is of course a mesh to be generated for the simulation domain. There are two mesh types, namely structured and unstructured meshes. Structured meshes store the neighboring mesh information implicitly and efficiently through the storage order in computer memory. They do not require extra connectivity data to specify the neighborhood topology. Unstructured meshes are very flexible, and thus they can be used to describe complex domain geometries. On the other hand, unstructured meshes, also called irregular meshes, require explicit specification of connectivity of the mesh elements, such as points, lines, faces, and cells. The advantages of a structured

mesh include its simplicity and ease to achieve high-order accuracy. There is also a mixed mesh type, which contains both structured and unstructured zones. The mixed mesh type combines the strength of both types. However, it is not often used in popular CFD codes. Regardless of which type of mesh a CFD code uses, a high-quality mesh is a prerequisite to good simulation results. For a typical CFD job, the time and effort spent on the creation of valid and high-quality meshes are usually substantial. It is also worth noting that in computational science, the terms *mesh* and *grid* are used interchangeably.

Meshless (or meshfree) methods are rarely used in CFD codes for real-world applications. They are, however, gaining popularity in the research world. In these methods, since no mesh is needed, the effort for mesh generation can be spent on other aspects of the project. One of the acclaimed advantages of meshless methods is their flexibility for large deformations and problems with really complex geometries. One example of a meshless method is the smoothed-particle hydrodynamics (SPH). Since this book focuses on the traditional mesh-based methods, no further discussion is provided on the meshless methods.

4.1.3 Other Important CFD Concepts to Get Started

Other important concepts are useful for one to get started using CFD. In a short primer like this book, it is impossible and not necessary to provide all the details on CFD. The following is a list of these concepts:

- The first is the solution algorithms for the velocity–pressure coupling. The Navier-Stokes equations are a set of coupled equations for fluid velocity and pressure. Indeed, there is no specific governing equation for pressure that only appears in the momentum equation's pressure gradient term. As a result, the solution of pressure has to resort to the mass conservation equation. The governing equations are rarely solved in a coupled fashion. Instead, a sequential iterative scheme is typically used, where the velocity and pressure are solved in sequence and each iteration tries to improve the solution. Commonly used solution algorithms are called PISO, SIMPLE, and PIMPLE.
- Linearization of nonlinear PDEs is important for CFD solution. The momentum equations, such as Equation (4-2), in the Navier-Stokes equations are nonlinear because the advection of the momentum is caused by the velocity itself. Directly solving a nonlinear differential equation is difficult, if not impossible. Usually, a nonlinear term is linearized by treating part of the term using values at an old time step or previous iteration.
- Flows in many engineering applications are turbulent. Turbulent flow is a complex physical phenomenon that is still not fully understood. There is a range of scales in a turbulent flow, for example, large vortex to small eddies and anything in between. Direct simulation of all these scales is difficult because they require excessive computing power. Instead, turbulence in engineering applications is often modeled. Chapter 5 of this book gives an overview of turbulence modeling.

- After the governing equations are discretized with a numerical method, a system of linear equation is produced. The solution of these linear equation systems gives the scalar and vector values (e.g., pressure and velocity) at grid points or mesh cell centers. Many algorithms (solvers) are used to solve linear equation systems. They can be broadly categorized as direct solvers and iterative solvers. Direct solvers are not attractive for large linear systems. Most CFD codes use iterative solvers. The choice and performance of an iterative solver depend on the properties of the linear system. A residual criterion is necessary to terminate the iteration process. If the residual falls below the specified criterion within the prescribed maximum iterations, the solution is deemed converged. Otherwise, nonconvergence is assumed.
- Numerical error and order of accuracy. Numerical models can only give approximate solutions to the problems, and they inevitably introduce numerical errors. Numerical errors can be estimated by observing the order of accuracy of the numerical scheme used. A numerical scheme has nth-order accuracy if the error is proportional to the grid size to the power of n. For example, the error caused by a second-order scheme is proportional to the square of the grid size. In general, holding the grid size constant, the higher the order of accuracy, the smaller the numerical error. In practice, higher order schemes, for example, second-order schemes, are preferable. However, higher order schemes usually come with the price of less stability. A compromise is typically needed.

4.1.4 Brief History of CFD

It is beneficial to have an understanding of the history of CFD. This section is a synthesis of materials gathered from multiple sources, including Wikipedia, CFD-Online, and the website http://www.amwel.com. References are given where appropriate. Who first coined and used the term CFD is debatable (http://www.amwel.com/history.html). Legend has it that Lewis Fry Richardson (1881–1953) used a "human forecast-factory" to build the first numerical weather model. This model predated the existence of electronic computers. In such a "human" model, a large stadium was filled with tens of thousands of people. Each was given a mechanical calculator for the computation of flow in the assigned grid cells. A central commander used colored signal lights to coordinate the computation. This notion sounds amusing and a little absurd; however, it is the prototype of modern CFD, and the central idea is essentially the same.

In the modern sense, the first CFD simulation might be the flow around a cylinder in a work published in 1933 by A. Thom in his paper titled "The Flow Past Circular Cylinders at Low Speeds" in the *Proceedings of the Royal Society* (Thom 1933). For a novice in CFD, the flow around cylinder case may be the most popular tutorial case to learn a CFD code. Since the 1960s, the research in CFD has been propelled and accelerated by the advancement in computing power. The major contributors were the scientists and researchers at NASA, who were motivated to solve aerospace problems (http://www.amwel.com). Several great ideas and achievements in CFD techniques came from prominent NASA scientists

and research groups, for example, the particle-in-cell (PIC) method (Harlow 1955), the marker-and-cell (MAC) method (Harlow and Welch 1965), and the vorticity-stream function method (Fromm and Harlow 1963).

Later, developments in the decoupling of pressure–velocity and turbulence models greatly advanced the CFD field. To tackle the problem of pressure–velocity coupling, Brian Spalding at the Imperial College of London and his coworkers developed the semi-implicit method for pressure-linked equations (SIMPLE) algorithm, as well as its variants SIMPLE-Revised (SIMPLER) and SIMPLE-Consistent (SIMPLEC) (Patankar and Spalding 1972, Patankar 1980). A. Thom's 1933 calculation for flow around cylinder had a Reynolds number of only 60. Of more engineering interest is flow at high Reynolds number, that is, in the turbulent regime. A commonly used approach in engineering practice is the Reynolds-averaged Navier-Stokes (RANS) models. One such model, which is still widely used today, is the k-ε model (Jones and Launder 1972, Launder and Sharma 1974). The wide use of CFD beyond aerospace engineering and into other disciplines has cultivated a new CFD industry. Since the 1980s, commercial CFD codes have gradually become more accessible. Many of the early CFD software came out of government-sponsored research programs or research codes at universities. In the past couple of decades, some of these early codes still exist, whereas others ceased their development because of business acquisitions, closures, and other reasons. More recently, a new trend of free and open-source CFD codes has stirred the arena again and sparked more diverse development in almost all aspects of code development and application. A list of available CFD packages is provided in Section 4.3.

4.2 BASIC WORKFLOW OF CFD

4.2.1 Modeling Considerations

The idea of a computer model is to abstract the process of interest in the real world and translate that process mathematically in the form of equations (Figure 4-1). Typically, the equations are written based on conservation laws and other constitutive relations. For example, there are conservation laws for mass, momentum, and energy of fluids. There are also constitutive relations to describe, for instance, the behavior of fluids under the influence of stress (also known as rheological models). In the derivation of the mathematical model, assumptions and simplifications are often introduced because of the complexity of the problems in the real world. It is impossible to model everything. It is also not always necessary to consider every aspect of the problem. On the other hand, the assumptions have to be legitimate and physically representative, and they must be tested as well. The level of simplification should also be in a reasonable range such that it helps control the scope of a CFD project without neglecting important physics.

To derive or select a reasonable CFD model, one also needs to consider other aspects, for example, the dimensionality of the problem. One frequently asked

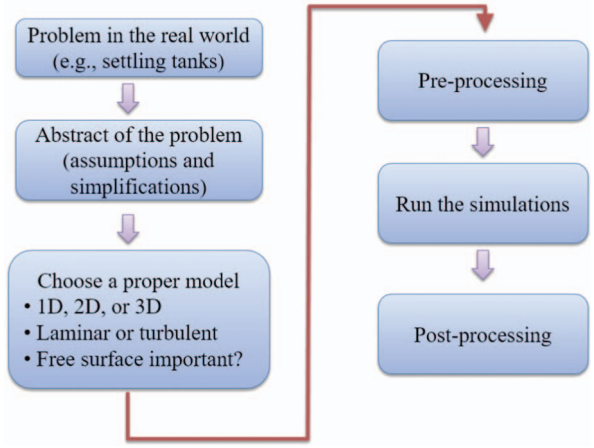

Figure 4-1. Workflow of a CFD project.

question is whether the processes should be modeled using 1D, 2D, or 3D space. The reduction of dimensionality can greatly lower the computational cost. Another important fluid flow characteristic to consider is whether the flow is turbulent or laminar. If it is turbulent, then how does one capture or model the turbulence? In water and wastewater hydraulics, many process units are chambers, tanks, or simply conduits, which have free surfaces. In this case, whether the free surface fluctuation needs to be considered in the model depends on how critical the free surface change is to the treatment process. For example, in a settling tank where the water surface is mostly flat and stable, the free surface might be well modeled with a shearless free-slip boundary. In other cases, for example, hydraulic jumps for mixing and aeration, or the stormwater inflow to a manhole, the free surface must be properly predicted by the model.

These considerations apply not only to CFD model developers, but also to users. The right decision on the selection of a proper model should be made based on understanding of the key processes. Sometimes, it is a balance between science and practical constraints. In reality, some iterations of model selection and fine tuning may be needed. From the beginning, and moreso recently, the boundary between developers and users is blurry because many commercial CFD codes provide function interfaces for customization and extension. These function interfaces provide users the access to internal data and control of the simulation process. For open-source CFD codes, the users have full access to every aspect of the source code and, therefore, have the freedom and full control to make modifications.

4.2.2 Steps in a Typical CFD Project

The first step in a CFD project is to define the problem and objectives and to make key assumptions based on the understanding of the process to be modeled. This first step is important in practice because it is the key to a successful CFD project.

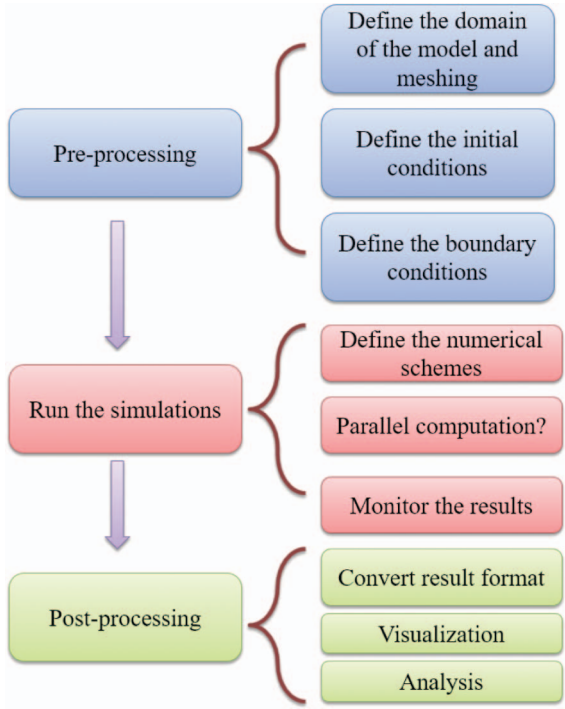

Figure 4-2. Typical steps in a CFD job.

This section assumes that this first step has been completed and a proper CFD model (code) has been selected. For a typical CFD simulation analysis, the basic workflow consists of at least three steps (Figure 4-2):

Preprocessing: In this step, the modeler needs to

- Specify the material properties of the fluid and other physical, chemical, and/or biological parameters;
- Specify turbulence parameters if the flow is turbulent;
- Delineate the simulation domain and generate the mesh. Geometry preparation and mesh generation are probably the most time-consuming and error-prone part of a CFD analysis for a complex real-world problem;
- Specify initial and boundary conditions;
- Set up solution and linear solver parameters, which include discretization schemes, relaxation parameters, and convergence tolerance;
- Specify simulation parameters such as time step size, simulation duration, and result output intervals; and
- Prepare for parallel computation if multiple computer cores are to be used. For example, if the CFD code uses the domain decomposition method for

parallel computation, the user typically needs to decompose the simulation domain into the desired number of subdomains.

Simulation: In this step, the simulation (either serial or parallel) is submitted and run on a designated computer system. For serial runs on a local machine, the submission is usually simple. For parallel runs on a high-performance cluster, a job script with a specified format is typically required. During the simulation, it is sometimes necessary to monitor the status of the job to detect and correct possible problems. Many CFD codes also provide run time modifiable functions to change a subset of the model parameters.

Postprocessing: In this step, analysis and visualization of the simulated results are performed. The specifics of postprocessing depend on the requirement of the CFD analysis, but typically include the following:

- Data extraction and evaluating the objectives;
- Error estimation and mesh independence studies: The simulation results should not depend on a mesh. In other words, the results should be mesh independent. Otherwise, the results are not reliable;
- Calibration and validation: Full confidence on the CFD results can only be gained through extensive calibration and validation. Typically, measurement data or theoretical results can be used for this task;
- Global flow parameter extraction, for example, flow rate, average effluent concentration, and settling tank efficiency;
- Flow field visualization, for example, vectors, contours, isosurfaces, streamlines, or stream ribbons. The main purpose is to help better understand the flow behavior; and
- Design option evaluation, for example, geometry or flow condition variations under different design options.

4.3 AVAILABLE CFD PACKAGES AND CODES

To carry out a CFD study, one needs not only a CFD solver but also a full package with a host of tools and software to complete the preprocessing, simulation, and postprocessing tasks. Not all available CFD packages have the complete set of tools. In some situations, even if a chosen CFD package has all the necessary functions to finish a CFD analysis, you may want to choose other software to perform a particular task. For example, one may find a specialized meshing software with some functionalities that make your preprocessing much easier. In this case, you can generate the mesh with this external software and then import it into your CFD package. Nevertheless, the general trend is that manufacturers of commercial CFD packages are racing to perfect their products so that their customers can rely solely on their revenue-generating packages.

In the next, the available software and choices for preprocessing, simulation, and postprocessing are listed. This list is by no means intended to be complete, and the order does not reflect or imply any preference or superiority.

4.3.1 Mesh Generation and Other Preprocessing Software

The following are commercially available mesh generation software:

1. Pointwise and Gridgen: http://www.pointwise.com/
2. GridPro: http://www.gridpro.com/
3. ANSYS Meshing and ICEM: http://www.ansys.com
4. HyperMesh: http://www.altairhyperworks.com/product/hypermesh

The following are open-source and freeware meshing software:

1. blockMesh, snappyHexMesh, and foamyHexMesh in OpenFOAM.
2. Gmsh: http://geuz.org/gmsh/, a 3D FEM mesh generator with built-in pre- and postprocessing capabilities.
3. Netgen: http://www.hpfem.jku.at/netgen/, an automatic 3D tetrahedral mesh generator. Geometric input supports constructive solid geometry (CSG) or boundary representation from STL file format (used for stereolithography).
4. Salome: http://www.salome-platform.org/, a generic platform for pre- and postprocessing for numerical simulation. It has a module for mesh generation.
5. enGrid: http://engits.eu/en/engrid, has native export to many CFD codes.

4.3.2 CFD Solvers

No two CFD solvers are exactly the same. However, the basic functionalities of CFD solvers should look similar. To consider the choice of a CFD solver for a particular problem, the following traits should be taken into account:

- Dimensionality of the computational domain: 2D planar, 2D axisymmetric, or 3D;
- Unstructured mesh (triangle and quadrilateral elements for 2D; tetrahedral, hexahedral, prism and pyramid elements for 3D) or structured mesh;
- Steady-state or transient flows or both;
- Compressibility: incompressible or compressible;
- Viscosity effect: inviscid or viscid (laminar and turbulent flows);
- Selection of turbulence models: RANS (k-ε, k-ω), DES, and LES;
- Rheology: Newtonian or non-Newtonian flows;
- Free-surface and multiphase models, including heat transfer and reactions;
- Lagrangian tracking of a dispersed phase, such as particles;

- Porous media flow model;
- Dynamic mesh capability for modeling flow around moving objects;
- Inertial (stationary) or noninertial (rotating or accelerating) reference frames;
- Multiple reference frame (MRF) and sliding mesh options;
- Volumetric sources of mass, momentum, heat, and chemical species;
- Material property database; and
- Extensive customization capability via user-defined functions (UDF, a nomenclature used in Fluent).

Commercially available CFD solvers include the following:

1. Ansys CFX,
2. Ansys Fluent,
3. Ansys CFD,
4. Star-CCM+,
5. COMSOL,
6. Phoenix,
7. Flow3D, and
8. NUMECA.

Open-source CFD solvers include the following:

1. OpenFOAM, by ESI group and OpenFOAM Foundation;
2. Gerris;
3. CFL3D, developed by NASA, only available to a "US person" within the United States;
4. OVERFLOW, by NASA;
5. TetrUSS, NASA (TETRahedral Unstructured Software System);
6. Delft3D, more specialized in such things as hydraulics and coastal flow; and
7. Telemac, also specialized in hydraulics problems.

As one can see, there are many choices in terms of CFD solvers. The criteria for selection should be based on the following considerations:

Functionality:

- Is there any particular process that you want to simulate? Check the advertised and user-endorsed features of each CFD package.
- Do you just need an off-the-shelf package, or do you want to do more secondary development? There might be some physical, chemical, and biological processes that are important to your project but not implemented in any CFD solver. In such a case, an extendable solver is necessary.

- Do you want a comprehensive package where preprocessing, solver, and postprocessing are bundled together? The trend is that most CFD software manufacturers try to provide a one-stop shop for everything you need. Thus, the selection of the CFD solver also needs to consider other parts of the packages.

Popularity and public acceptance:

- Consider what others are using in your field. It is much easier to compare studies if you use the same (or similar) software.
- How long has the package been around? Does it have a long and credible history?

Availability of technical support and training:

- In general, the support is much better for commercial packages since you are the paying customer.
- For open-source packages, the price you pay for freedom is less support. However, for popular open-source packages, the user base is getting bigger and there is always active online community support.

4.4 CHALLENGES AND OPPORTUNITIES

A user may face several technical challenges in CFD. The following is an incomplete list based on the author's experience:

- Mesh generation: It may be labor intensive when the simulation domain is complex. The generation of a high-quality mesh requires an experienced modeler. In recent years, the new trend in mesh generation software is automatic and requires less user interference. Many meshing software programs are also trying to integrate with CAD systems such that the change of a design can be automatically dealt with.
- As a simulation problem becomes bigger and more complex, the required computational power may increase dramatically. Despite the rapid increase of computing power in recent years, long simulation time is still a big concern for many CFD users.
- Engineers and designers are increasingly facing problems involving multiphysics, multiscales, multicomponents, and multidomains. To solve these problems, first the CFD packages need to be able to provide the necessary functionalities. Second, they need close collaboration between CFD modelers and domain experts.

Accompanying any challenge is an opportunity. CFD application in water and wastewater engineering is a great market and has tremendous potential to grow in the coming decades as the need to repair and rebuild aging infrastructure in many countries is ever growing. Researchers, CFD software manufacturers, practitioners,

regulators, and all other stakeholders should work together so that the CFD technique can be used properly to reduce cost, increase efficiency, and enhance safety.

References

Fromm, J. E., and F. H. Harlow. 1963. "Numerical solution of the problem of vortex street development." *Phys. Fluids* **6** (7): 975–982.

Gottlieb, D., and S. Orszag. 1977. *Numerical analysis of spectral methods: Theory and applications*. Philadelphia: SIAM.

Harlow, F. H. 1955. *A machine calculation method for hydrodynamic problems*. Technical Rep. No.LAMS-1956. Los Alamos, NM: Los Alamos National Laboratory.

Harlow, F. H., and J. Welch. 1965. "Numerical calculation of time-dependent viscous incompressible flow of fluid with a free surface." *Physics Fluids* **8** (12): 2182–2189.

Jones, W., and B. Launder. 1972. "The prediction of laminarization with a two-equation model of turbulence." *Int. J. Heat Mass Transfer* **15** (2): 301–314.

Launder, B., and B. Sharma. 1974. "Application of the energy dissipation model of turbulence to the calculation of flow near a spinning disc." *Lett. Heat Mass Transfer* **1** (2): 131–137.

Patankar, S. 1980. *Numerical heat transfer and fluid flow*. New York: Hemisphere Publishing.

Patankar, S., and D. Spalding. 1972. "A calculation procedure for heat, mass and momentum transfer in three-dimensional parabolic flows." *Int. J. Heat Mass Transfer* **15** (10): 1787–1806.

Smith, G. 1985. *Numerical solution of partial differential equations: Finite difference methods*. 3rd ed. Oxford, UK: Clarendon Press.

Thom, A. 1933. "The flow past circular cylinders at low speeds." *Proc. R. Soc. London, Ser. A* **141** (845): 651–669.

Versteeg, H., and W. Malalasekera. 2007. *An introduction of computational fluid dynamics: The finite volume method*. Essex, UK: Pearson Education.

Zienkiewicz, O., and R. Taylor. 1989. *The finite element method*. New York: McGraw-Hill.

This page intentionally left blank

CHAPTER 5

Turbulence-Resolving Methodologies and Turbulence Modeling

Andrés E. Tejada-Martínez

Most flows of interest in water and wastewater treatment are turbulent. This chapter reviews the three main methodologies for tackling turbulent flows with computational fluid dynamics (CFD), namely direct numerical simulation (DNS), Reynolds-averaged Navier-Stokes simulation (RANS), and large-eddy simulation (LES). Although the majority of CFD applications to water and wastewater treatment make use of the RANS approach, increasing computational resources should enable the application of LES and DNS in the future. The latter two would permit a fine-scale study and understanding of the turbulence in water and wastewater systems beyond the traditional RANS approach.

5.1 DIRECT NUMERICAL SIMULATION

The most brute force approach to turbulence is direct numerical simulation (DNS), in which all the scales of motion are simulated or resolved by the numerical method discretizing the Navier-Stokes equations. All turbulent flows are characterized by a wide range of spatial and temporal scales or eddies with the range increasing with increasing Reynolds number, Re. The Reynolds number is defined as $\mathrm{Re} = UL/\nu$, where U and L are characteristic flow velocity and length scales, respectively, and ν is kinematic viscosity. The Reynolds number is representative of the importance of inertial forces relative to viscous forces in a flow. In DNS, the computational grid must be sufficiently fine to capture the smallest scales, and the computational domain must be sufficiently large to capture the largest scales. Following Kolmogorov's theory (Piomelli 2001, Pope 2000, Hinze 1975), the ratio of the largest scales to the smallest (Kolmogorov) scales can be computed as $\mathrm{Re}^{3/4}$, where Re is the Reynolds number based on the

large-scale structures. Thus, to capture all the scales, a three-dimensional grid of approximately $\mathrm{Re}^{9/4}$ vertexes or grid points is required. The time step in DNS should be sufficiently small to capture the fast timescales associated with the smallest eddies. Considering the ratio of the timescale of the larger eddies of the flow to the timescale of the smallest eddies (i.e., the Kolmogorov timescale), the number of time steps required for a DNS scales as $\mathrm{Re}^{1/2}$. The total computational cost of DNS is defined as the total number of grid points multiplied by the number of time steps (Piomelli 2001). Thus, the total cost scales as $\mathrm{Re}^{11/4}$.

The computational expense of a DNS becomes greater than previously estimated for wall-bounded flows. The scaling for near-wall turbulent eddies is the viscous scale, defined as the kinematic viscosity divided by the wall friction velocity (Pope 2000). Considering this scaling together with the empirical result that the wall friction velocity goes as $UC_f^{1/2}$ where U is the free stream velocity away from the wall and the skin friction coefficient goes as $C_f \sim \mathrm{Re}^{-\alpha}$ with $\alpha = 0.2 - 0.25$, Piomelli (2001) estimates that the cost of a wall-bounded DNS translates to $\mathrm{Re}^{3.5}$.

Even though DNS is unsuited for most flows of interest because of its high computational expense, it can be useful for gaining insight into the physics behind turbulence in moderately low Reynolds number flows. Such information is required for the development of turbulence and subgrid-scale models or closures used in the RANS and LES methodologies, respectively. Some of the early well-known DNS simulations include the turbulent channel flow simulation of Kim et al. (1987) and the turbulent flow over a backward-facing step of Le et al. (1997). Both studies were originally conducted to gain new insight into the physical mechanisms involved in turbulent flows and have been often used to validate RANS and LES and their respective closures.

Because the DNS approach is too computationally expensive for most turbulent flows, early scientists had to find different approaches. If a full description of all scales in a turbulent flow is not possible, it is possible to derive equations that govern the large scales, while the effect of the smaller scales on the large ones is modeled. The first of such approaches is RANS. as described in the next section.

5.2 REYNOLDS-AVERAGED NAVIER-STOKES SIMULATION

Irregularity is one of the most striking features of turbulent flows. Even though it seems impossible to describe the turbulent motion in all details as a function of time and space coordinates, it appears possible to indicate average values of the flow variables (velocity and pressure). As pointed out by Hinze (1975), mere observation of turbulent flows and time histories of turbulent quantities show that these averages exist because of the following reasons: (1) At a given point in the turbulent flow domain, a distinct pattern is repeated more or less regularly in time, and (2) at a given instant, a distinct pattern is repeated more or less irregularly in space. So turbulence, broadly speaking, has the same overall structure throughout the domain

considered. Furthermore, although general assumptions regarding the behavior of the smallest scales lead to turbulence closure models, details of the motion at this level are not of interest for most applications in engineering and geophysics. Motivated by the latter, Osborne Reynolds developed a statistical approach in 1895 and derived the famous equations that bear his name to describe the dynamics of the mean or average flow, otherwise the largest, most energetic of the scales.

Formally, the Reynolds equations are obtained from the Navier-Stokes equations by decomposing the velocity $\mathbf{u}(u_1, u_2, u_3)$ and the pressure p into mean (average) and fluctuating components as $\mathbf{u} = \langle \mathbf{u} \rangle \mathbf{u}'$ and $p = \langle p \rangle + p'$, where the brackets denote the means and the primes denote the fluctuations reflecting the turbulent intensities of $\mathbf{u}$ and p. The previous decomposition is referred to as the Reynolds decomposition. There are essentially two ways to define the mean components in this decomposition. These are ensemble averaging and time averaging.

Ensemble averaging is done by performing many physical experiments on the same problem, measuring the velocity and pressure at every time and at every point in the domain, and then averaging over this set of experimental data. Ensemble averaging can be done via multiple realizations of a physical experiment or via multiple computational simulations, with white noise introduced into the problem data, such as boundary and initial conditions.

Time averaging was Reynolds's original approach; he defined the mean flow variables as

$$\langle \mathbf{u} \rangle (t, \mathbf{x}) = \int_t^{t+T} \mathbf{u}(\lambda, \mathbf{x}) d\lambda \text{ and } \langle p \rangle (t, \mathbf{x}) = \int_t^{t+T} p(\lambda, \mathbf{x}) d\lambda \qquad (5\text{-}1)$$

The timescale T has to be sufficiently long that choosing a larger timescale would produce the same mean components. At the same time, T should be short enough relative to temporal variations in the mean not associated with the turbulence. In the case of statistically steady flows, the mean quantities are time independent.

Substitution of the Reynolds decomposition into the Navier-Stokes equations leads to the well-known Reynolds-averaged Navier-Stokes equations. These are of the same form as the original Navier-Stokes equations, except that they describe the behavior of $(\langle \mathbf{u} \rangle, \langle p \rangle)$ instead of $(\mathbf{u}, p)$. Furthermore, in addition to the mean viscous stress (given through Newton's law of viscosity in the case of a Newtonian fluid), the Reynolds-averaged Navier-Stokes equations also possess a second stress, namely the Reynolds stress, representing the influence of the fluctuating components (i.e., the turbulence) upon the mean flow components. The Reynolds stress is a tensor or matrix whose components are defined as $-\langle u_i' u_j' \rangle$ with $i, j = 1 \ldots 3$, denoting the individual entries of the tensor. The Reynolds stress tensor requires knowledge of the velocity fluctuations, an unknown entity since the intent is to solve for the mean component of the flow as governed by the Reynolds-averaged Navier-Stokes equations. This situation presents what has classically been termed a *closure problem*, wherein a turbulence closure or model needs to be applied to approximate the Reynolds stress tensor.

The most popular turbulence models approximate the Reynolds stress tensor in terms of an eddy viscosity and the gradient of the mean velocity. The eddy viscosity is expressed, for example, in terms of the turbulent kinetic energy (TKE) and TKE dissipation rate in the case of the well-known k-epsilon (or k-ε) model, where TKE and TKE dissipation rate are obtained from their respective differential transport equations (Pope 2000, Andersson et al. 2012). Other more computationally expensive models exist for which the Reynolds shear stress components are solved directly from their corresponding differential transport equations. In contrast, the least computationally expensive models are often called zero-equation models. In these models, the eddy viscosity is given through an algebraic expression instead of solving differential transport equations.

Table 5-1 provides a list of popular turbulence models, including their strengths and weaknesses. Details of these models and their application to wastewater are summarized by Karpinska and Bridgeman (2016). Additional information about these models can be found in Wilcox (1994), Pope (2000), and Andersson et al. (2012).

In summary, RANS entails the numerical solution of the Reynolds-averaged Navier-Stokes equations with the Reynolds stress, appearing on the right-hand side of these equations, approximated via a turbulence model. The solution of these equations yields the behavior of the larger, more energetic components of the flow, given through the mean flow components ($\langle \mathbf{u} \rangle$,$\langle p \rangle$). For example, Figure 5-1 presents the mean flow solution obtained via RANS for a flow through a laboratory-scale serpentine contactor computed by Zhang et al. (2012). The RANS solution consists of the principal recirculation zones within each contactor chamber, while in contrast, the more computationally expensive LES solution (also shown in Figure 5-1) is seen to capture smaller eddies embedded within the principal recirculation zones. Figure 5-2 presents the RANS solution structure for a turbulent jet in comparison to respective LES and DNS solutions. As can be seen, the RANS solution does not resolve the turbulence fluctuations, which makes it a more computationally efficient approach; however, the solution does not provide a complete perspective. Nevertheless, a RANS solution often provides information about the flow of interest to engineers such as the baffling factor (i.e., the t10 index) in the flow through the serpentine contactor and the width of the turbulent jet in Figures 5-1 and 5-2.

In RANS, the turbulent fluctuations and associated turbulent eddies are not resolved (i.e., solved for), unlike in the more expensive approaches LES and DNS. Thus, the RANS computational grid can be much coarser than DNS and LES grids. However, the main disadvantage in RANS is that the solution depends strongly on the turbulence model chosen, and no universal turbulence model exists. That is, turbulence models that perform well for certain classes of problems may not perform as well for others (Table 5-1). Thus, when performing CFD analyses based on the RANS methodology, it is strongly recommended that researchers validate their CFD models via comparison with physical experiments if possible, check the dependence of their results on the turbulence model chosen by rerunning the simulations with different turbulence models, and perform grid resolution studies ensuring that their solutions are not affected adversely by grid refinement.

Table 5-1. Advantages and Disadvantages of Popular Turbulence Models for RANSS

Model	*Advantages*	*Disadvantages*
Prandtl's mixing-length model	Cost-effective	Limited to simple flows (e.g., predicted eddy viscosity vanishes with the mean velocity gradient)
Standard k-ε (sk-ε)	Excellent performance for many flows. Well established in academia and industry. Robust, economical in terms of computational effort and satisfactory accuracy in diverse turbulent flow issues.	Poor performance in some scenarios (e.g., strong streamline curvature, vortexes, rotating flows, flow separation, and adverse pressure gradients). Assumes locally isotropic turbulence. Poor prediction of the lateral expansion in 3 D wall jets.
Renormalized group (RNG) k-ε	Improved performance for swirling and high strained flows compared to sk-ε.	Less stable than sk-ε.
Realizable k-ε	Suited for planar and rounded jets, swirling and separated flows, and wall-bounded flows with strong adverse pressure gradients.	Not recommended for use with multiple reference frames.
Standard k-ω	Valid throughout to boundary layer, subject to fine grid resolution. Accounts for the streamwise pressure gradients. Applicable for detached, separated flows and fully turbulent flows.	Pressure-induced separation is typically predicted to be excessive and early.

(Continued)

Table 5-1. Advantages and Disadvantages of Popular Turbulence Models for RANSS (Continued)

Model	*Advantages*	*Disadvantages*
Shear stress transport (SST) k-ω	The most accurate of the two-equation eddy viscosity models. Suitable for adverse pressure gradients and pressure-induced flow separation. Accounts for the transport of the principal shear stresses.	Less suitable for free shear flows.
Reynolds stress model (RSM)	Accurate calculation of the mean flow properties and all Reynolds stresses through corresponding transport equations. Accounts for the streamline curvature, rotation, and rapid changes in strain rate, yielding superior results to two-equation models for complex flows (e.g., with stagnation points).	Computationally expensive. Not always more accurate than two-equation models. Harder to obtain converged result. Reliability of RSM predictions is still limited by the closure assumptions used to model pressure-strain and dissipation-rate terms in the Reynolds stress transport equations.

Source: Data from Karpinska and Bridgeman (2016) and Andersson et al. (2012).
Note: Terms in the model names are as follows: k is turbulent kinetic energy, ε is dissipation rate of turbulent kinetic energy, and ω is the specific rate of dissipation of turbulent kinetic energy. More details regarding these models can be found in the previously listed references, as well as Pope (2000) and Wilcox (1994).

5.3 LARGE-EDDY SIMULATION

In the large-eddy simulation (LES) approach to turbulence, a low-pass, local, spatial filter is applied to the Navier-Stokes equations, instead of an ensemble or temporal average. Spatial filtering decomposes the variables into two components as $\mathbf{u} = \overline{\mathbf{u}} + \overline{\mathbf{u}}'$ and $p = \overline{p} + \overline{p}'$ where $\overline{\mathbf{u}}$ and $\overline{p}$ are the resolved (locally smoothed)

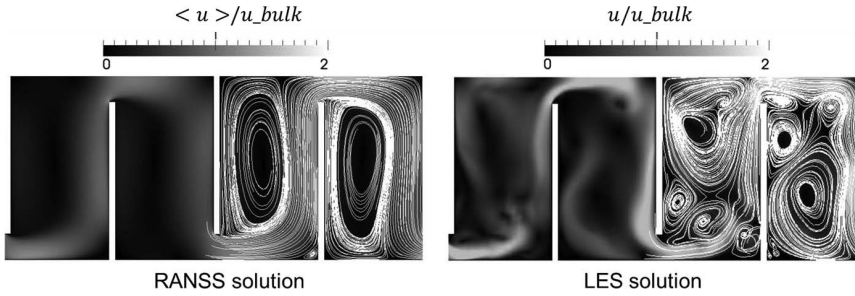

Figure 5-1. Comparison of mean (RANSS) and instantaneous (LES) speed and corresponding streamlines obtained from RANSS and LES through a laboratory-scale serpentine contactor. Velocities are scaled by bulk velocity.
Source: Zhang et al. (2012).

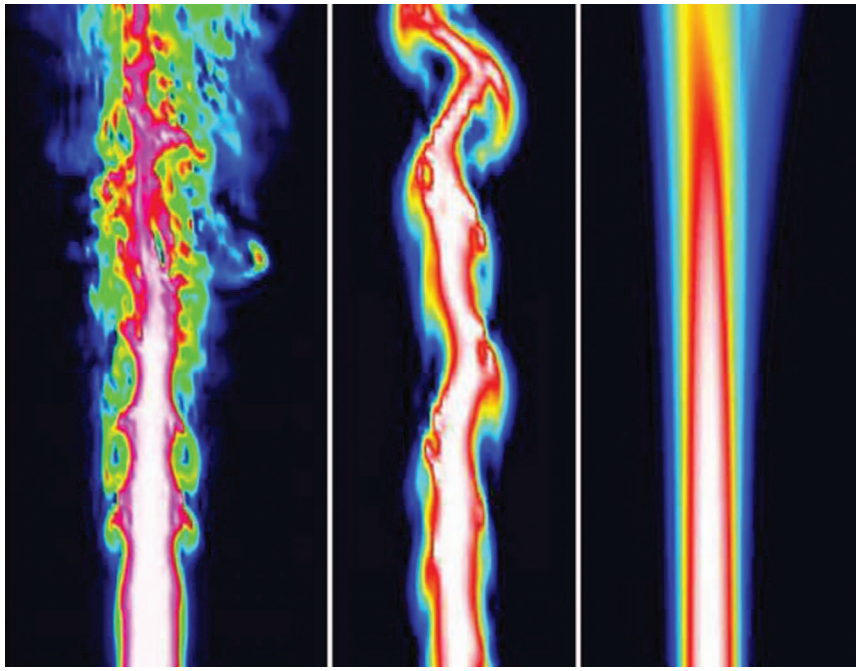

Figure 5-2. Turbulent jet structure as calculated via DNS (left panel), LES (middle panel), and RANSS (right panel).
Source: Maries et al. (2012), reproduced with permission from Springer.

flow components and u' and $\overline{p}'$ are the residual (smaller) components. Filtering the Navier-Stokes equations leads to equations governing the resolved components $(\overline{\mathbf{u}}, \overline{p})$. The filtered equations are of the same form as the original unfiltered Navier-Stokes equations, except that they are in terms of $(\overline{\mathbf{u}}, \overline{p})$ instead of the

unfiltered variables ($\mathbf{u}, p$). Furthermore, in addition to the filtered viscous stress term, the filtered Navier-Stokes equations possess a second stress, namely the residual stress, representing the influence of the small (residual) unresolved components upon the resolved (larger) ones. The residual stress tensor is defined as $\tau_{ij} = \overline{u}_i\overline{u}_j - \overline{u_i u_j}$. The residual stress requires knowledge of the unfiltered velocity $\mathbf{u} = (u_1, u_2, u_3)$, presenting a closure problem because the intent in LES is to solve the filtered equations, which yield $\overline{\mathbf{u}}$ and not $\mathbf{u}$. Thus, to obtain a closed system, the residual stress tensor, τ_{ij}, must be modeled or approximated. Note that in practice, in classical LES, the filter is assumed implicitly by the numerical discretization in conjunction with the computational grid, thus often the resolved velocity $\overline{\mathbf{u}}$ is referred to as the grid-scale velocity and the residual stress is referred to as the subgrid-scale (SGS) stress. LES consists of the numerical solution of the filtered Navier-Stokes equations with modeled SGS stress for the grid-scale components ($\overline{\mathbf{u}}, \overline{p}$).

Based on the discussion above and the comparison in Figure 5-2, LES can be considered a compromise between DNS and RANS (Pope 2000). In LES, the computational grid is sufficiently fine to resolve a significant range of the turbulence, unlike in RANS (e.g., Figure 5-3), but it is not fine enough to resolve the smaller energy-dissipating motions, as in DNS. As such, the computational cost of LES lies somewhere between the costs of RANS and DNS. Furthermore, given that LES resolves a significant portion of the turbulent scales, results depend less on the model of the unresolved scales (i.e., the SGS stress model) than in RANS (i.e., the turbulence model).

In LES, the larger eddies of the turbulence are computed directly, while the effect of the smaller SGS eddies on the larger resolved eddies is modeled through the SGS stress. The SGS eddies have a universal character (i.e., the SGS eddies behave similarly in all turbulent flows); thus, the effect of these eddies should be capable of being represented by an SGS stress model suitable for any turbulent flow. Conversely, the larger eddies in a turbulent flow are widely believed to be deterministic, and hence predictable, once the effects of the smaller eddies on them are known. Furthermore, these larger eddies are often the most important flow structures and carry the most energy. These notions provide the foundation

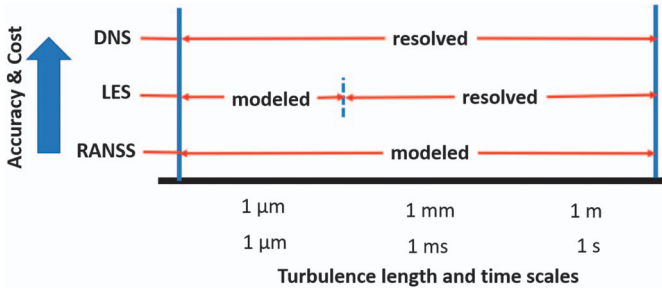

Figure 5-3. Comparison of turbulence resolution (length and time scales), accuracy, and computational cost in DNS, LES, and RANS simulation (i.e., RANSS).

for LES: to model the mean effects of the small scales on the larger ones based on the universal features of the former, and then numerically to simulate the motion of the latter.

The main objective in modeling the effects of the smaller SGS scales on the larger scales is to provide proper energy dissipation. As first proposed by Kolmogorov (Pope 2000), the role of the smallest of the scales is to receive energy transferred from the larger scales and dissipate this energy in the form of heat through viscous effects. The energy-dissipating small scales are not present in (or are not admitted by) the filtered equations; thus, without a model to account for dissipation associated with these small scales, the filtered equations would give rise to an accumulation of energy in the smallest resolved scales. Modeling the dissipative mechanism of the smallest scales is based on their universality as well as the universality of the midrange scales of the turbulence. This midrange is often referred to as the *inertial range*. The sole purpose of the scales in the inertial range is to transfer energy from the energy-containing larger scales down to the dissipative (smallest) scales. All turbulent flows possess an inertial range where the energy contained in the scales in this range decreases as the size of the scales decreases, following a –5/3 power law behavior (Figure 5-4). This behavior was originally hypothesized by Kolmogorov and proved experimentally a number of times, for example, see Sreenivasan (1995). The size of the inertial range increases with increasing Reynolds number. Ideally, the smallest of the resolved scales in LES should fall within the inertial range, as highlighted in Figure 5-4. Popular models of the SGS stress in the LES equations such as the well-known eddy viscosity-based Smagorinsky model (Smagorinsky 1963) assume that the LES grid resolves down to the inertial range while making use of the universality of scales

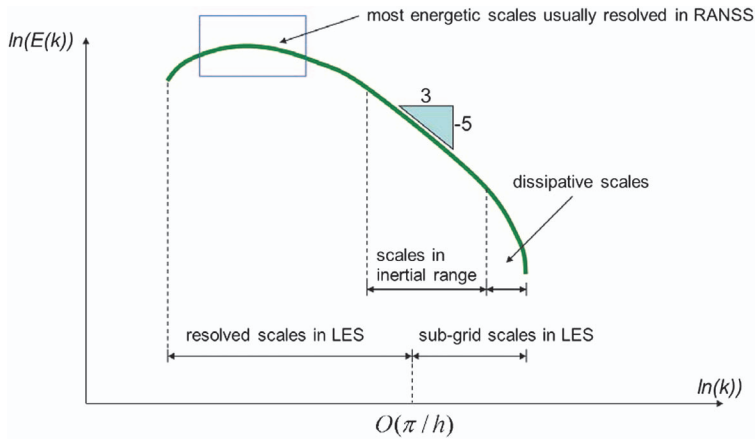

Figure 5-4. Sketch of typical energy spectrum in a turbulent flow. The energy is shown versus wavenumber, k*, which is inversely proportional to length scale. LES resolves the energy spectrum up to the filter cutoff implicitly set by the numerical discretization and computational grid cell size,* h.

within the inertial and the energy-dissipating smaller scales in order to account for the proper energy dissipation in the filtered Navier-Stokes equations.

As noted by Piomelli (2001), away from a solid surface, resolution of the inertial range required for LES is nearly independent of the Reynolds number. However, this is not the case near a wall or solid surface, where the size of the more energetic eddies resolved in the LES decreases with the distance to the surface. The resolution required to resolve the viscous sublayer next to a solid surface scales as $Re^{1.8}$, and the resolution needed for the outer boundary layer scales as $Re^{0.4}$, as estimated by Chapman (1979). Thus, although LES offers computational savings relative to DNS, it can still prove expensive for flows with boundary layers.

LES in which the dynamics of the turbulence next to a solid surface (e.g., a wall) are resolved is often referred to as wall-resolved LES. In these cases, the computational grid is required to resolve the viscous sublayer next to the wall, and thus the grid is typically designed such that the wall-normal distance to the first grid point is at a distance $y^+ \approx 1$ from the wall. In the previous expression, y^+ is the dimensionless wall-normal distance to the wall in so-called *wall units*. More specifically, $y^+ = yu_\tau/\nu$, where y is the dimensional wall-normal distance to the wall, u_τ is the wall friction velocity (defined as the square root of the wall shear stress scaled by density), and ν is kinematic viscosity. Following the law of the wall, the viscous sublayer occupies the range $y^+ < 5$, the buffer layer is within the range $5 < y^+ < 30$, and the log layer is within $30 < y^+ < 300$.

5.4 WALL TREATMENT AND HYBRID RANS-LES TECHNIQUES

To reduce the computational expense associated with the boundary layer next to a solid surface boundary or wall, LES and RANS are often enhanced by wall treatments. In this case, the mesh adjacent to the boundary is left intentionally coarse. More specifically, the first grid points off the boundary are taken to be within the log layer. Thus, the mesh does not resolve the viscous sublayer nor the buffer layer. The computed velocity at the first grid points off the boundary is assumed to satisfy the classical log law, which provides an expression for the velocity scaled by the wall friction velocity. The latter is then used to solve for the friction velocity and ultimately the wall shear stress (defined as the square of the friction velocity multiplied by the density). Finally, instead of imposing the no-slip condition, the wall shear stress is imposed as the boundary condition at the wall. A review of this approach and its variants often used in LES is given by Piomelli and Balaras (2002). Similar wall treatments are also adopted for RANS, including making use of boundary conditions, for example, for TKE and the TKE dissipation rate, consistent with log-layer theory, in the case of the *k*-epsilon turbulence model (Bredberg 2000).

Variants of LES with wall modeling consist of the hybrid RANS-LES approaches in order to deal with the expensive near-wall dynamics. There are two main classes of hybrid RANS-LES techniques, namely global and hybrid

(Sagaut and Deck 2009). In the hybrid approach, the computational domain is partitioned into an LES zone and a RANS zone, where a pure LES solution is computed in the LES zone and a pure RANS solution is computed in the RANS zone. The solution algorithm should be able to handle the interchange of these solutions across the zones. Meanwhile in the zonal approach, there is no clean partitioning of the domain into RANS and LES zones, but rather the solution is strictly hybrid, neither purely LES nor purely RANS, making it difficult to interpret the turbulence being resolved as the solution becomes closer to that of LES.

5.5 SUMMARY

The three main approaches to tackling turbulent flows have been reviewed, namely DNS, LES, and RANS. DNS is the most natural approach, in which almost 100% of the turbulence is resolved, thus requiring no turbulence closure or modeling. However, given that DNS resolves all the turbulence, it requires fine grids to capture the energy-dissipating Kolmogorov spatial scales and timescales, which can be as small as micrometers and microseconds (Figures 5-2 and 5-3). These scales make DNS unfeasible for most turbulent flows; thus, other approaches have been devised. In the RANS approach, the grid resolves only the mean component of the flow, and the effect of the unresolved turbulence on the computed mean flow is accounted for through a turbulence model. As such, RANS solutions can be heavily dependent on the turbulence model. LES is intermediate to RANS and DNS. In LES, a wide range of the turbulent scales is resolved (typically accounting for about 80% of the total turbulent energy). Thus, LES requires finer grids than RANS yet coarser grids than DNS. The savings afforded by LES are tempered in wall-bounded flows, where capturing the more energetic scales of the turbulence can make the computation unfeasible as the size of these scales decreases with distance to the wall. To bypass this difficulty, LES is often applied with wall modeling in which the near-wall mesh is intentionally made coarse and the viscous sublayer and buffer layer are not resolved. Instead of imposing the no-slip condition, the wall shear stress is imposed, with the wall shear stress estimated by assuming that the computed LES velocity at the first grid points off the wall satisfies the classical log law. Similar approaches have been devised for RANS to avoid expensive resolution of high-velocity gradients in wall-bounded flows. Hybrid RANS-LES approaches have been proposed as alternatives to deal with the expensive near-wall region.

As noted earlier, most computations of flow in water and wastewater treatment involve RANS because typically this solution methodology is sufficient to provide results of engineering interest. For example, Zhang et al. (2012) have shown that RANS with appropriate wall treatments is able to predict residence time statistics such as the baffle factor on par with LES. An attribute of turbulence-resolving simulations, such as LES and DNS, is that they can provide insight into

the physics of the turbulence. Of particular interest to the water and wastewater community is the turbulence interaction with chemical and biological reactions often occurring in water and wastewater treatment processes. LES and DNS can shed light on turbulence-chemistry and turbulence-biology interactions, potentially leading to their accurate closures in the Reynolds-averaged transport equations for chemical and biological species concentration (Zhang et al. 2014).

References

Andersson, B., L. Hakansson, M. Mortensen, S. Rahman, and B. van Wachem. 2012. *Computational fluid dynamics for engineers*. Cambridge, UK: Cambridge University Press.

Bredberg, J. 2000. *On wall boundary conditions for turbulence models*. Technical Rep. Gothenburg, Sweden: Chalmers Univ. of Technology.

Chapman, D. R. 1979. "Computational aerodynamics development and outlook." *AIAA J.* **17** (12): 1293–1313.

Hinze, J. 1975. *Turbulence*. New York: McGraw-Hill.

Karpinska, A. M., and J. Bridgeman. 2016. "CFD-aided modelling of wactivated sludge systems: A critical review." *Water Res.* **88**: 861–879.

Kim, J., P. Moin, and R. Moser. 1987. "Turbulent statistics in fully developed channel flow at low Reynolds number." *J. Fluid Mech.* **177**: 133–166.

Le, H., K. Moin, and J. Kim. 1997. "Direct numerical simulation of turbulent flow over a backward-facing step." *J. Fluid Mech.* **330**: 349–374.

Maries, A., M. A. Haque, S. L. Yilmaz, M. B. Nik, and G. E. Marai. 2012. "Interactive exploration of stress tensor used in computational turbulent combustion." In *New developments in the visualization and processing of tensor fields*, 137–156. Berlin: Springer.

Piomelli, U. 2001. "Large eddy and direct simulation of turbulent flows (short course notes)." In *Proc., 9th Annual Conf. of the CFD Society of Canada*, 1–60. Kitchener, Canada: CFD.

Piomelli, U., and E. Balaras. 2002. "Wall-layer models for large-eddy simulations." *Ann. Rev. Fluid Mech.* **34** (1): 349–374.

Pope, S. 2000. *Turbulent flows*. Cambridge, UK: Cambridge University Press.

Sagaut, P., and S. Deck. 2009. "Large eddy simulations for aerodynamics: Status and perspectives." *Philos. Trans. R. Soc. London, Ser. A* **367** (1899): 2849–2860.

Smagorinsky, J. 1963. "General circulation experiments with the primitive equations." *Mon. Weather Rev.* **91** (3): 99–152.

Sreenivasan, K. R. 1995. "On the universality of the Kolmogorov Constant." *Phys. Fluids A* **7** (11): 2778–2784.

Wilcox, D. C. 1994. *Turbulence modelling*. La Cañada, CA: DCW Industries.

Zhang, J., A. E. Tejada-Martinez, and Q. Zhang. 2012. "Reynolds-averaged Navier-Stokes simulation of the flow and tracer transport in a multichambered ozone contactor." *J. Environ. Eng.* **139** (3): 1150–1157.

Zhang, J., A. E. Tejada-Martinez, and Q. Zhang. 2014. "Developments in computational fluid dynamics-based modeling for disinfection technologies over the last two decades: A review." *Environ. Modell. Software* **58**: 71–85.

CHAPTER 6

Preprocessing

Ruo-Qian Wang
Faissal R. Ouedraogo
Subbu-Srikanth Pathapati

6.1 CONVERT AN ENGINEERING PROBLEM INTO A CFD CASE

Translating an engineering problem into a computational fluid dynamics (CFD) case is the most important step in the usage of CFD to ensure that the CFD model is representative of the engineering problem under investigation. The following are some main components required for a CFD case, and they should be determined from the analysis of the engineering problem:

1. **The Domain of Study and Problem Definition**
   It is crucial to define the domain of study clearly before starting CFD analysis. The modeler should start with clear goals in mind and then proceed with the appropriate simplifications before creating the geometry for modeling. Some important aspects to check are as follows:
   - Can the engineering problem be represented by 2D simulations or is a 3D model required?
   - Can the engineering problem be treated as a steady-state problem, or is it necessary to model time dependence?
   - Is there geometric symmetry in the engineering problem that allows for modeling half the domain?
   - Think ahead with regard to the extent of the model domain, for instance, where inlets and outlets are to be placed to avoid inaccurate results.
2. **Material Properties**
   Appropriate material properties should be assigned to the fluids and solids being modeled. Some common properties are density and viscosity for fluids and specific gravity and particle diameter for solids.

3. **Boundary Conditions and Operating Conditions**
   Boundary conditions refer to specific quantities, such as mass flow rates, volumetric flow rates, velocity magnitude, turbulence quantities, volume fractions, and species concentrations, which are set by the modeler at the boundaries in the computational domain. Common boundary conditions in most CFD codes are "mass flow inlet," "pressure inlet," "pressure outlet," "velocity inlet," and "wall," among many others. Operating conditions for the entire computational domain include quantities such as reference pressure, gravity, and temperature.
4. **Initial Conditions**
   For transient CFD simulations, initial conditions refer to the status (e.g., velocity, pressure, and temperature) of fluids at the beginning of the simulation period. The initial conditions also determine the status of the fluid in the domain of study, such as whether the domain is empty or full, or whether the fluid is in motion at the beginning of the simulation. Initial conditions are critical because not only do they have great influence on results, but they also dictate how long the simulation needs to run.
5. **Physical and Chemical Processes**
   For CFD modeling of water and wastewater treatment, it is important to understand the physical (e.g., convection or diffusion) and chemical (e.g., reaction kinetics or rates) processes thoroughly before starting the modeling process. The modeler must be able to determine if and when simplification of the process is possible. The chosen processes to be modeled dictate the type of CFD solver and the potential changes to be made to that solver.

Once these five components are identified from the engineering problem, the CFD model process can be started. The next step is to create the geometry, as a boundary of the problem domain, using a computer-aided design (CAD) software package. After the geometry is created, the meshing process can begin.

6.2 MESHING AND MESHING TOOLS

Meshing, also called *mesh generation* and *grid generation*, is an essential step of preprocessing and is critical to the success of a CFD analysis. CAD files in various formats, including but not limited to .stl or .vtk files, are read into the appropriate meshing software.

A mesh can be categorized according to different criteria. Regarding the cell type, the mesh can be classified into triangle and quadrilateral meshes in a 2D domain, and tetrahedral, pyramid, triangular prism, or hexahedral meshes in a 3D domain.

In terms of cell connectivity, a mesh can be classified into structured, unstructured (also called flexible mesh), or hybrid mesh. A structured mesh has

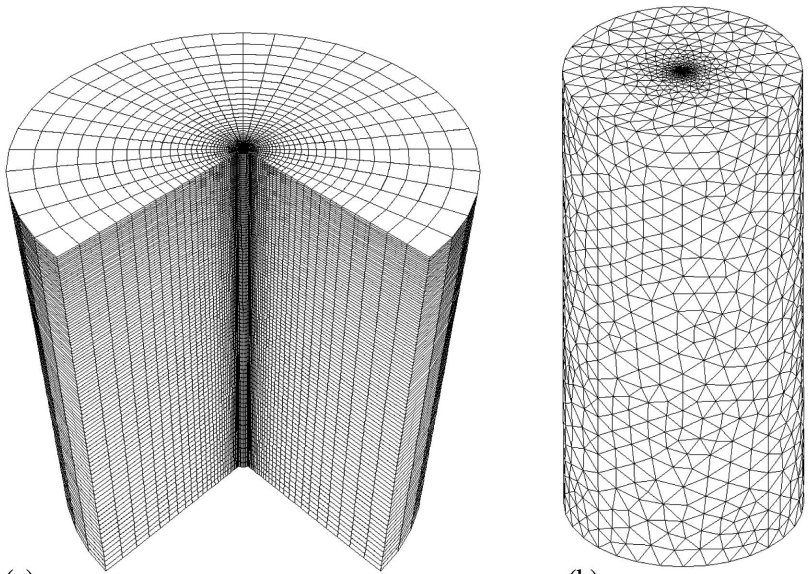

Figure 6-1. Types of mesh: (a) structured mesh, (b) unstructured mesh.
Source: Part (a): Wang et al. 2015.

an orthogonal arrangement of the computing cells (e.g., Figure 6-1a) and is highly efficient in computation and memory storage. Structured mesh can be further classified according to its general configuration, including three basic types: H-grids, O-grids, and C-grids. In comparison, unstructured meshing is often applied to complex geometries where it is impractical and often infeasible to use structured meshes. Unstructured meshing needs to be performed with care, and the modeler should make the appropriate adjustments during the solution process to minimize errors.

A hybrid mesh or a blocked mesh is a combination of unstructured and structured meshing. An example of unstructured mesh is depicted in Figure 6-1b. More details can be found in mesh generation books (e.g., Thompson et al. 1998).

The quality of the mesh is critical to obtaining a converged CFD solution. Some basic mesh quality concepts are described here to help guide the general direction of mesh improvement.

Skewness is a general indicator of mesh quality. There are various definitions of skewness—a straightforward definition applicable to triangles and tetrahedrons is based on the size of equilateral shapes, that is,

$$\text{Skewness} = (\text{optimal cell area} - \text{cell area})/(\text{optimal cell area}) \qquad (6\text{-}1)$$

where an optimal cell is the equilateral triangle that shares the same circumscribed circle or the equilateral tetrahedral that shares the same circumscribed sphere.

Smoothness describes the change in size from cell to cell. There should not be sudden jumps in the size of the cell because this may cause erroneous results at nearby nodes.

Aspect ratio is the ratio of the longest to the shortest side in a cell. Ideally, it should be equal to 1 to ensure the best results. Also, local variations in cell size should be minimal, that is, adjacent cell sizes should not vary beyond 20%. Having a large aspect ratio can result in interpolation error.

When modeling turbulent flow in internal and external flow, an important concern for the modeler is to ensure that the mesh is fine near the solid surface, such as the wall of a pipe, where turbulent boundary layers develop. The dimensionless parameter y^+ is used as a guide for determining boundary layer mesh thickness. y^+ is defined as $y^+ = (yu^\star)/\upsilon$ where y is the first grid distance to the solid surface, υ is the kinetic viscosity, and $u^\star$ is the shear velocity. A general rule of thumb is to calculate boundary layer thickness with the goal of keeping the y^+ value in the range of 30 to 300. Detailed discussion about wall functions and turbulence modeling is in Chapter 5.

Global mesh size and local refinement depend on the specific engineering problem. It is often true that mesh generation is the most time-consuming step in a CFD analysis. From the perspective of final CFD results, the time invested in this step is worthwhile, though, because mesh quality is usually the bottleneck of the complete CFD simulation.

A mesh generation tool is usually an embedded component in a commercial CFD package. Open-source CFD solvers usually rely on simple accessory meshing codes or third-party software. For example, OpenFOAM contains blockMesh and snappyHexMesh codes to generate simple meshes. But OpenFOAM can also read the meshes from other mesh generators, including ANSYS meshing. It is a general trend that open-source CFD codes support more mesh file formats. Many companies and research organizations are still actively developing new meshing tools. A detailed list can be found at https://www.cfd-online.com/Links/soft.html#mesh.

References

Thompson, J. F., B. K. Soni, and N. P. Weatherill, eds. 1998. *Handbook of grid generation*. Boca Raton, FL: CRC Press.

Wang, R. Q., E. E. Adams, A. W. K. Law, and A. C. Lai. 2015. "Scaling particle cloud dynamics: From lab to field." *J. Hydraul. Eng.* **141** (7): 06015006.

Wang, R. Q., A. W. K. Law, and E. E. Adams. 2013. "Large eddy simulation of starting and developed particle-laden jets." In *Proc, 8th Int. Conf. on Multiphase Flow*, Japan Society of Multiphase Flow: Osaka, Japan.

CHAPTER 7
Postprocessing

Ruo-Qian Wang

Once the results from computational fluid dynamics (CFD) simulations are available, we need to visualize and analyze the output to extract information. *Visualization* is a subject focusing on realistic renderings of volumes, surfaces, illumination sources, and so forth with or without a dynamic (transient) component. The common means are color plots, animations of vector fields, contours, isosurfaces, streamlines, and stream tubes. This chapter first presents the common visualization means and then introduce some representative postprocessing tools with demonstrations from literature.

7.1 VISUALIZATION AND DATA ANALYSIS METHODS

Statistical analysis: A common practice in CFD data analysis is to sample simulation results at characteristic points. This practice usually requires specifying a particular location in the computational domain and for a particular period of time. The sampled result is a time history of velocity, pressure, concentration, density, or other parameters at probe locations. In addition to probe points, it is also a common practice to sample along lines.

Vector field: Vector field is a straightforward method to visualize the velocity field. The vector is usually designed to point in the local velocity direction with a length proportional to the velocity magnitude. The vectors can also be colored according to a color map to reflect the velocity magnitude or other scalar quantities. An example is in Figure 7-1.

Streamlines and stream tubes: A streamline is a curve that is instantaneously tangent to the fluid velocity throughout the flow field. It is commonly used to visualize the velocity field because it is intuitive to show the direction and general trend of the stream. Streamlines can be colored according to the magnitude of velocity, the strength of the vorticity, or any other flow variables to be more informative (e.g., Figure 7-1). Streamlines are generated by setting the starting points in the computational domain and shooting following the tangential

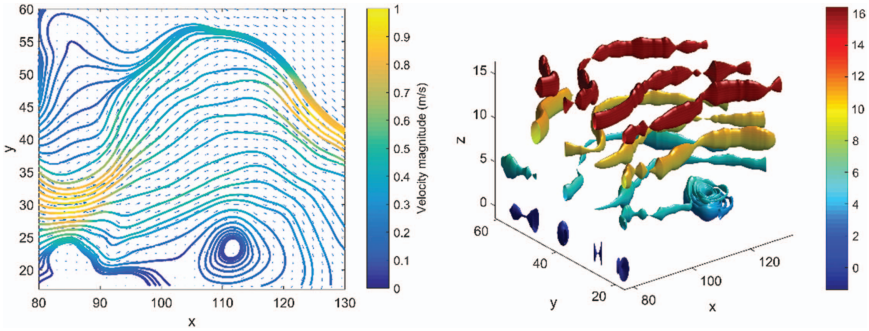

Figure 7-1. Demonstration of streamlines and stream tubes. The color indicates the magnitude of the velocity. Left: streamlines; right: streamtubes. The graphs are generated with MATLAB.

direction of the velocity vectors. If the starting points form a closed curve, the generated stream surface is called a stream tube, which is usually used in 3D simulation to show the change of flow in a cross-sectional area and the flow direction (e.g., Figure 7-1).

Contours and isosurfaces: Lines that connect points that share the same value are called *contours*. Contouring is a common practice used to visualize a scalar field, for example, velocity magnitude, concentration, or salinity. One example is shown in Figure 7-2. The counterpart of contours in 3D domains is called *isosurfaces*, which defines the connected surface with the same value points in space. Contours can be used along with isosurfaces to visualize the data inside the volume of the computational domain.

Visualization of multiphase flow: CFD application in environmental engineering usually involves multiphase flows, for example, free surface, immiscible chemical constituents, and solid particles. Visualization of such multiphase flow is challenging. A common method is to visualize the particles or other dispersed phases as dots or discrete shapes in the computational domain and fluid phase as streamlines or vector fields. Figure 7-3 is an example of particle clouds settling in water. The flow field was visualized using vector field at the cross section intersecting the middle plane of the particle cloud. Another tip to clearly visualize

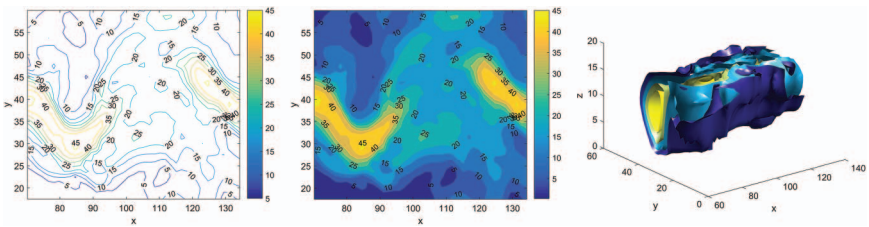

Figure 7-2. Sample plots of contours and isosurfaces. Left, contours; middle, filled contours; and right, isosurfaces.

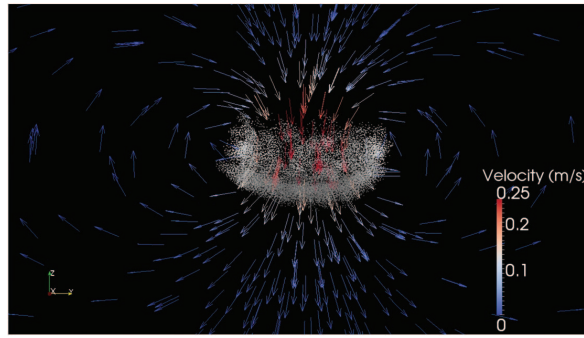

Figure 7-3. Entrainment of ambient fluid into a particle cloud generated by ParaView.
Source: Derived from Wang et al. (2014); reproduced with permission from Elsevier.

3D multiphase flow involves careful rendering with surface material and lighting. More professional 3D animation software, such as Autodesk Maya or Autodesk 3ds Max can be used. A popular open-source alternative is Blender.

Tracer test for residence time distribution: The residence time distribution (RTD) is an indicator of the mixing efficiency of a system, which has been extensively used in environmental and chemical engineering related fields. This concept describes the distribution of the amount of time that a fluid parcel could spend inside the system. In practice, there are generally two ways to determine the RTD, including the so-called pulse experiment and the step experiment.

In the *pulse experiment*, the tracer is injected into the system within a short time to approximate the delta function. The concentration of the tracer at the outlet is monitored, so that the distribution curve can be obtained by

$$E(t) = \frac{C(t)}{\int_0^\infty C(t)dt} \tag{7-1}$$

Note that the exit age distribution $E(t)$ has a unit of 1/time. In the *step experiment*, the concentration of the injection changes abruptly from 0 to C_0. The outlet concentration can be recorded as a function of

$$F(t) = \frac{C(t)}{C_0} \tag{7-2}$$

Then, the exit age distribution can be determined by

$$E(t) = \frac{dF(t)}{dt} \tag{7-3}$$

Ideally, in a plug flow reactor, the function $E(t)$ is a delta function; in a complete mixing system, $E(t)$ follows the relationship

$$E(t) = \frac{1}{\tau} e^{-t/\tau} \tag{7-4}$$

which is an exponentially decaying process. In reality, the rapid and complete mixing system is difficult to achieve, so the determined $E(t)$ deviates from this relationship of exponential decay.

7.2 POSTPROCESSING TOOLS

There are numerous CFD postprocessing tools, including commercial and open-source software. The widely used open-source postprocessing tools include ParaView and VisIt, and commercial postprocessing software includes Ansys CFD-Post, Tecplot 360, and Ensight. Using the postprocessing software that comes with the CFD software is usually sufficient and more convenient. The content that follows aims at briefly introducing some representative postprocessing tools.

7.2.1 ParaView

ParaView is a state-of-the-art postprocessor designed to be able to handle very large data sets. It is an open-source software dedicated to scientific visualization,

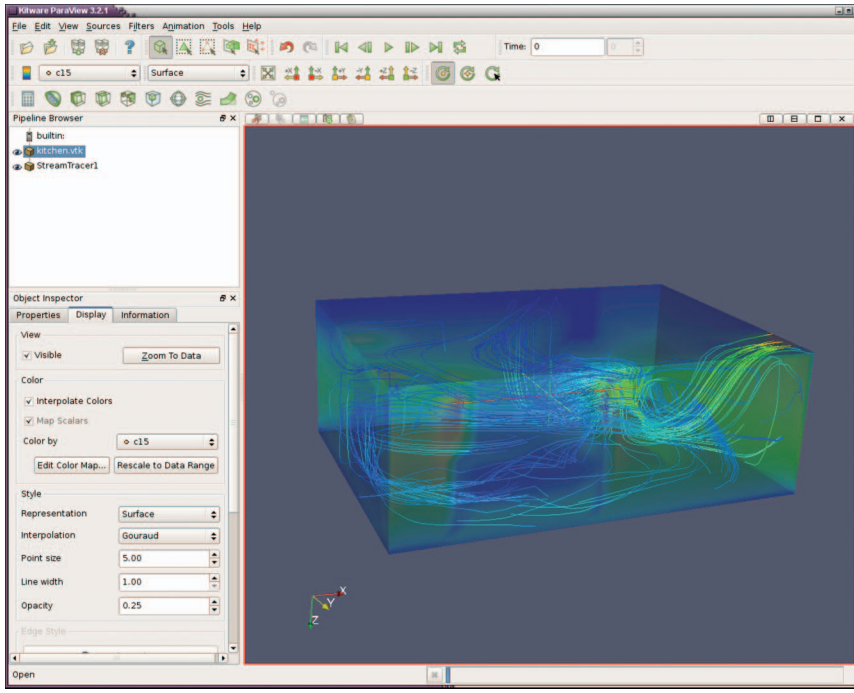

Figure 7-4. User interface of ParaView (http://www.exadios.com/products/paraview/paraview.png).

with a wide range of compatible data formats. Open-source CFD codes, such as OpenFOAM, heavily rely on it to perform postprocessing, and a customized plug-in was developed for this purpose. Figure 7-4 shows the user interface with ParaView.

7.2.2 Ansys CFD-Post

CFD-Post is a flexible, state-of-the-art postprocessor. It is designed to enable easy visualization and quantitative analysis of CFD simulation results. It is distributed with the Ansys CFD package, so it is customized to support Ansys CFD.

7.2.3 Tecplot 360

Tecplot 360 is a visual data analysis tool that integrates *XY*, 2D, and 3D plotting. It is a dedicated CFD visualization tool and optimized for memory use and computing efficiency. Figure 7-5 is a sample postprocessing result of Tecplot 360.

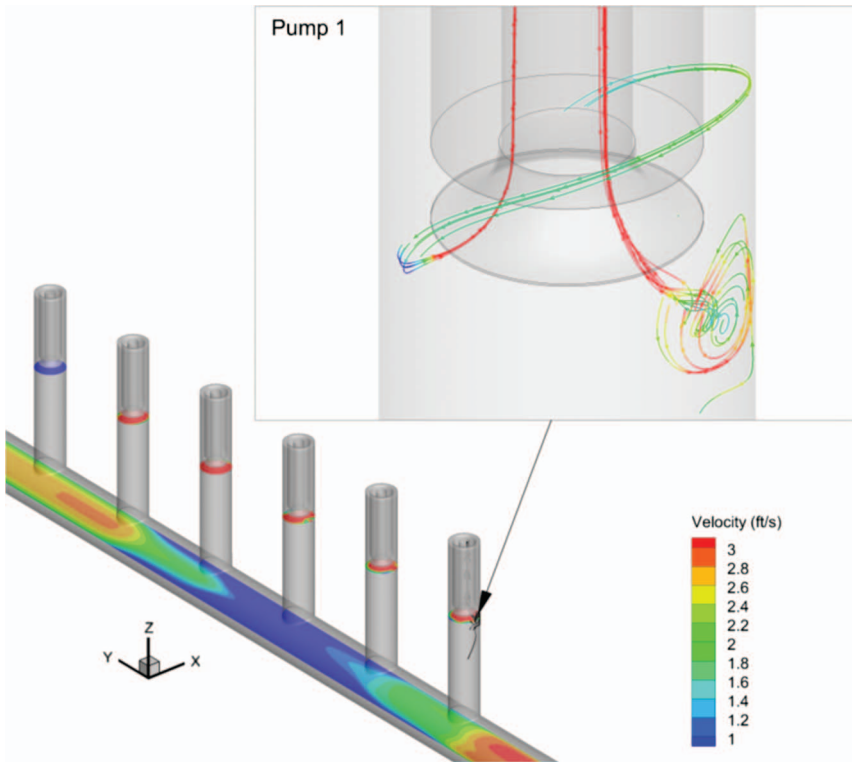

Figure 7-5. A sample postprocessing result of Tecplot. The figure shown is a typical pump intake system used in a water treatment plant. Water flows in from both ends of the bottom pipe. A vortex, which may damage pumping efficiency, is found near the intake mouth of pump 1.

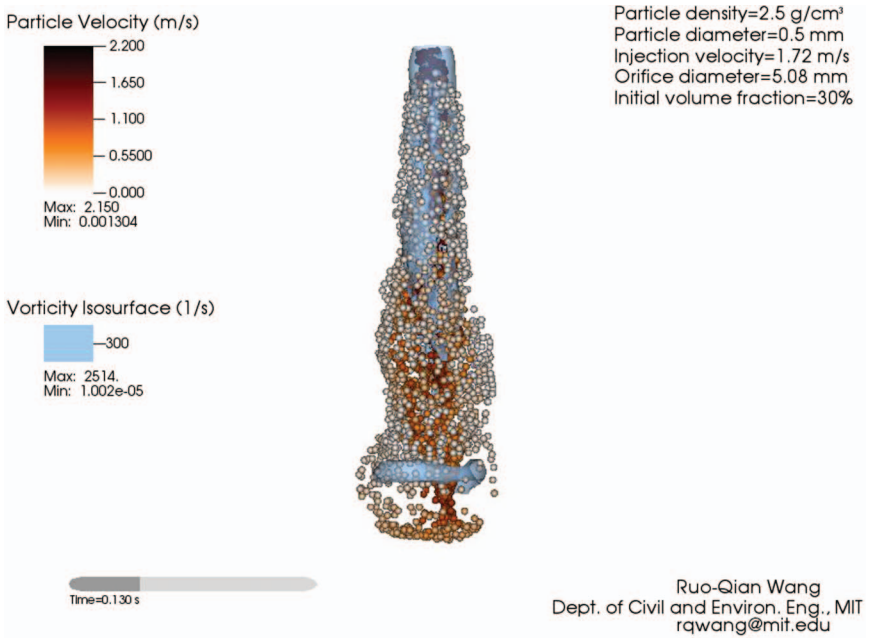

Figure 7-6. A developing particle-laden jet. The visualization is generated using VisIt.
Source: Wang et al. 2013.

7.2.4 Other Tools

There are other tools, for example, EnSight, FieldView, and VisIt. Different softwares have various features and specialties. Figure 7-6 is a visualization result of a particle-laden jet generated by VisIt software.

CFD-online.com has a useful list of postprocessing codes, which can be found at https://www.cfd-online.com/Wiki/Codes. Readers are encouraged to explore them.

It is also worth noting that general programming languages become popular among the advanced postprocessing community to complement the general use of postprocessing tools because of their high flexibility to extract data and ability to handle large data sets. Python, MATLAB, and Java are outstanding examples, among others.

References

Wang, R. Q., A. W. K. Law, and E. E. Adams. 2013. "Large eddy simulation of starting and developed particle-laden jets." In *Proc., 8th Int. Conf. on Multiphase Flow*, Japan Society of Multiphase Flow: Osaka, Japan.

Wang, R. Q., A. W. K. Law, and E. E. Adams. 2014. "Large-eddy simulation (LES) of settling particle cloud dynamics." *Int. J. Multiphase Flow* **67** (12): 65–75.

CHAPTER 8
Verification and Validation

Subbu-Srikanth Pathapati
René A. Camacho

The previous chapters have discussed the methodology of setting up, running, and postprocessing a computational fluid dynamics (CFD) model. This chapter focuses on the all-important issue of how to determine if a CFD model is a valid representation of reality.

8.1 MOTIVATION

Flows in water, wastewater, and stormwater treatment range from natural flows to engineered flows. In these types of flow, we see pressurized pipe flows, gravity-driven flows, and open-channel flows. Flows range from laminar (which are atypical; they mostly occur in filtration or groundwater flow) to fully turbulent. Further complexity ensues with the addition of one or more phases to the model, for instance, modeling gas addition for aeration, particle simulation for sedimentation, or chlorine addition for disinfection. In recent years, we have seen the addition of complex species transport, reaction kinetics, mass transfer, and radiation modeling as well. This being the case, it is all the more important that the process of CFD modeling is undertaken with great care.

Modeling errors can have varied consequences, some of which are as follows:

- **Poor and misleading representation of reality**—where the level of inaccuracy of the results exceeds what is acceptable for the application;
- **Inconsistent results**—where there are drastic differences in the results under the same operating conditions from two different users;
- **Inaccurate results**—which come from using unrealistic physics;
- **Overdesign**—which comes from taking safety factors to an economic breaking point; and
- **Failed design**—resulting from liability to utilities, consultants, original equipment manufacturers, and, most importantly, public health and safety.

8.2 CRITERIA FOR A DEFENSIBLE CFD MODEL

Figure 8-1 and Table 8-1 show the generally accepted criteria for a defensible CFD model (Versteeg and Malalasekara 2007). Each component is described in the following sections.

8.2.1 Consistency

A model is said to be consistent when the solution of a discretized equation approaches the solution of the exact equation as the grid spacing and/or time step tends to zero. In addition, truncation error should also tend to zero as grid spacing and/or time step is infinitesimally small. Although this is a theoretical concept, there are methods to realize this in practice, namely grid independence and time-step independence. A solution is said to be grid independent when there is no significant change in results with progressively finer grids, and a solution is said to be time-step independent when there is no significant change in results with smaller time steps. Figure 8-2 is an example of grid independence in practice (Zhang et al. 2013). The authors demonstrate the variability of cumulative residence time distribution predictions with grid size.

8.2.2 Stability

A stable solution does not amplify errors that appear in the numerical solution process. Stability in steady-state, iterative methods is achieved when the solution does not diverge. Stability in temporal methods is achieved when the model yields a bounded solution. Achieving a stable solution is largely dependent on the particular type of problem and the experience of the user. However, the following best practices may be implemented:

- Choose the right time step: Experiment with the time step depending on the timescale of the process being modeled. In classical CFD, in particular, for

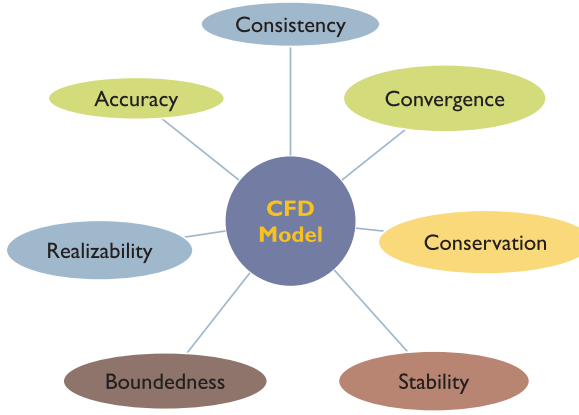

Figure 8-1. Characteristics of a defensible CFD model.

Table 8-1. Characteristics of a Defensible CFD Model

Parameter	*Definition*	*Getting There*
Consistency	Discretized equation approaches the exact equation as grid spacing approaches 0 Truncation error approaches 0 as grid spacing approaches 0	Higher order solution schemes Grid/mesh convergence
Convergence	Numerical solution of transport equations approaches the solution of the exact equation as grid spacing approaches 0	Consistency and stability Iterative convergence
Conservation	In numerical method, all sources and sinks need to be consistent with the net flux through the boundaries of the control volume	Conservation laws are applied to equations of flux as well as the numerical solution method
Stability	Numerical solution method does not amplify errors that appear in the numerical solution process	Iterative methods—when solution does not diverge Temporal methods—when a bounded solution is produced
Boundedness	Numerical solutions should lie within proper bounds Physical nonnegative quantities such as density must be positive values Other quantities such as phase fractions must be between 0% and 100%	Higher order solution schemes Locally refined meshing
Realizability	When the model produces guaranteed physically realistic solutions	Appropriate choice of models Validation with experimental data

compressible flows, a Courant-Friedrichs-Levy (CFL) number less than or equal to one (Ferziger and Peric 2002) is used to choose the appropriate initial time step. For incompressible flows, one practical rule of thumb is to set a time step that is the ratio of the characteristic length to the characteristic velocity in the computational domain. The time step can then be adjusted to accelerate convergence.

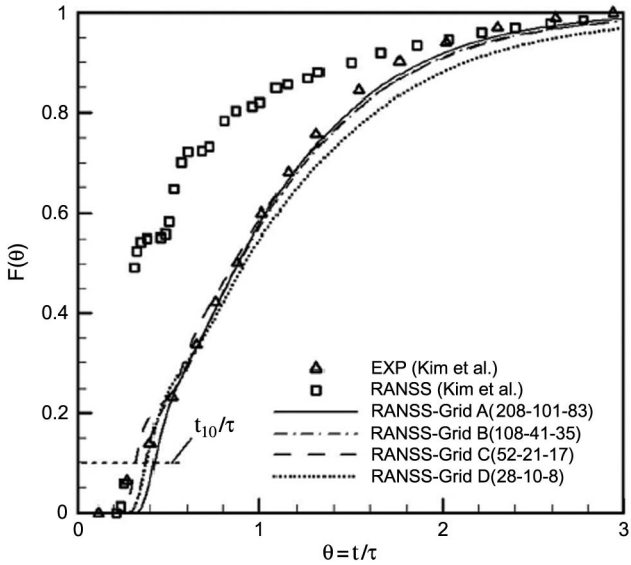

Figure 8-2. Cumulative residence time distribution as a function of grid size. Grid A is made of 1.45 million cells, whereas Grid D is made of 1,864 cells. Grids B and C have cell counts that lie between those of A and D. The model is grid independent using Grid B.

- Use underrelaxation factors (URFs) in the CFD code are used to restrain the amount by which a variable may change from one iteration to the next. Commercial CFD solvers come with default URFs that the modeler can adjust to improve and sustain stability. A typical approach would be to start the solution with lower values of URFs and to increase them closer to default values once residuals show stability and convergence.
- Solve for the flow field first before adding complexity to the model, such as species transport or mass transfer modeling.
- Analyze the sensitivity of the model to boundary conditions or grid size.

8.2.3 Conservation

Conservation of mass, momentum, and energy are at the core of any CFD analysis. Most common CFD codes have in-built options for solving the continuity and momentum equations. The appropriate solution method should be chosen for each specific case study.

Typical solution schemes for the solution of the momentum equations include, for example, first-order and second-order upwinding schemes, and Quadratic Upstream Interpolation for Convective Kinematics QUICK schemes (Tu et al. 2007). Typical mass residual levels for simple steady-state flows are in the range of 1×10^{-3}, whereas multiphase and reacting flows may require more stringent residuals. The same applies to momentum, energy, and other transport

equations. The volume fraction of a secondary, typically gas, phase is of particular interest to water and wastewater treatment CFD modeling. Care must be taken to ensure that the residuals for the volume fraction equation are set to an appropriate level. The following sections provide guidance on simple steps that can be taken to ensure that the CFD model is representative of reality by checking for mass conservation and energy and momentum conservation.

8.2.3.1 Mass Conservation

Tests to confirm mass conservation are generally simple to implement. In models with closed conduits, or models where the direction of the flow is predominantly in one direction, tests of mass conservation can be conducted by setting up flux-measuring devices at the inlet and outlet boundaries of the model, as well as in intermediate locations. The fluxes reported at each location can be plotted and compared to determine if there are substantial differences in flux, which may indicate inexplicable gains or losses of mass.

Figure 8-3 presents an example of a dam and spillway CFD model. In this example, mass conservation can be evaluated by tracking the volumetric fluxes simulated near the upstream and downstream boundaries of the model, as well as in an intermediate location, such as at the forebay. If the differences between the volumetric fluxes throughout the model oscillate within an acceptable range, for example ±2.5%, then mass conservation is satisfied. If the differences exceed the tolerance for mass conservation error, then the modeler needs to investigate the causes of such errors and implement corrective actions to improve the model performance. General causes of mass conservation errors are grid errors and errors in the definition of boundary conditions.

In the design of storage and mixing structures such as ponds, tanks, and reservoirs, an additional strategy to evaluate mass conservation under steady-state conditions consists of tracking the water surface elevations over the simulation period and then simulating the flushing of a conservative tracer, initially well mixed, within the tank or reservoir. If mass conservation is satisfied by the model,

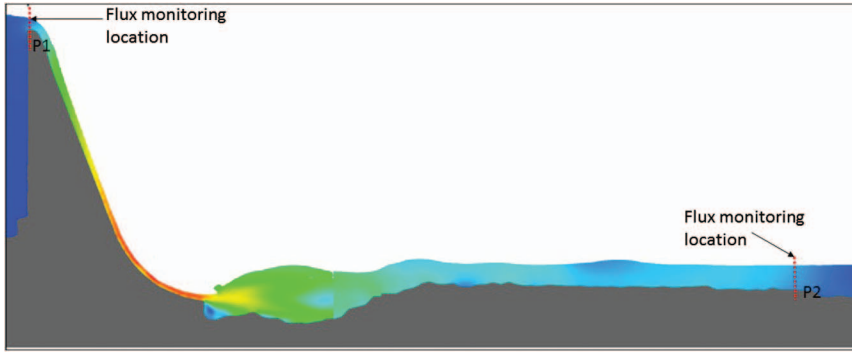

Figure 8-3. Basic checks of performance for a CFD model of a dam and spillway. Flow rates are calculated at an upstream (P1) and downstream (P2) location to check mass conservation.

the tracer must eventually be flushed out of the system. To evaluate the evolution of the tracer in the system, the mass of tracer $M(t)$ that remains in the simulated region at a certain time t can be computed numerically based on the tracer concentration $C(x,t)$ by means of

$$M(t) = \int_V C(x,t)dV \tag{8-1}$$

And this information can in turn be used to evaluate the retention time simulated by the CFD model by means of

$$T_{R,\text{model}} = \int_0^\infty \frac{M(t)}{M_0} \tag{8-2}$$

where M_0 is the initial mass of tracer in the reservoir and the fraction $r(t) = M(t)/M_0$ is a remnant function (Takeoka 1984) that physically represents the fraction of initial mass of dye with residence time greater than $T_{R,\text{model}}$.

8.2.3.2 Energy and Momentum Conservation

Tests of energy conservation can also be performed in a CFD model to ensure that variables such as velocity and pressure are realistic for the system under analysis. One of the simplest checks of energy conservation consists of applying Bernoulli's equation between two points in the flux domain. Bernoulli's equation applied between two points in the direction of the flow indicates that the total amount of energy at each point must be the same, or

$$\frac{P_1}{\gamma} + \frac{1}{2g}V_1^2 + Z_1 = h_f + \frac{P_2}{\gamma} + \frac{1}{2g}V_2^2 + Z_2 \tag{8-3}$$

where
P_1 and P_2 = Pressures at points 1 and 2,
V_1 and V_2 = Flow velocities,
Z_1 and Z_2 = Vertical positions of the fluid at points 1 and 2 in reference to a given datum,
γ = Specific weight of water,
g = Gravity acceleration, and
h_f = Losses of energy caused by friction and accessories.

For the CFD model shown in Figure 8-3, an energy balance can be performed between a point located at the water surface of the forebay area (P1), and another point located close to the apron or base of the dam (P2, where $Z_2 = 0$) to help determine the expected velocities at the base of the dam. If the base of the dam is considered to be the zero datum, the energy balance neglecting energy losses is reduced to

$$V_2 = \sqrt{2gZ_1} \tag{8-4}$$

The theoretical velocities predicted by Equation (8-4) can be compared against the velocities simulated by the model to ensure that the simulation results are within the expected orders of magnitude and range of values.

8.2.3.3 Conservation Monitoring Tools

Monitoring tools available in most commercially available CFD programs, such as flux measurement devices and probes, can be used to support the evaluation of mass, momentum, and energy conservation. An explanation of these tools is presented here:

- **Flux measuring devices:** These are typically 2D planes or porous baffles that can be set up at different locations of a model domain to monitor volumetric fluxes, heat fluxes, and scalar fluxes.
- **Probes:** Probes are single grid cell monitors used to track during a model simulation specific variables such as velocities, pressures, temperatures, and scalar concentrations. Probes can be placed at any grid cell location within the model domain. The information provided by a probe consists of a time series showing the evolution of a particular variable during a test at the probe location.

While monitoring residuals for mass, momentum, and energy convergence, the user can also monitor variation of velocity magnitude, pressure, and volume fractions of primary and secondary phases, among many other variables. This work can be done via continuous plots of the variables of interest as a function of iteration and/or time step. Various options are typically available for reporting real-time information, including and not limited to area-weighted average, mass-weighted average, and volume integrals.

8.2.4 Boundedness and Realizability

Numerical solutions should lie within proper bounds. For instance, though the model shows overall mass convergence, there might be locations in the computational domain with nonphysical values of variables. A thorough check should be performed during postprocessing in order to ensure that all variables are within realistic physical bounds. Typical best practices to meet this requirement include locally refined meshing where large gradients are expected and using higher order discretization schemes.

A through validation protocol is required to ensure that a CFD model is realizable and translates from design to real-time implementation. Please refer to the Sections 8.3 and 8.4 on validation and calibration.

8.2.5 Accuracy

No model is a 100% accurate representation of reality. A numerical model is said to be close to accurate when the errors inherent in producing an approximate numerical solution are reduced and controlled. This list provides a broad description of the types of errors encountered in a CFD analysis (Kaiser 2005).

- Numerical Errors
  - **Modeling errors:** The difference between the actual flow and the exact solution to the mathematical model. These errors are not known a priori.
  - **Discretization errors:** The difference between the exact solution of the conservation equations and the exact solution of the algebraic (discretized) system of equations. Truncation errors are part of this.
  - **Convergence errors:** The difference between the iterative solutions and the exact solutions of the discretized equations.
- User Errors
  - Garbage in, garbage out (GIGO).
  - Inability to reproduce results across different users.
- Software Errors
  - Poor code, bugs in code.
  - Unsuitable software for particular application.
- Validation Errors
  - Insufficient or poorly sampled experimental data.
- Representation Errors
  - Is the model oversimplified, for example, using a 2D approach to solve a 3D problem?

A simple 1D calculation, such as checking the velocity magnitude at inlets and outlets, can be performed as a basic check of accuracy. The user can compare hand calculations with an area-weighted average from CFD postprocessing.

8.3 VERIFICATION VERSUS VALIDATION

Verification in CFD is defined as "The process of determining that a model implementation accurately represents the developer's conceptual description of the model and the solution to the model," or *solving the equations right* (AIAA 1998). Verification is essentially minimizing numerical errors.

Validation in CFD is defined as "The process of determining the degree to which a model is an accurate representation of the real world from the perspective of the intended uses of the model," or *solving the right equations* (AIAA 1998). Validation is the comparison of model results with experimental data.

Table 8-2 summarizes the steps taken during verification versus validation.

The user should be cognizant of the uncertainties associated with experimental data caused by factors such as poorly calibrated or uncalibrated instrumentation, poor sampling techniques, and measurement errors. Choosing a measurable index to validate CFD results is of the utmost importance. For instance, in disinfection of water, there is a desired residual component that is

Table 8-2. Verification versus Validation

Steps	*Verification*	*Validation*
1	Examine the computer programming of the code (choose the right code for your application)	Examine iterative convergence
2	Examine iterative convergence	Examine consistency
3	Examine consistency	Examine spatial (grid) convergence
4	Examine spatial (grid) convergence	Examine temporal convergence
5	Examine temporal convergence	Compare CFD results to experimental data
6	Compare CFD results to highly accurate solutions	Examine model uncertainties

measured downstream of the ozone contactor. If sampling is not representative of the entire cross section of flow, CFD results do not correlate with measured data. It is recommended to us error bars with experimental data while comparing with CFD results.

8.4 CALIBRATION OF MODELS

Core fluid mechanical equations do not require calibration. In addition, widely used and robust turbulence models do not require calibration for coefficients for most applications. That being said, CFD models can be calibrated, depending on the application. For instance, in geophysical applications of CFD models, the tests of accuracy are conducted during the phases of calibration and confirmation (Gupta et al. 2006, McCutcheon et al. 1990). During calibration, a model representing the existing conditions of the system is executed, and the simulations are compared against empirical observations of important transport variables, such as velocities, pressures, water elevations, and temperatures. The calibration target is usually the roughness of the solid boundaries. Meanwhile, other parameters, such as those associated with the turbulence closure model, are not subject to calibration.

Calibration examples of CFD models are in general limited but can be found in the literature. Teklemariam et al. (2008) for example, calibrated a CFD model of the Keeyask Generating Station on the Nelson River, in Manitoba, Canada, based on comparisons between model simulations and stage-discharge rating curves available at different locations of the simulated region. The process of calibration is

also known as *model skill assessment,* and it allows a modeler to identify issues in input data sets and assumptions and to improve the model by adjusting different model subcomponents and parameters (Gupta et al. 2006; Hsu et al. 1999, Jolliff et al. 2009, Li et al. 2005, Versteeg and Malalasekera 2007, Zhang et al. 2010).

Whereas model calibration is a critical modeling practice used to ensure model accuracy and to report the level of errors expected from the model simulations, empirical data to corroborate CFD model results are generally difficult to obtain or are unavailable for larger scale applications. In the absence of empirical data to constrain model simulations, the modeler must implement alternative tests of model performance to ensure that at a minimum, the model simulations are a realistic representation of the conditions expected in the field. Some useful general tests of model accuracy include checks of mass, momentum, and energy conservation throughout the modeled system. These tests are generally easy to implement in any CFD model and can be compared to the results from manual applications of basic hydrodynamic principles; these principles are outlined in the previous section on convergence (8.2.3).

8.5 SUMMARY OF BEST PRACTICES

- Check for grid independence to ensure consistency in solutions.
- Check for time step dependence for transient simulations.
- Perform mass and energy balance checks.
- Perform sensitivity analyses to boundary conditions and grid size.
- Iterative convergence should be set to appropriate residual level.
- Check for anomalous quantities in the computational domain.
- Search literature for appropriate models for turbulence, multiphase flow, and species transport for a given case.
- Test the robustness of the CFD code with simple benchmark cases.

References

AIAA (American Institute of Aeronautics and Astronautics). 1998. *AIAA guide for the verification and validation of computational fluid dynamics simuations*. AIAA G-077-1998. Reston, VA: AIAA.

Ferziger, J. J, and M. Peric. 2002. *Computational methods for fluid dynamics*. 3rd ed. Berlin: Springer-Verlag.

Gupta, H. V., K. J. Beven, and T. Wagener. 2006. *Model calibration and uncertainty estimation, encyclopedia of hydrological sciences*. Hoboken, NJ: Wiley.

Hsu, M., A. Kuo, J. Kuo, and W. Liu. 1999. "Procedure to calibrate and verify numerical models of estuarine hydrodynamics." *J. Hydraul. Eng.* **125** (2): 166–182.

Jolliff, J. K., J. C. Kindle, I. Shulman, B. Penta, M. A. M. Friedrichs, R. Helber, and R. A. Arnone. 2009. "Summary diagrams for coupled hydrodynamic-ecosystem model skill assessment." *J. Mar. Syst.* **76** (1–2): 64–82.

Kaiser, J. 2005. *CFD best practice guidelines*. Canonsburg, PA: ANSYS.

Li, M., L. Zhong, and W. C. Boicourt. 2005. "Simulations of Chesapeake Bay estuary: Sensitivity to turbulence mixing parameterizations and comparison with observations." *J. Geophys. Res.* **110** (C12): C12004.

McCutcheon, S. C., Z. Donwei, and S. Bird. 1990. *Model calibration, validation and use: Manual for performing waste load allocations*. USEPA-823-R-92-003. Washington, DC: USEPA.

Takeoka, H. 1984. "Fundamental concepts of exchange and transport time scales in a coastal sea." *Cont. Shelf Res.* **3** (3): 311–326.

Teklemariam, E., B. Shumilak, D. Murray, and G. K. Holder. 2008. "Combining computational and physical modeling to design the Keeyask Station." *Hydro. Rev.* **27** (4): 67–72.

Tu, J., G. Yeoh, and C. Liu. 2007. *Computational fluid dynamics: A practical approach*. Oxford, UK: Butterworth-Heinemann.

Versteeg, H. K., and W. Malalasekera. 2007. *An introduction to computational fluid dynamics: The finite volume method*. London: Pearson Education.

Zhang, A., K. W. Hess, and F. Aikman. 2010. "User-based skill assessment techniques for operational hydrodynamic forecast systems." *J. Oper. Oceanogr.* **3** (2): 11–24.

Zhang, J., A. E. Tejada-Martínez, and Q. Zhang. 2013. "Reynolds-averaged Navier-Stokes simulation of the flow and tracer transport in a multichambered ozone contactor." *J. Environ. Eng.* **139** (3): 450–454.

This page intentionally left blank

Part 3

Water Treatment Technologies and CFD Application Case Studies

This page intentionally left blank

CHAPTER 9

Aeration

Tien Yee
Yovanni A. Cataño-Lopera
Jie Zhang

9.1 BACKGROUND

Jet aerators are commonly used in wastewater treatment plants to help introduce air into wastewater. The efficiency of jet aerators to transfer oxygen to wastewater in a basin depends on two main factors, the aeration capabilities of the device itself, which determines the overall volumetric mass transfer coefficient K_La values, and the surrounding hydrodynamics (Fonade et al. 2001). Currently, the operational design of a basin with jet aerators is empirical (Morchain et al. 2000). Although the empirical equations provide a starting point for a wastewater treatment plant design, the design may not be efficient. Through the use of a CFD model, the oxygen transfer efficiency of jet aerators was evaluated, along with the influence of the transverse flow. This case study was done to reproduce part of the Morchain et al. (2000) work and to provide readers a glimpse of the capabilities of CFD in aeration studies.

9.2 OBJECTIVES

1. Hydrodynamic modeling of the flow field in an aerated lagoon with transverse flow (Figure 9-1).
2. Comparison of oxygen mass transfer to ideal reactor models with transverse flow.

9.3 RESULTS AND DISCUSSION

9.3.1 Hydrodynamics of Jet with Cross-Flow

Simulations were carried out for various cross-flow conditions α, where α represents the ratio between the jet velocity and the cross-flow velocity.

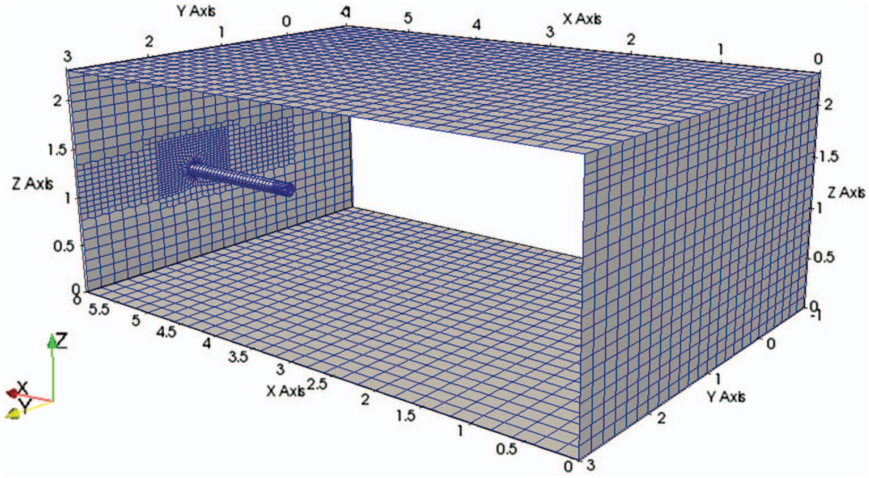

Figure 9-1. Geometry of simulation domain showing part of a lagoon and the jet aerator.

Information regarding the numerical model, solver, flow and geometry are listed in Table 9-1.

As mentioned in Morchain et al. (2000), the jet flow path is deflected as shown in Figure 9-2 and is sensitive and dependent upon the cross-flow. Also, the transverse flow of the jet can be characterized by a kidney-shaped curve of the jet and is shown in Figure 9-3. Furthermore, the jet core was also observed to be accompanied by a pair of counterrotating vortexes adjacent to the jet. Intense mixing occurs behind the inner boundary of the jet because of these vortexes. These hydrodynamic characteristics show the influence of cross-flow within an aeration lagoon, which affects the modeling of air and oxygen transfer.

9.3.2 Mean Mass Fraction and Oxygen Transfer

In this study, the oxygen mass fraction was modeled using the scalar transport equation, with the source term described by the equation

$$q = \rho K_L a (C^* - C) \tag{9-1}$$

where

q is analogous to the flux density (kg O_2 $m^{-3}h^{-1}$),

ρ = Density of the fluid, C^* (9.0×10^{-6} kg O_2 kg^{-1}) and C is the mass fraction of oxygen in saturated water at 20°C and modeled oxygen mass fraction, respectively, and

$K_L a$ = Overall volumetric transfer coefficient in units of h^{-1}.

The variable $K_L a$ was treated as a constant for each simulation case. The mass transfer of oxygen is related to the mass fraction of oxygen through fundamental mass conservation ρQC. For the detailed determination of oxygen transfer, readers

Table 9-1. Information Related to the CFD Simulation

Flow conditions	Items		Reference
	System	Hypothetical semi-infinite rectangular domain surrounding jet aerator	
	Geometry	See Figure 9-1	Morchain et al. (2000)
	Dimensions	6 m × 4 m × 2 m	
	Aerator flow rate	50 m^3/h	
	Transverse current flow rate	3,000 m^3/h	
Model information	Simulation	Method or Governing Equation	
	Type	RANSS finite volume code	
	Flow	N-S equation	Section "CFD Model" – See Chapter 4 for model description
	Turbulent model	Standard *k*-omega	
	Oxygen mass fraction	Scalar transport equation for passive scalar	
Software used	Type of software	OpenFOAM	Free/open source
	Meshing tool	snappyHexMesh	Free/open source
	Solver	interFoam	Free/open source
	Postprocessing tool	ParaView	Free/open source

(Continued)

Table 9-1. Information Related to the CFD Simulation (Continued)

Computational information	Items	Remarks
	Computational grid	57,612 unstructured mesh grid Min volume = 1.165×10^{-7} m^3. Max volume = 3.72×10^{-3} m^3
	Computing device equivalent	CPU: Xeon E7-4820 Speed: 2.0 GHz CPUs: 4 Cores: 32 Memory: 256 GB
	Computing time	25 h, 11 min

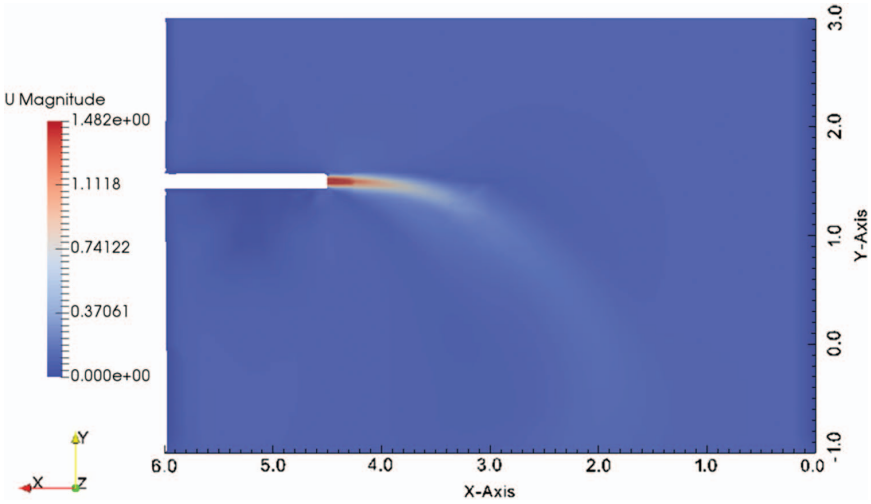

Figure 9-2. Velocity magnitude plot along horizontal plane containing jet axis for $\alpha = 15$.

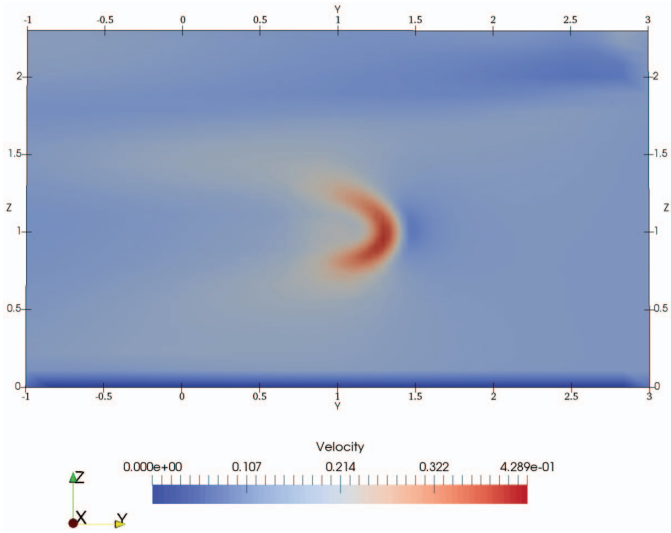

Figure 9-3. Velocity magnitude plot along vertical plane at $X = 15 \times$ *diameter,* $\alpha = 10$.

are referred to Morchain et al. (2000). A typical plot of the mean mass fraction of oxygen perpendicular to the jet axis is shown in Figure 9-4 for the case of $\alpha = 15$.

The CFD model was used to simulate the plug flow reactor (PFR), and comparison was made for oxygen transfer to that of an ideal behavior closed reactor model, the perfectly mixed reactor (PMR) (Figure 9-5). The finding shows that for a PFR, the amount of oxygen transfer depends on the transverse flow rate

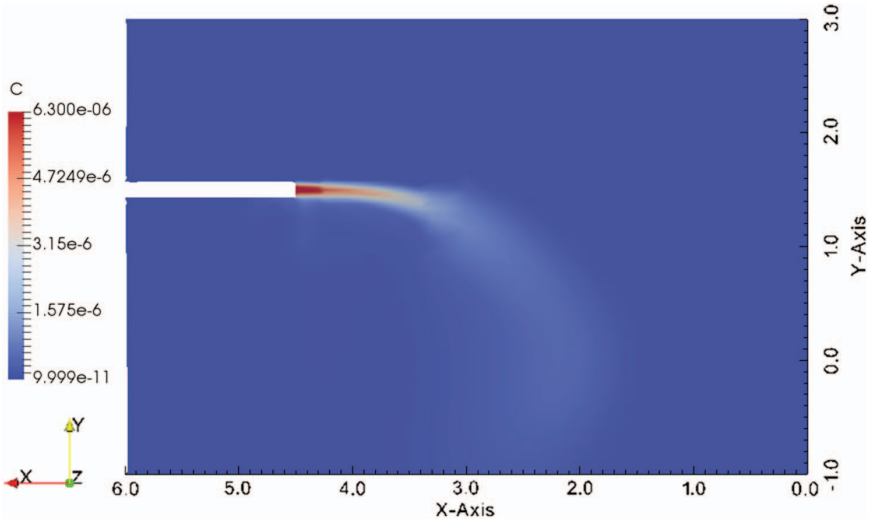

Figure 9-4. Mean mass fraction of oxygen plot perpendicular to the jet axis for $\alpha = 15$.

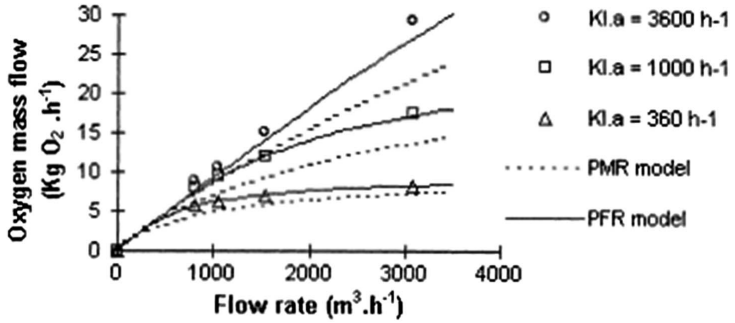

Figure 9-5. Rate of oxygen transfer (the amount of oxygen transfer in terms of mass of O_2 *per unit time) for different transverse liquid flow rates and different* $K_L a$ *values.*

Source: Adapted from Morchain et al., with permission.

of liquid being aerated. When the transverse flow rate is low, modifying the overall volumetric oxygen transfer coefficient $K_L a$ has little effect on the amount of oxygen transfer that is generated from the transverse flow flushing the aerated zone. At high transverse flow rates, a tenfold increase in the $K_L a$ value only doubles the oxygen transfer capacity. This finding by Morcain et al. (2000) shows that the momentum in the fluid phase is not significantly affected by the presence of air bubbles and therefore, the use of a single-phase model is deemed appropriate.

References

Fonade, C., N. Doubrovine, C. Maranges, and J. Morchain. 2001. "Influence of a transverse flowrate on the oxygen transfer performance in heterogeneous aeration: Case of hydro-ejectors." *Water Res.* **35** (14): 3429–3435.

Morchain, J., C. Maranges, and C. Fonade. 2000. "CFD modeling of a two-phase jet aerator under influence of a crossflow." *Water Res.* **34** (13): 3460–3472.

This page intentionally left blank

CHAPTER 10
Sedimentation

Xiaofeng Liu

10.1 BACKGROUND

When wastewater is transported to the treatment plant, it is preliminarily treated to remove large debris and solids (WEF 2009). Then, the wastewater flows through primary treatment tanks, which constitute the first step to remove solids that are not removed by preliminary treatment. Primary treatment is designed to serve as a preliminary step before secondary treatment, which includes biological and chemical processes.

The secondary treatment unit receives influx from the biological unit. Within the sedimentation treatment unit, the solids settle in the tanks. With time, the settled solids thicken, and a blanket of sludge is formed on the bottom. In this chapter, we focus on the primary tanks, where the physical settling process is the dominating action.

Settling tanks are of great importance to the effectiveness of the wastewater treatment process. They constitute a substantial portion of the total constructional and operational cost of a treatment plant. They also occupy a large percentage of space in the footprint of a plant. In general, from the point of view of their geometric shapes, there are three kinds of settling tanks: circular, rectangular, and vertical flow configurations.

10.2 OBJECTIVES

1. Analyze the flow field and sludge concentration distribution.
2. Estimate the settling efficiency of different tank configurations.

The simulation case presented in this section was adapted from Liu and García (2011). The main purpose of the study was to optimize the design of large primary settling tanks for the city of Chicago. The scheme diagram of the settling tanks is shown in Figures 10-1 and 10-2. The detailed information about the CFD

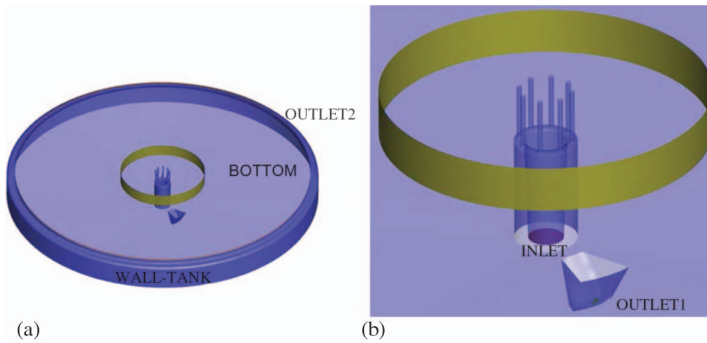

Figure 10-1. 3D view of the settling tank modeled in this study: (a) overall view of the tank, and (b) center area view around the feed well. Note that the boundary names are labeled.
Source: Liu and García (2011).

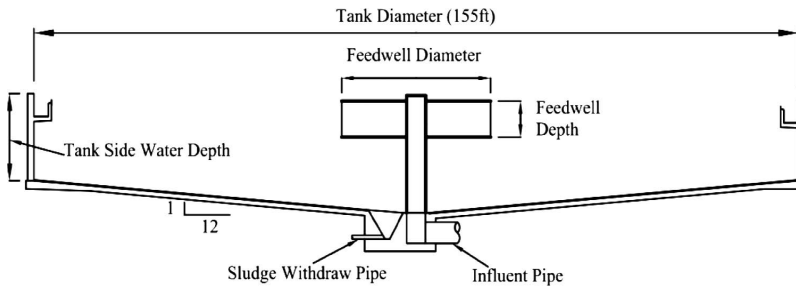

Figure 10-2. Definitions of the design parameters for the primary settling tank.
Source: Liu and García (2011).

simulation is listed in Table 10-1. Among many parameters that affect tank performance, the most influential ones are the tank depth and diameter, which not only affect the hydrodynamics but also the cost and spatial footprint. Because of the limitation of the plant site, the tank diameter had to be fixed to be 155 ft (47.24 m). Thus, the major simulation cases were for the variations of tank depth. Other simulations were also done later for the design of details, such as inlet and outlet structures, feed well diameter and depth, and bottom slope. For demonstration purposes, only one case is shown in this section. The idea is to show the whole workflow of how to use OpenFOAM's driftFluxFoam solver for a typical simulation.

A more elaborate description of the model formulations and simulation steps can be found in the case folder.

Table 10-1. Information Related to the CFD Simulation

Flow conditions	Items		Reference
	System based on	A full-scale primary settling tank designed for the Metropolitan Water Reclamation District of Chicago	
	Geometry	Figures 11.1 and 11.2	Liu and Garcia (2011)
	Dimensions	155-ft diameter and 15 ft deep	
	Flow rate	4.4 million gal./day with an inflow volumetric concentration of 0.0001	
Model information	Simulation	Method or governing equation	Brennan (2001)
	Type	RANS	
	Flow	N-S equation for non-Newtonian fluid	The detailed model description is in the case folder
	Particle concentration	Transport equation for passive scalar with a settling flux	
Software used	Type of software	OpenFOAM	Free and open source
	Meshing tool	Ansys Meshing	Commercial
	Solver	driftFluxFoam	Free and open source
	Postprocessing tool	ParaView	Free software
Computational information	Items	Remarks	
	Computational grid	Unstructured, 553,314 cells	
	Computing device equivalent	8 CPU cores	
	Computing time	~6 h	

10.3 RESULTS AND DISCUSSION

Flow field: The flow field is shown in Figure 10-3. The influent enters the tank from the bottom through the central feed pipe. Then it flows up and spreads laterally in the center well until it hits the baffle and bends downward. The flow then continues along the radius of the tank toward the effluent weir. Gravitational settling of particles occurs as the flow moves through the system. Figure 10-3 also shows the formation of a sludge layer on the bottom of the tank.

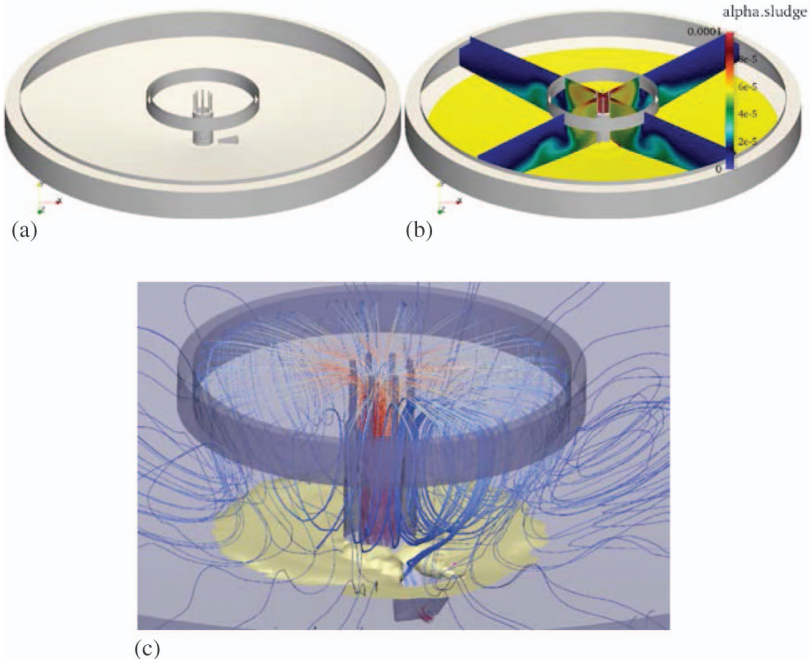

Figure 10-3. Result visualization using ParaView: (a) background, (b) contour and isosurface plot, and (c) streamlines.

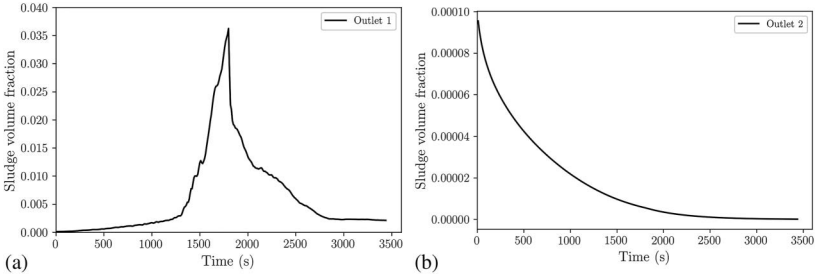

Figure 10-4. Simulation results: (a) outlet 1 concentration history, and (b) outlet 2 concentration history.

Concentrations at outlets: The recorded concentration (recorded as volume fraction of sludge) time history at each outlet is plotted and analyzed in Figure 10-4. The sludge withdraw pump operates on a schedule of a half-hour on and a half-hour off. For Outlet 1 (sludge withdraw port), the concentration builds up steadily until the pump is turned on and then the concentration of the withdraw decreases. On the other hand, as shown in Figure 10-4(b), for Outlet 2 (effluent of the tank), the concentration shows a steady exponential decline from a uniform initial volumetric concentration (percentage) (0.0001) as particles settle out.

References

Brennan, D. 2001. "The numerical simulation of two phase flows in settling tanks." Department of Mechanical Engineering, Ph.D. dissertation, Univ. of London.

Liu, X., and M. H. García. 2011. "Computational fluid dynamics modeling for the design of large primary settling tanks." *J. Hydraul. Eng.* **137**(3): 343–355.

WEF (Water Environment Federation). 2009. *Design of municipal wastewater treatment plants: WEF manual of practice 8, ASCE manuals and reports on engineering practice, no. 76*. 5th ed. New York: McGraw-Hill Education.

APPENDIX: MODELING INSTRUCTIONS

The detailed steps to create and run the case in OpenFOAM are provided here. It is assumed that the reader is somewhat familiar with the basic case structure in OpenFOAM, which contains a set of subdirectories and files. The reader is encouraged to consult the OpenFOAM user's guide and ensure that the proper version of OpenFOAM is installed on his or her machine. The OpenFOAM version used to set up and run the model is v4.x.

STEPS

1. Generate mesh using OpenFOAM utility blockMesh or snappyHexMesh or another meshing software; if necessary, import the mesh generated externally into the OpenFOAM program.
2. Run OpenFOAM's "checkMesh" tool to check the validity and quality of the mesh. If problems are reported, fix the mesh.
3. Set boundary and initial conditions in the case's "0" directory (if the initial starting time is 0).
4. Modify the control parameters (e.g., startTime, endTime, timeStep, or writeInterval) in the case's "/system/controlDict" file. The user can also set run time postprocessing (e.g., sampling and monitoring) in this step.
5. Run the case by issuing the solver's command (the name of the solver) in the Linux command window.

This page intentionally left blank

CHAPTER 11
Ozone Disinfection

Jie Zhang

11.1 BACKGROUND

Ozone disinfection is becoming increasingly common in the water treatment industry, in part because of its strong disinfecting properties and in part because it controls taste and odor compounds (Crittenden et al. 2012, Zhang et al. 2014). Globally, more than 3,000 ozone contactors are being used for water disinfection (Wols et al. 2010). A common approach to ozone disinfection is to pass the water through an ozone contactor tank consisting of a series of chambers, as depicted in Figure 11-1. The flow in an ozone contactor is usually characterized by shorting-circuiting and recirculation or dead zones (as shown in Figure 11-1), which reduce hydraulic efficiency. Ozone gas is released into the chambers from the bottom of one or multiple chambers via bubble diffusers. Upon release, the ozone dissolves in the water and begins the disinfection process.

11.2 OBJECTIVES

This case study aims to

- Analyze the flow fields and residence time distribution (RTD) of the system,
- Predict distributions of ozone and concentration of by-products (e.g., bromate), and
- Estimate effluent disinfectant concentration-contact time (CT) value through the CFD modeling of a full-scale ozone contactor operated by the city of Tampa Water Department, Florida (shown in Figure 11-2). More details of the simulation can be found in Table 11-1.

11.3 RESULTS AND DISCUSSION

Flow: Figure 11-3 shows speed contours and streamlines of the flow in the ozone contactor. The flow pattern is characterized by an undulating, high-speed core jet

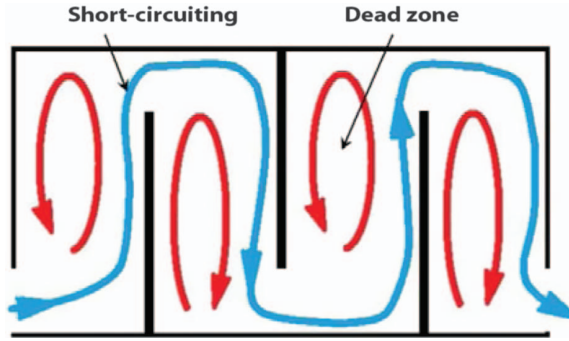

Figure 11-1. Short-circuiting and dead zones in a typical ozone contactor.

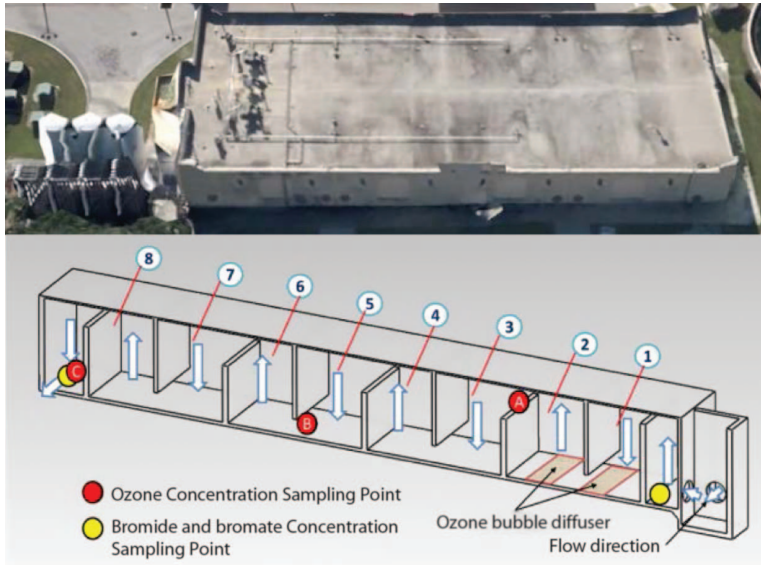

Figure 11-2. Photo and schematics of the David L. Tippin Water Treatment facility, Water Department of the City of Tampa, Florida.
Source: Courtesy of Elsevier; reproduced with permission.

extending from chamber to chamber and a secondary, slower recirculation zone, or dead zone, within each chamber. The core jet facilitates the passage of a portion of water through the whole length of the contactor over much shorter times than the mean residence time, resulting in short-circuiting and thus a reduction in hydraulic (disinfection) efficiency.

Tracer: Figure 11-4 shows the normalized residence time distribution and cumulative residence time distribution of the ozone contactor. The first peak of the RTD is caused solely by short-circuiting. The following peaks result from the combined effect of recirculation (dead) zones and short-circuiting. The baffling

Table 11-1. Information related to the CFD simulation

Flow conditions	Items		Reference
	System based on	A full-scale ozone contactor operated by the city of Tampa's water department	
	Geometry	Figure 11-2	Zhang et al. 2014
	Dimensions	51.7 m × 12.2 m × 7.32 m	
	Flow rate	45–55 million gal./day (2.0–2.4 m^3/s)	
Model information	**Simulation**	**Method or Governing Equation**	**Reference**
	Type	RANS	Section 5.2
	Flow	N-S equation	Chapter 1
	Tracer	Transport equation for passive scalar	Section 2.2
	Chemical reaction	Transport equation for chemical species	Section 2.2
	CT	Transport equation for CT	Section 2.2
	Reaction system	6 species/6 reactions	Zhang et al. 2014
Software used	**Type of software**	**Name of software**	**Availability**
	Meshing tool	Gambit or Gridgen	Commercial
	Solver	OpenFOAM	Free and open source
	Postprocessing tool	ParaView	Free software
Computational information	**Items**	**Remarks**	
	Computational grid	Structured, 881,050 cells	
	Computing device equivalent	(4 CPU cores + 8 G RAM) × 4	
	Computing time	~48 h	

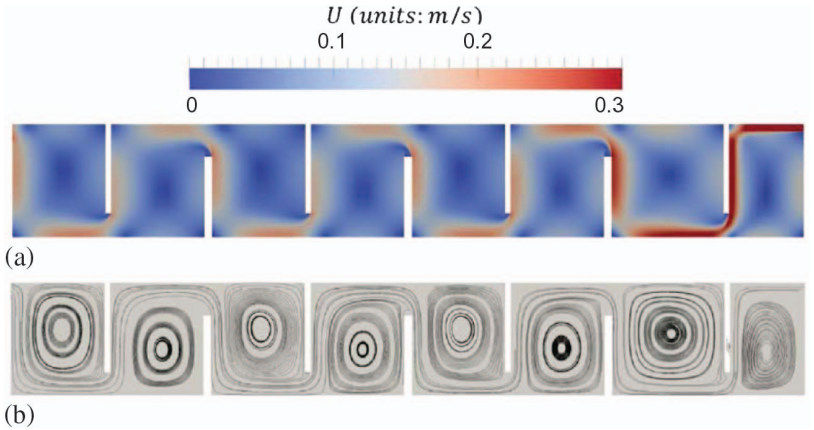

Figure 11-3. (a) Speed contours and (b) streamlines on the streamwise-vertical plane at midspan of the simulated full-scale ozone contactor. Note that the flow direction is from right to left.
Source: Courtesy of Elsevier; reproduced with permission.

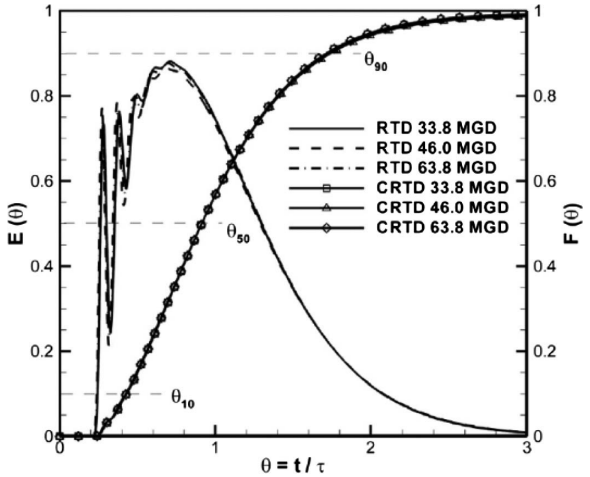

Figure 11-4. Normalized residence time distribution (RTD) and cumulative residence time distribution (CRTD) for different flow rates.
Source: Courtesy of Elsevier; reproduced with permission.

factor, which is a common used index of hydraulics, predicted by the CFD simulation is 0.49. This is close to the physical experimental measurement (0.54).

Ozone: In Figure 11-5, the predicted ozone concentrations are compared with physical experimental data for scenarios (with different operation conditions) at the sample points marked in Figure 11-2. In this figure, it can be observed that all the data points are close to the bisector with an *R*-square or coefficient of

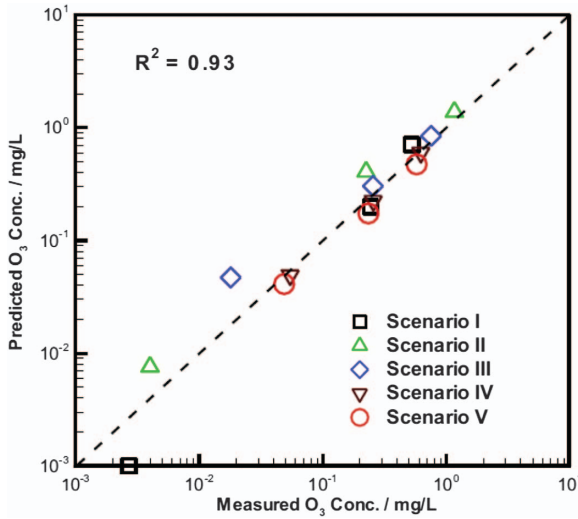

Figure 11-5. Comparison of predicted and measured ozone concentration at the sample points A, B, and C in Figure 11-2.
Source: Courtesy of Elsevier; reproduced with permission.

Table 11-2. Average CT values at contactor outlet

Scenario	*I*	*II*	*III*	*IV*	*V*
CT (mg min/L)	14.04	22.06	13.19	9.56	9.97

determination equal to 0.93. This result indicates that the predictions of ozone concentrations have good agreement with the physical experimental data, serving to validate the chemical reaction simulations conducted as well as the overall computational framework.

CT: As shown in Table 11-2, the CT value is greater than 7.8 min/L in all scenarios, demonstrating that the full-scale ozone contactor evaluated is able to meet disinfection regulations.

References

Crittenden, J. C., R. R. Trussell, D. W. Hand, K. J. Howe, and G. Tchobanoglous. 2012. *MWH's water treatment: Principles and design*. Hoboken, NJ: Wiley.

OpenCFD Ltd. 2010. "OpenFOAM user guide version 1.7.1." Accessed November 24, 2013. https://www.openfoam.com/docs/user/.

Wols, B. A., J. A. M. H. Hofman, W. S. J. Uijttewaal, L. C. Rietveld, and J. C. Van Dijk. 2010. "Evaluation of different disinfection calculation methods using CFD." *Environ. Modell. Software* **25** (4): 573–582.

Zhang, J., A. E. Tejada-Martínez, Q. Zhang, and H. Lei. 2014. "Evaluating hydraulic and disinfection efficiencies of a full-scale ozone contactor using a RANS-based modeling framework." *Water Res.* **52**: 155–167.

APPENDIX: MODELING INSTRUCTIONS

The detailed steps to create and run the case in OpenFOAM are provided below. Before starting the case, it is recommended that the user become familiar with the basic directory structure in OpenFOAM, which contains the minimum set of files required to run an application. The reader is encouraged to read carefully Section 4.1 of OpenFOAM User Guide(OpenCFD Ltd. 2010). Ensure that OpenFOAM is properly installed in your machine. The OpenFOAM version used to set up and run the model is v1.7.

STEPS

1. Generate mesh using OpenFOAM utility blockMesh or snappyHexMesh or another software (e.g., Gambit or Gridgen).
2. Optional: Convert the mesh into OpenFOAM format if it comes from another software.
3. Make the boundary names in the files of initial variables (in folder "0") are consistent with those in the "boundary" file in /constant/polymesh/.
4. Modify the control parameters (endTime, timeStep, and writeInterval) in /system/controlDict.
5. Run the case by using the command (the name of the solver defined in the /system/controlDict) in the Linux command window.

CHAPTER 12

Pumping Intakes

Kevin D. Nielsen
Daniel Morse
Tien Yee
Jie Zhang

12.1 BACKGROUND

Analysis of pump approach flow conditions is an important part of pump station design. The objectives of pump intake design are to mitigate phenomena such as submerged vortices, free-surface vortices, excessive preswirl of flow entering the pump, nonuniform spatial distribution of velocity at the impeller eye, excessive variations in velocity and swirl with time, and entrained air or gas bubbles (Claxton 1998). Undesirable approach flow conditions can lead to poor pump performance in a variety of ways, such as reduced flow and head capacity, increased power requirements, cavitation damage, vibration, and noise. These impacts not only negatively affect the ability to meet fluid flow design criteria, but they can also have significant impacts on operation and maintenance costs.

In the past, pump intake design studies have been mostly carried out using scaled physical model tests. However, development of computational fluid dynamics (CFD) techniques over the past two decades have made it possible for CFD analysis to play an important role in the design and troubleshooting of pump intakes. Specific methodologies for developing physical model tests to evaluate pump intakes are described in the Hydraulic Institute standards for pump intake design. Current CFD model evaluations of pump stations attempt to simulate these same hydraulic tests and acceptance criteria, as discussed in the following section. As CFD becomes more widely used and comparisons to actual pump performance become more available, other hydraulic criteria may become applicable for the evaluation of pump intakes using CFD.

The Hydraulic Institute (HI) provides approach flow design guidelines to help ensure proper pump performance. Adherence to these guidelines can reduce the risk of poor pump performance. However, site constraints can often limit the ability to meet all the approach conditions recommended by the HI standards.

Proper pump performance may still be achieved through wet well modification or through remedial measures. Ensuring that these modifications achieve the desired goal can often require construction of a physical hydraulic model of the pump station wet well. HI standards provide physical model approach flow modeling and acceptance criteria that can be used to identify unacceptable flow patterns at the pump suction. The main evaluation criteria consist of the following:

- Swirl angle, which is a measure of the rotational velocity in the pump suction piping;
- Velocity distribution at the pump intake; and
- Free surface and subsurface vortices.

Computational fluid dynamics (CFD) provides detailed three-dimensional (3D) simulation of multiphase fluid flow to solve complex hydraulic flow problems. This aspect allows the use of CFD to solve problems that would have previously required the use of physical models. CFD simulation tools can provide valuable insights into the evaluation and design of pump approach flow conditions. These CFD simulation tools can also be used to minimize the required costs of physical modeling. CFD analysis provides an estimate of swirl angles and average velocity distribution in the pump bell, as defined by the Hydraulic Institute standards. In addition, flow characteristics in the wet well can be analyzed to identify areas of poor approach flow conditions that could lead to development of free-surface and submerged vortices. These results can then be compared against the Hydraulic Institute (HI) acceptance criteria to identify undesirable pump approach flow conditions and to evaluate improvement modifications where necessary.

12.2 USE OF CFD FOR HYDRAULIC INSTITUTE MODELING CRITERIA

It is important to note that CFD is not an exact representation of a HI standard physical model evaluation, but rather that it should be viewed as an indicator of the potential for flow issues. Swirl angle, velocity distribution, and vortex potential from CFD analysis are not recognized by the HI as a method for meeting the specific criteria of 5 degrees, 10% of the average velocity, and vortex type, respectively. Therefore, swirl angle calculations, velocity distribution, and vortex potential in CFD analysis should only be used as a general comparison of compliance with HI criteria. The focus of a CFD pump intake analysis is on the relative comparison between the modeled scenarios and geometries. The accuracy of a CFD model depends on a variety of factors and is most effective when performed in conjunction with engineering professionals experienced with both pump station design and the advantages and limitations of CFD analysis.

Swirl angle is defined as the average angle between the axial and tangential velocities at a cross-sectional plane. The swirl angle plane is located four diameters from the pump intake, as shown in Figure 12-1.

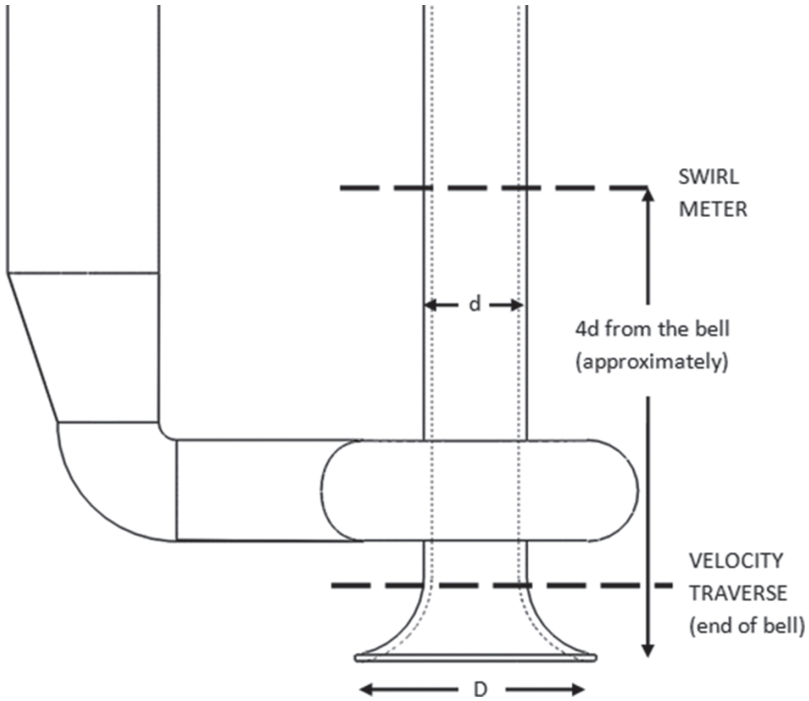

Figure 12-1. Swirl angle measurement location in a physical model.

In a physical model, the swirl angle is measured with a swirl meter, as defined in the HI standards. There are a variety of ways in which this swirl angle can be calculated using CFD. One method to calculate swirl angle from CFD data is by calculating the arctangent of the average tangential velocity divided by the average normal velocity in the pipe cross section, as shown in Equation (12-1):

$$\alpha = \tan^{-1}\left(\frac{\overline{U_{\tan}}}{\overline{U_{norm}}}\right) \tag{12-1}$$

The acceptable limit for time-averaged swirl angle is 5 degrees in a physical model. Swirl angle from CFD analysis is not recognized by the Hydraulic Institute for a measure in meeting the specific criteria of 5 degrees. Therefore, swirl angle calculations in a CFD analysis should only be used as a general comparison of compliance with HI criteria.

An intake velocity distribution is defined as acceptable if the velocity throughout the cross section at the pump intake is within 10% of the average velocity. Figure 12-2 shows an example of how the velocity distribution is measured in a physical model.

The velocity at the end of the bell in a CFD model can be extracted from each of the finite volume locations to produce a velocity distribution at the pump

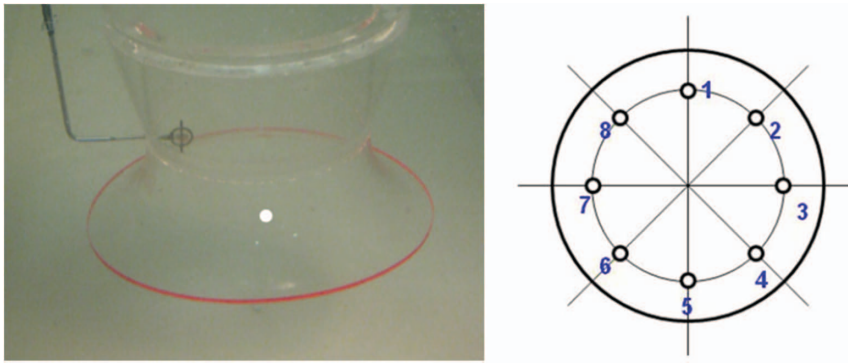

Figure 12-2. Physical model velocity measurement probe and measurement location pattern in the pump intake bell.

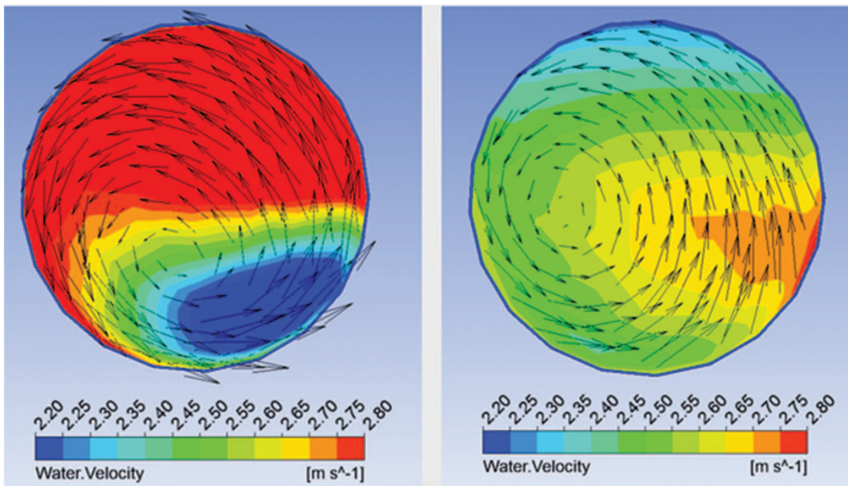

Figure 12-3. Velocity distribution examples from CFD analysis.

suction. These velocities can be plotted with a velocity legend to illustrate areas that are greater than and less than 10% of the average velocity. For example, in Figure 12-3 the areas that are dark red are greater than 10% higher than the average velocity, and those areas that are dark blue are less than 10% below the average velocity. These areas of dark red and dark blue do not meet the HI criteria. Figure 12-3 shows an example of poor velocity distribution on the left and good velocity distribution on the right.

In general, desirable flow approach characteristics consist of an approach velocity less than 0.5 m/s (1.5 ft/s), adequate depth to reduce the potential of surface vortices, a constant flow acceleration toward the pump, and no regions of flow separation or recirculation. Regions of recirculation can spawn surface and

subsurface vortices, which can be detrimental to pump operation. The HI standards provide a classification for the various types of surface and subsurface vortices that may occur in a physical model. In addition, the HI standards provide criteria for which types of vortices are acceptable and which types are not acceptable. The HI standard vortex types are shown in Figure 12-4. The vortex types within the red boxes do not meet the HI acceptance criteria.

CFD is not able to specifically identify the vortex classification type as defined by HI standards. However, through the use of tools developed by comparison of hydraulic parameters to physical model vortex activity, CFD analysis can be used

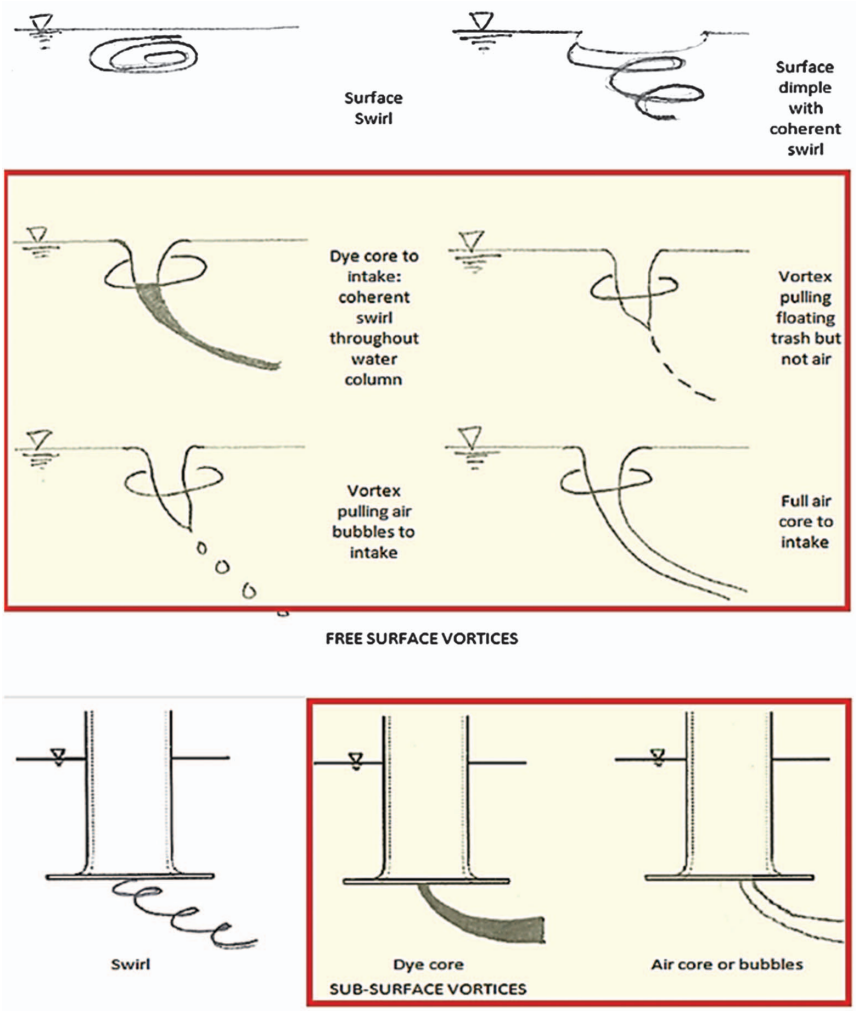

Figure 12-4. Classification of free-surface and subsurface vortices, as defined by HI standards.

to identify areas of potential vortex activity. Figures 12-5 and 12-6 show a comparison between vortex activity in a physical model, as visualized using tracer dye, and potential vortex activity in the CFD model, as identified by lambda 2 values and marked with streamlines.

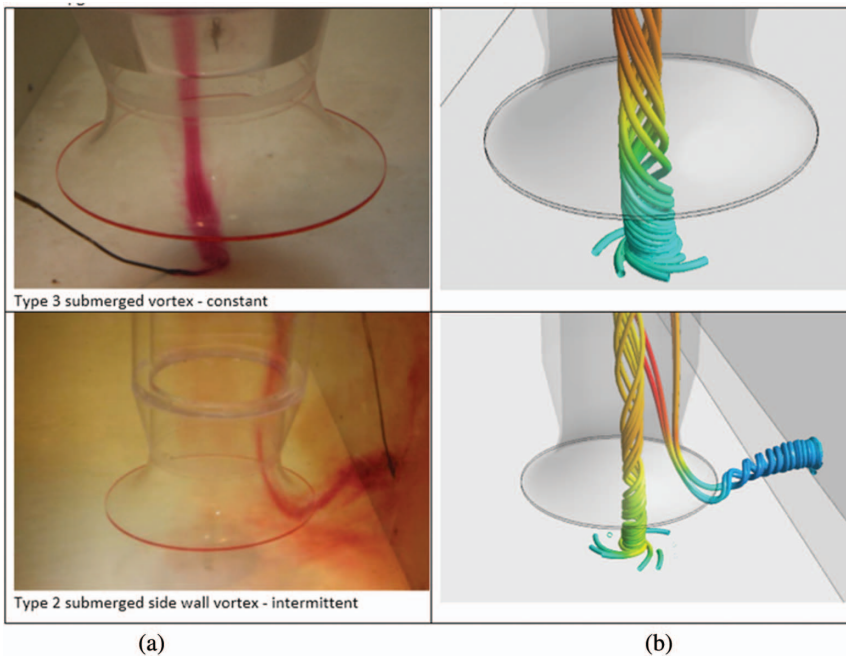

Figure 12-5. (a) Physical model subsurface vortex activity compared to (b) CFD analysis of potential vortex activity.

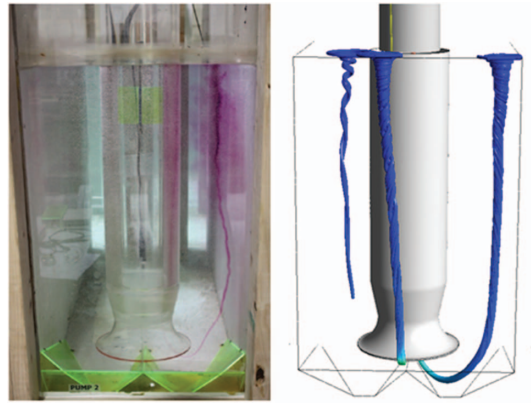

Figure 12-6. Physical model surface vortex activity compared to CFD analysis of potential vortex activity.

12.3 PHYSICAL MODEL AND CFD COMPARISONS

When using CFD to evaluate approach conditions for pump stations, it is important to understand the advantages and disadvantages of both physical modeling and CFD modeling of pump station approach conditions. The following should be considered when deciding on the modeling approach and the use of CFD:

- Physical modeling is accepted by the Hydraulic Institute, whereas CFD modeling is not.
- CFD modeling is usually an order of magnitude less expensive.
- CFD modeling can be performed with significantly less time.
- CFD modeling allows for efficient evaluation of several alternatives.
- Physical modeling can predict vortex classification, whereas CFD modeling can only identify potential vortex activity.
- CFD modeling can predict swirl angles; however, the reference criteria are based on the physical model testing vane. In addition, vortices can affect swirl angle, which CFD does not capture with average velocity vector calculations.
- CFD provides much more spatial detail about velocity distribution. Time-varying analysis can be performed using transient CFD simulation methods. However, this analysis requires additional computational time and resources to generate accurate results.

Although significant progress has been achieved using CFD in evaluation of pump approach conditions, additional work is still required to develop reliable CFD pump intake evaluation methodologies. A summary of conclusions developed between previous comparisons of CFD to physical model evaluations is listed here:

- Vortex comparison: Vortex algorithms, such as lambda 2 or swirling strength, provide the best correlation to physical model results.
- Swirl comparison: Trends of swirl angle are captured by CFD, but individual swirl measurements are loosely correlated to physical model observations. In addition, CFD results are significantly affected by vortex activity, and they often underpredict swirl angle when there is significant vortex activity.
- Velocity distribution comparison: Velocity comparisons show generally good agreement between CFD and physical modeling, but they are sensitive to where the physical model measurements are taken. In addition, physical models may miss regions of high or low velocity within the intake velocity plane.
- CFD results are extremely sensitive to the volume mesh size, meshing schemes, model run times, turbulence models, and time steps. Generally, sensitivity analyses are recommended to evaluate solution accuracy with respect to mesh and model parameters.

- Adequate mesh size, run times, and time step require an exponential increase in computational power. This requirement makes only simple projects suitable for desktop or workstation analysis. More complex problems require cluster computational server architecture to adequately perform the CFD analysis in a reasonable time.
- CFD is a powerful tool to assist with pump station design, and it can efficiently assist in the evaluation of potential alternatives.
- Physical modeling is currently still required for confirmation of final configurations to meet the HI acceptance criteria.

Where possible, the recommended approach is to use CFD modeling in conjunction with physical modeling to evaluate pump approach conditions. The CFD model can be used to efficiently evaluate layout alternatives and determine potential remedial measures. The physical model can then be used for refinement of alternatives and final documentation of performance. This conjunctive use of CFD and physical modeling can often lead to the most cost-effective way to develop acceptable pump intake designs.

12.4 CFD SIMULATION OF PUMP INTAKE CHAMBER

12.4.1 Background

One important component of a water and wastewater treatment plant is the pump intake system. The main purpose of the intake system is to reliably deliver an adequate quantity of water of the best quality (Baruth 2005). In many water and wastewater treatment plants, the pump intake chamber is a critical location where hydraulic issues (Claxton 1998), such as vortex and air entrainment, are prone to occur and therefore is of particular interest to CFD modelers as well. A simple but typical pump intake system may consist of either a wet well or channel leading to a pump intake chamber.

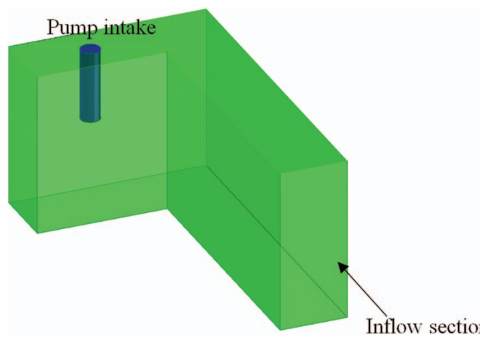

Figure 12-7. General geometry setup for the CFD demonstration case study.

Table 12-1. Information Related to the CFD Simulation

Flow conditions	Items		Reference
	System	Single bay L-shaped channel leading to a pump intake	
	Geometry	Figure 12-7	Demonstration case study
	Dimensions	500 in. × 300 in. × 205 in. ID = 13.5 in., OD = 14.0 in. or 12.7 m × 7.62 m × 5.207 m ID = 0.343 m, OD = 0.3556 m	
	Model flow rate	10 million gal./day (i.e., 0.44 m^3/s)	
	Reynolds number	8.4×10^4 (at inlet, based on inlet width)	
Model information	**Simulation**	**Method or Governing Equation**	**Reference**
	Type	RANS finite volume	
	Flow	N-S equation	Section "CFD Model"—See Chapter 4 for model description
	Turbulent SGS model	Realizable k-ε model	
Software used	**Type of software**	**Name of software**	**Availability**
	Meshing tool	Trelis	Commercial
	Solver	Fluent	Commercial
	Postprocessing tool	Tecplot 360	Commercial
Computational information	**Items**	**Remarks**	
	Computational grid	1,790,000 elements	
	Computing device equivalent	Mobile workstation, 8-core CPU, RAM 64 GB	
	Computing time	2 h	

The use of CFD to simulate a pump intake chamber have been well documented in literature such as Li et al. (2006), where different aspects of pump intake design, including evaluation of swirl angles within the pump suction, have been demonstrated. The simple case study in the following section is a hypothetical one, with the intention of demonstrating the application potential of CFD in predicting the presence of vortex near a pump intake.

12.4.2 Objectives

1. Identification of vortex location near a single pump intake shown in Figure 12-7.

12.4.3 Results and Discussion

12.4.3.1 Vortex Prediction and Identification

To demonstrate a case study with vortex formation near a pump intake, a hypothetical L-shaped approach channel was intentionally used, shown in Figure 12-7. The reasoning behind using this geometry is to create an uneven velocity distribution to induce the formation of vortex, for demonstration

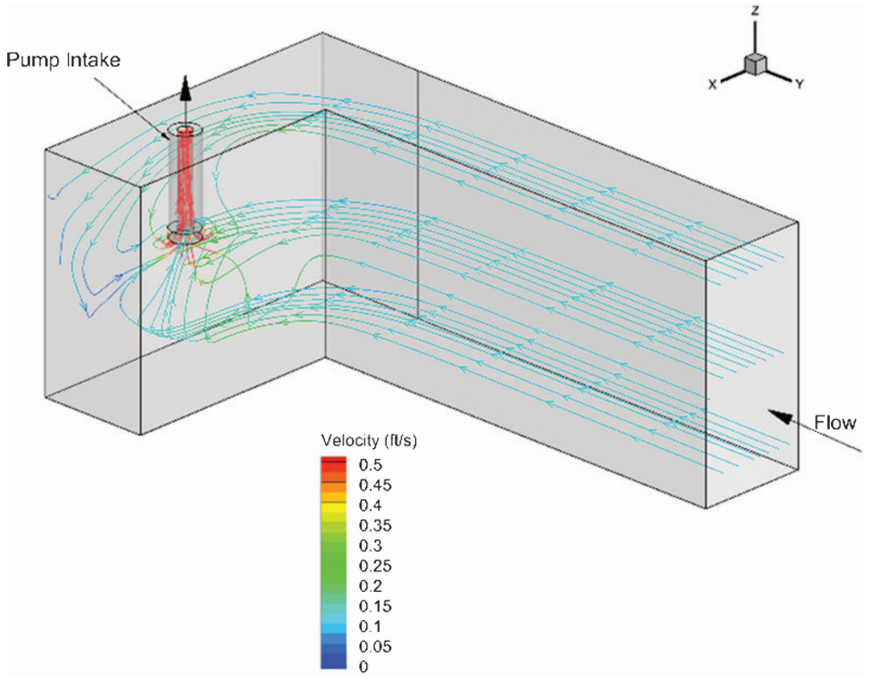

Figure 12-8. CFD results of uneven velocity distribution in the approach channel at the bend.

purposes. In this simulation, a pump intake was placed at the end of the L-shaped channel and an intake flow rate of 10 million gal./day (i.e. 0.44 m^3/s) was used. More details of the simulation are listed in Table 12-1.

Figure 12-8 showed the streamline of approach velocity in the *XY* plane immediately after the bend. The streamlines converge at the intake and enter the intake at different velocities. The magnitude of velocity can be seen in Figure 12-9 to differ spatially in the horizontal plane. Further examination of the velocity magnitude in the vertical plane in Figure 12-9 shows steep velocity gradients, especially at the far end of the channel, an indicator of potential vortex formation near the intake.

In Figure 12-10, streamlines were drawn at locations where potential vortices may form. The streamlines showed swirling motion starting from the surface and extending into the pump intake column. Three surface vortices (S1, S2, and S3 in Figure 12-10) were identified using the CFD model. The largest vortex, S1, formed at the inside of the bend near the intake, and two other vortices, S2 and S3, were identified at the end of the intake bay.

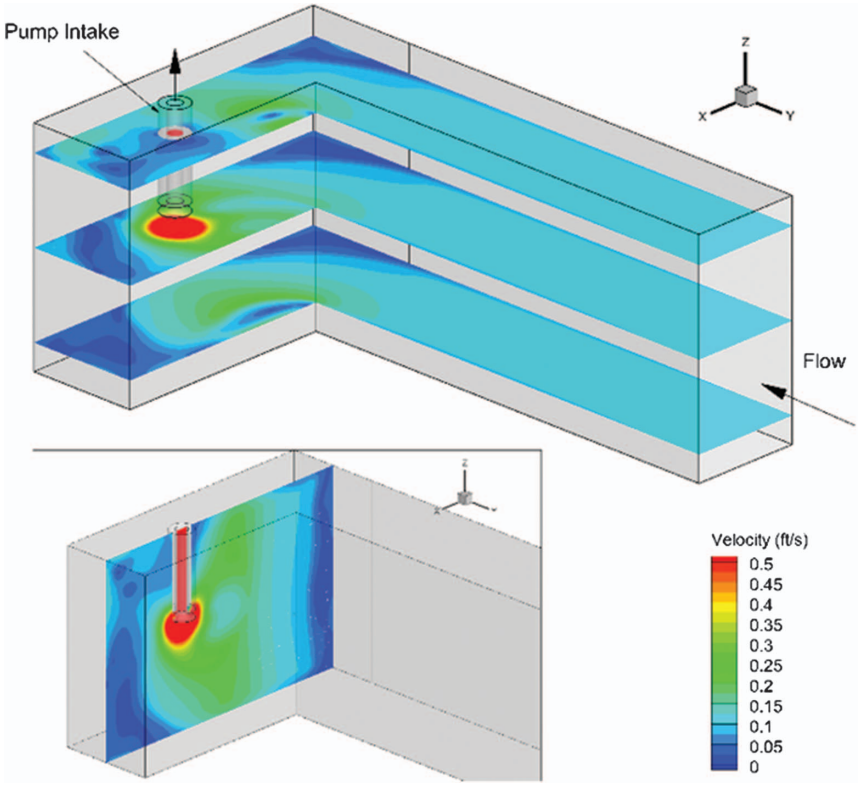

Figure 12-9. Velocity magnitude plot at different cross sections in the horizontal and vertical plane.

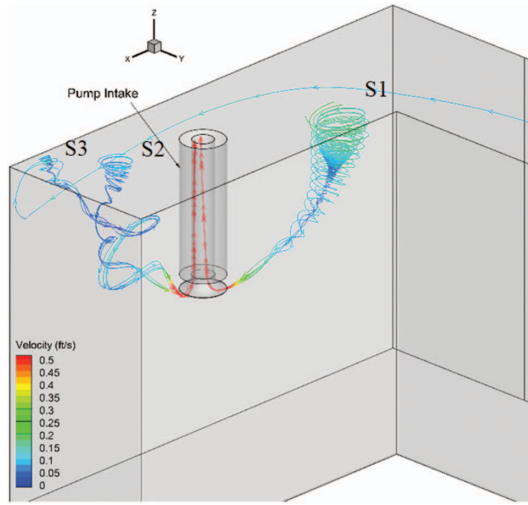

Figure 12-10. Streamline of the three vortices S1, S2, and S3 identified near the pump intake.

12.4.3.2 Other Considerations

The simulation showed the capability of CFD as a tool to identify vortices and problems related to the flow dynamics near a pump intake. Often, vortex formation can be mitigated by using antivortex devices. These structures may be such shapes as cones, walls, or fillets, as mentioned in Choi et al. (2010). CFD can be used to study the effectiveness of the vortex suppression devices based on the placement and dimensions of these devices. Another application of CFD in pump intake simulations is in estimating the swirl angles (Li et al. 2006) within the pump intake. Currently, the role of CFD for pump intake study is still in its infancy, and CFD should not be regarded as a direct substitute for a physical model. However, the use of CFD as a prediction tool is demonstrated in this case study and can be seen as advantageous when used in preliminary pump intake studies.

References

Baruth, E. E. 2005. *Intake facilities: Water treatment plant design*. 4th ed. New York: McGraw-Hill.

Choi, J.-W., Y.-D., Choi, C.-G., Kim, and Y.-H., Lee. 2010. "Flow uniformity in a multi-intake pump sump model." *J. Mech. Sci. Technol.* **24** (7): 1389–1400.

Claxton, J. 1998. *American national standard for pump intake design: ANSI/HI 9.8-1998*. Parsippany, NJ: Hydraulic Institute.

Li, S., J. M., Silva, Y., Lai, L. J., Weber, and V. C., Patel. 2006. "Three-dimensional simulation of flows in practical water-pump intakes." *J. Hydroinf.* **8** (2): 111–124.

CHAPTER 13

Flow Distribution to Multiple Treatment Trains

Carrie L. Knatz

13.1 BACKGROUND

Many treatment facilities have multiple, parallel treatment trains to be able to handle a range of flows. A common influent channel is the most typical configuration to split the flow into multiple treatment trains. If hydraulics is not considered in the design of the influent channel, a significant maldistribution of flow can occur resulting in failure to meet treatment performance requirements. Often energy-intensive assemblies such as flowmeters and flow-regulating valves are used to achieve equal flow distribution. Less energy-intensive options that use structural components such as rectangular weirs, V-notch weirs, and submerged orifices are also used (Benefield et al. 1984). Since energy is often not readily available when upgrading treatment plants, engineers are challenged with finding a design that balances energy, cost and performance. Table 13-1 provides the information related to the CFD analysis performed to evaluate flow distribution into the multiple DAF treatment trains.

The Haworth water treatment plant in Oradell, New Jersey, provides up to 710 m^3/day of water to 800,000 users in north New Jersey. Treatment plant upgrades were identified in response to new, stringent drinking water regulations and growing customer demands. The upgrades included ozone for pre-oxidation, high-rate dissolved air flotation (DAF), intermediate disinfection, filtration, and final disinfection. Early engineering identified that the new processes would have to function with as little as 0.46 m of available energy at peak flow. The challenge to the design team at Haworth was to find a solution that used minimal energy and achieved optimal distribution of solids and flow to the multiple DAF process trains. CFD was identified as a valuable design tool to evaluate low energy flow distribution configurations. Figure 13-1 presents the original design configuration (Configuration 1) of the DAF influent channel, and Figure 13-2 presents the modifications (Configurations 2 through 5) evaluated, which were intended to improve flow distribution. The design of the DAF influent channel consisted of a

Table 13-1. Information Related to the CFD Simulation

Flow conditions	Items		Reference
	System based on	A full-scale DAF influent channel operated by United Water, Haworth, NJ	Design–build contract documents 2011
	Geometry	Figure 13-1	Knatz et al. (2015)
	Dimensions	494 ft × 24 ft × 18 ft	
	Flow rate	187 million gal./day	Peak day flow
Model information	Simulation	Method or Governing Equation	Reference
	Type	RANS	Chapter 5
	Flow	RKE	
	Reaction system	1 species/0 reactions	Knatz et al. (2015)
Software used	Type of software	Name of software	Availability
	Meshing tool	Gambit	Commercial
	Solver	Fluent	
	Postprocessing tool	Fluent	
Computational information	Items	Remarks	
	Computational grid	Unstructured, 600,000 cells	
	Computing device equivalent	2 cores + 32 GB RAM	
	Computing time	~12 h	

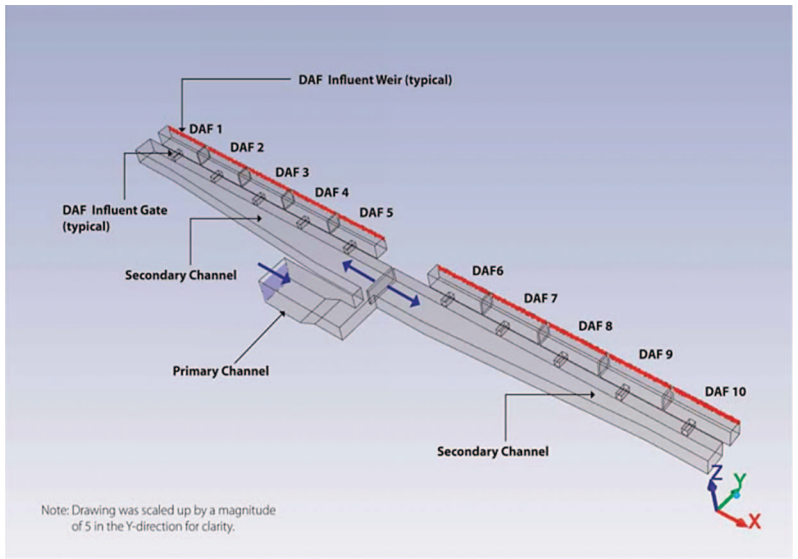

Figure 13-1: Initial influent channel configuration (Configuration 1) model domain. Note*: The model domain was scaled up by a factor of 5 in the Y-direction for clarity in the illustration.*
Source: Courtesy of IWA; reproduced with permission.

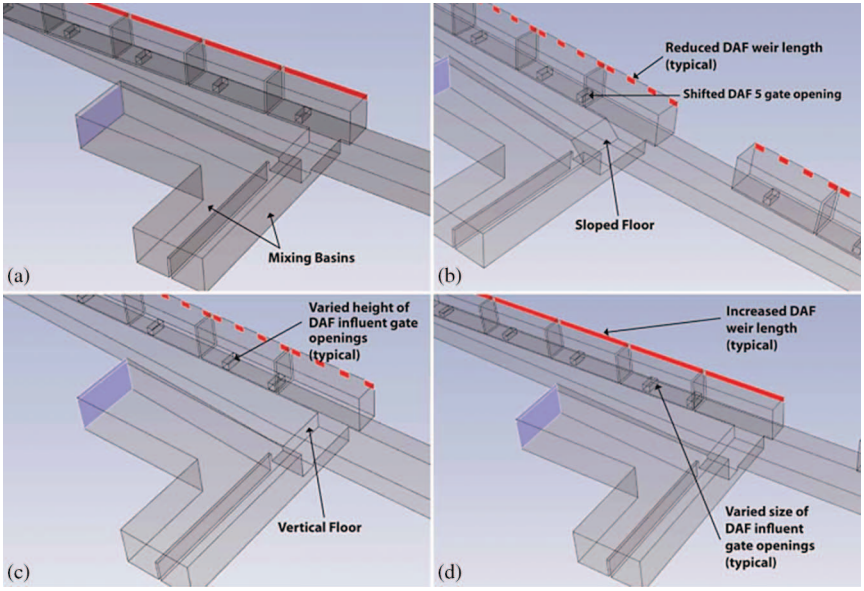

Figure 13-2: Illustration of different features for each configuration: (a) Configuration 2, (b) Configuration 3, (c) Configuration 4, (d) Configuration 5.
Source: Courtesy of IWA; reproduced with permission.

primary channel that feeds two secondary channels, each delivering flow to five DAF units. From the secondary influent channels, the flow enters each DAF unit through an influent gate opening and then over an influent weir.

13.2 OBJECTIVES

1. Achieve equal flow split from the primary influent channel to each of the two secondary influent channels.
2. Achieve ±10% deviation from equal flow split from the secondary influent channels to each of the ten-individual dissolved air flotation (DAF) treatment process trains.
3. Minimize headloss associated with the influent channel design.

13.3 RESULTS AND DISCUSSION

Primary Flow Split: Figure 13-3 presents the primary flow split from the primary channel to the two secondary channels. To address the issue of the primary flow

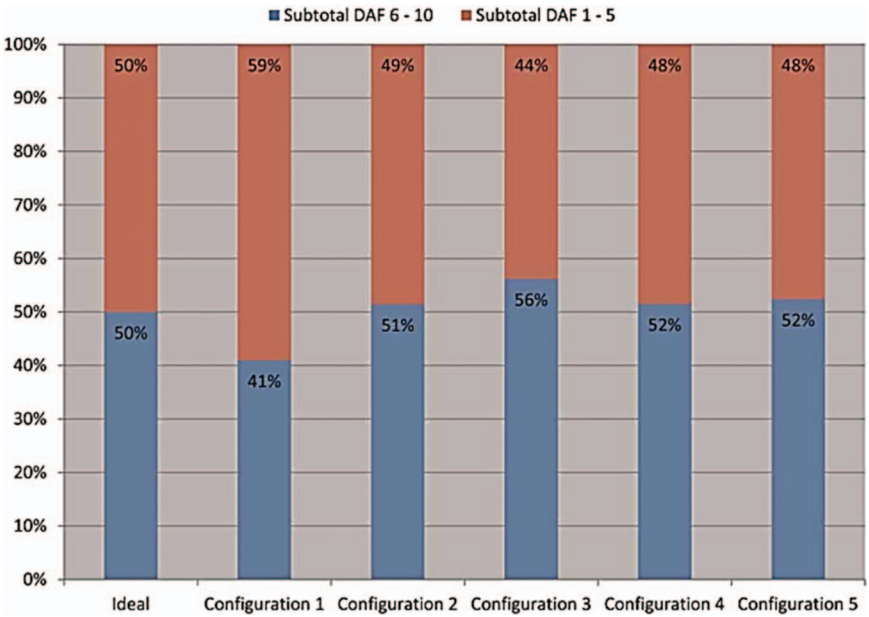

Figure 13-3: Primary flow split for various configurations.
Source: Courtesy of IWA; reproduced with permission.

split maldistribution exhibited for Configuration 1, two mixing basins were introduced between the primary and secondary channels. The primary channel flow enters the first of two mixing chambers, goes over a baffle wall to the second mixing chamber, then under a baffle wall and up where it splits to the two secondary channels. This design change improved the flow distribution from the primary channel to the secondary channels.

Secondary Flow Split: The flow distribution from the secondary channels to the individual DAF units (secondary flow split) was evaluated based on the percentage deviation from the ideal. Flow was calculated where a maximum of 10% deviation was considered acceptable. Figure 13-4 presents the secondary flow split for Configurations 1, 2, and 3. Although the flow distribution was improved from Configuration 2 to Configuration 3, it was still higher than the ±10% criterion.

After analyzing the flow field near the DAF Unit 5 influent gate, it was apparent that the flow exiting the last mixing basin projects a jet up and over the DAF Unit 5 opening, resulting in a non-uniform velocity profile and starving the flow entering the unit (Figure 13-5).

To address this issue, the DAF Unit 5 gate opening was moved off-center, and the floor was sloped at the upstream end of the DAF Units 1 through 5 secondary channel for Configuration 3. Figure 13-6 presents the results for Configuration 3 demonstrating lower velocity exiting the last mixing basin.

The next approach to improving the flow distribution was to vary the size of the influent gate openings from largest at the upstream DAF unit and smallest at the downstream DAF unit. Momentum carries the bulk flow to the downstream end of the channel but with small openings downstream and larger openings upstream more flow is forced upstream. Figure 13-7 presents the secondary flow

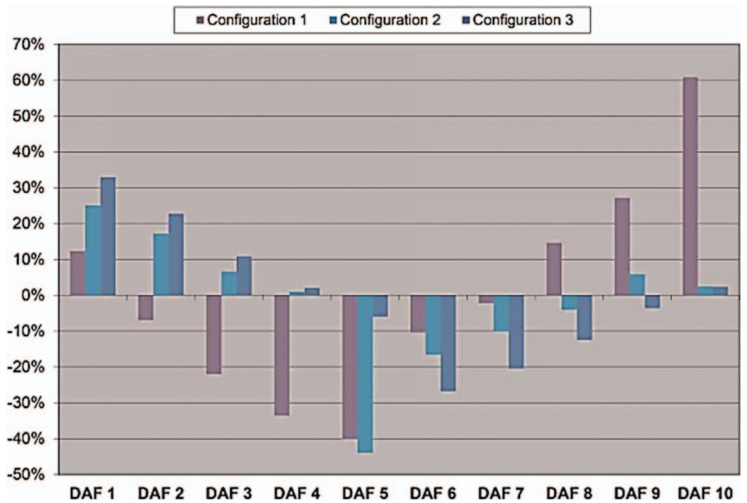

Figure 13-4: Percent deviation of secondary flow split for Configurations 1, 2, and 3 (negative value = less than ideal; positive value = more than ideal).
Source: Courtesy of IWA; reproduced with permission.

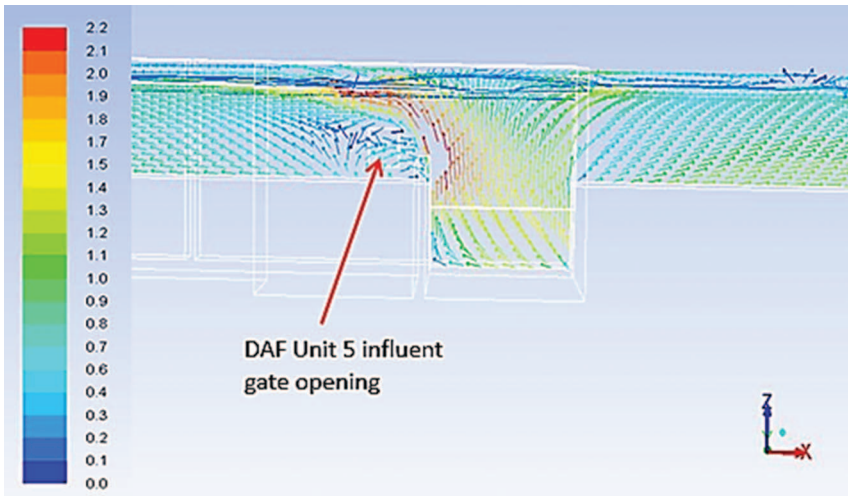

Figure 13-5: Velocity vectors (m/s) in a vertical section through the secondary channel for Configuration 2.
Source: Courtesy of IWA; reproduced with permission.

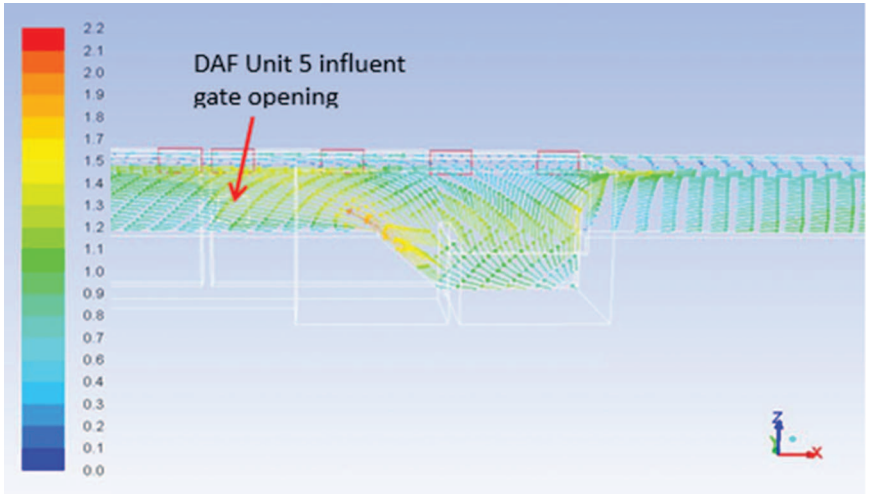

Figure 13-6: Velocity vectors (m/s) in a vertical section through the secondary channel for Configuration 3.
Source: Courtesy of IWA; reproduced with permission.

split for Configurations 4 and 5. Configuration 4 varied the heights of each DAF influent gate opening. In addition, to further improve the secondary flow split, Configuration 5 varied the widths and heights of each DAF influent gate opening.

Physical Data Validation: Upon completion of the treatment plant upgrades, the flow distribution predicted by the CFD analysis was confirmed by data

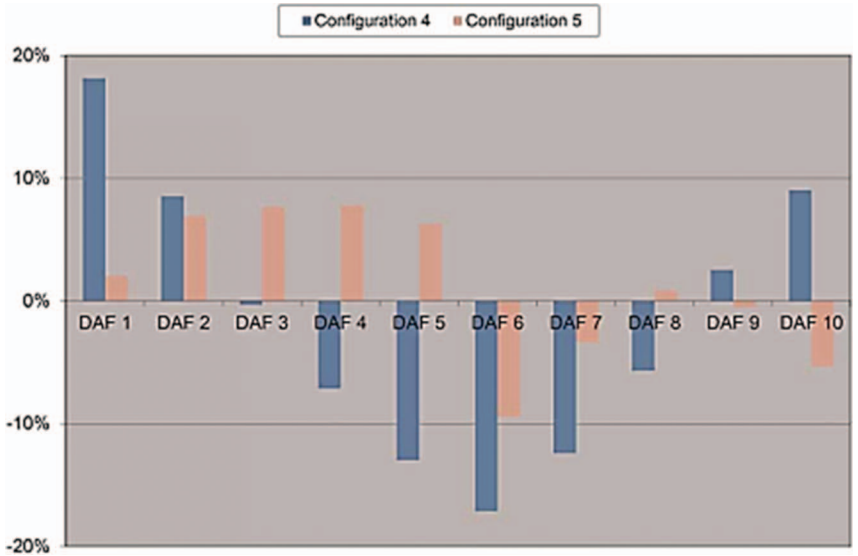

Figure 13-7: Percent deviation of secondary flow split for Configurations 4 and 5.
Source: Courtesy of IWA; reproduced with permission.

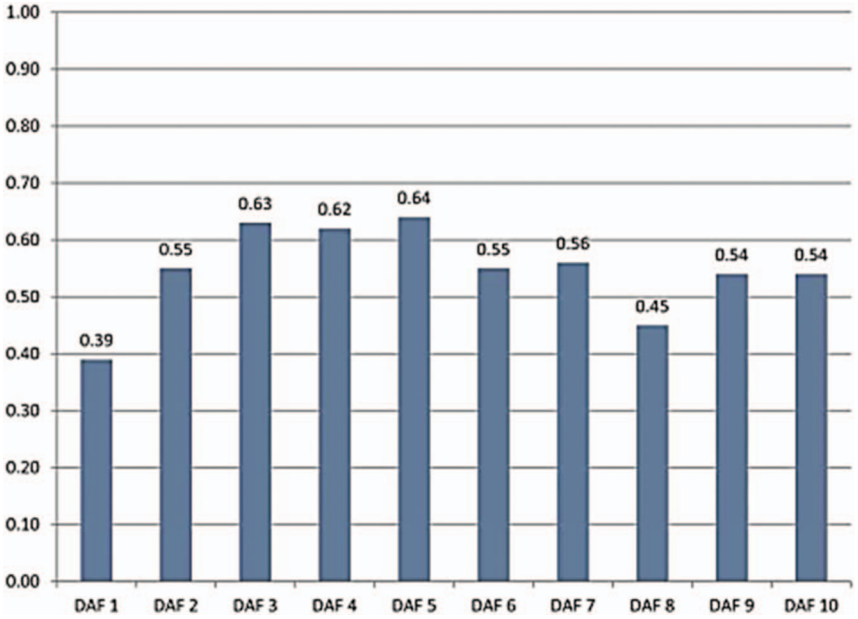

Figure 13-8: Actual average turbidity levels for the various DAF units.
Source: Courtesy of IWA; reproduced with permission.

obtained by the turbidity analyzer that had been installed at each of the ten DAF units. The average turbidity over a five-month period was relatively close for all units indicating that solids were evenly distributed and removed (Figure 13-8).

References

Benefield, L. D., J. F. Judkin, and A. D. Parr. 1984. *Flow in open channels, treatment plant hydraulics for environmental engineers*. New York: Prentice-Hall, 108–122.

Knatz, C. L., S. Rafferty, and A. Delescinskis. 2015. "Optimization of water treatment plant flow distribution with CFD modeling of an influent channel." *Water Qual. Res. J. Can.* **50** (1), 72–82.

CHAPTER 14

Aerated Grit Tank Improvements

Carrie L. Knatz

14.1 BACKGROUND

Aerated grit tanks are commonly used in the preliminary treatment of wastewater to minimize potential problems with treatment processes caused by large solids and grit, which cause undue mechanical wear and increased equipment maintenance. Grit is removed by inducing a spiral flow pattern through the aerated grit tank. Air is introduced in the grit tank along one side, causing a perpendicular spiral flow pattern where heavier particles drop to the bottom of the tank and lighter, organic particles are suspended and eventually carried out of the tank (EPA 2003).

The interaction of the air particles with the primary water flow through the tank was modeled using the discrete phase model (DPM), which injects discrete particles specified as air bubbles at the diffuser locations. Table 14-1 provides information related to the CFD analysis used as a design tool to improve the process performance in the aerated grit tanks.

14.2 OBJECTIVE

Evaluate proposed retrofit design alternatives to improve hydraulic conditions, grit capture, and grit deposition in the existing aerated grit tank. Flow path lines colored by velocity were visually inspected to evaluate the organization of a spiral flow pattern to demonstrate the desirable hydraulic conditions.

14.3 RESULTS AND DISCUSSION

Figure 14-1 presents the configuration of an existing aerated grit tank where the influent enters the tank via a 90-degree channel bend on the side of the tank

Table 14-1. Information Related to the CFD Simulation

Flow conditions	Items		Reference
	System based on	Metropolitan Syracuse Wastewater Treatment Plant, Syracuse, NY	Record drawings 1997
	Geometry	Figure 14-1	
	Dimensions	63 ft × 13 ft × 11 ft	
	Flow rate	10 million gal./day per tank (84 million gal./day facility)	Design flow
Model information	**Simulation**	**Method or Governing Equation**	**Reference**
	Type	RANS	Chapter 5
	Flow	Realizable *k*-epsilon model, DPM	
	Reaction system	2 species/0 reactions	
Software used	**Type of software**	**Name of software**	**Availability**
	Meshing tool	Gambit	Commercial
	Solver	Fluent	
	Postprocessing tool	Fluent	
Computational information	**Items**	**Remarks**	
	Computational grid	Unstructured, 200,000 cells	
	Computing device equivalent	1 core + 16 GB RAM	
	Computing time	~12 h	

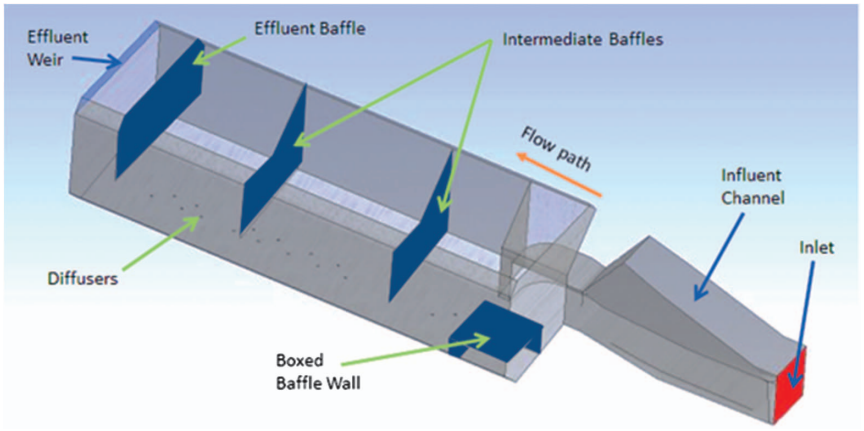

Figure 14-1. Existing (baseline configuration) aerated grit tank configuration.

opposite from the air diffusers. Flow enters the tank and hits a boxed baffle wall that protects the grit collector sumps. Two intermediate baffle walls split the tank into thirds, and an effluent under-baffle wall forces the flow low to mitigate solids from exiting over the effluent weir. Three CFD simulations were evaluated:

- Baseline:
  - Used existing tank configuration and
  - Used existing airflow rate;
- Alternative 1:
  - Removed intermediate baffle walls,
  - Modified the boxed baffle wall, and
  - Doubled the airflow rate; and
- Alternative 2:
  - Preserved the intermediate baffle walls,
  - Modified the boxed baffle wall, and
  - Doubled the airflow rate.

Figure 14-2 presents the modified boxed baffle wall included in Alternative 1 and Alternative 2 configurations. Figures 14-3, 14-4, and 14-5 present the path lines colored by velocity for the Baseline, Alternative 1, and Alternative 2 configurations, respectively. Although the spiral flow pattern is demonstrated in the Baseline configuration, the intermediate baffle wall is disrupted. Also, the boxed baffle wall forces the flow to divert around the vertical wall parallel to the length of the chamber. The spiral flow pattern is more organized in the Alternative 1 configuration; this is mainly attributed to the increased airflow rate. The angled, boxed baffle wall allows the flow to be carried above the box rather than diverted around the box in the Baseline configuration. The spiral flow pattern in the

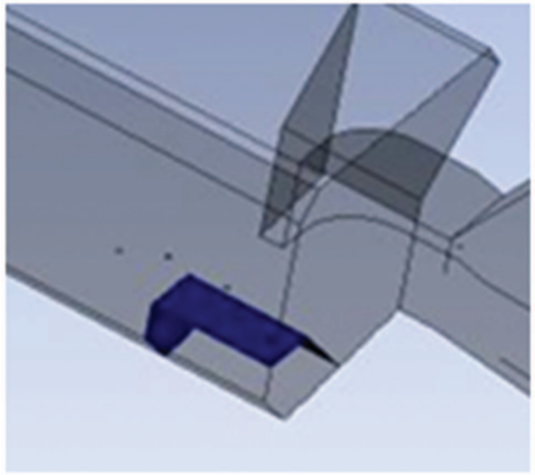

Figure 14-2. Illustration of the modified boxed baffle wall.

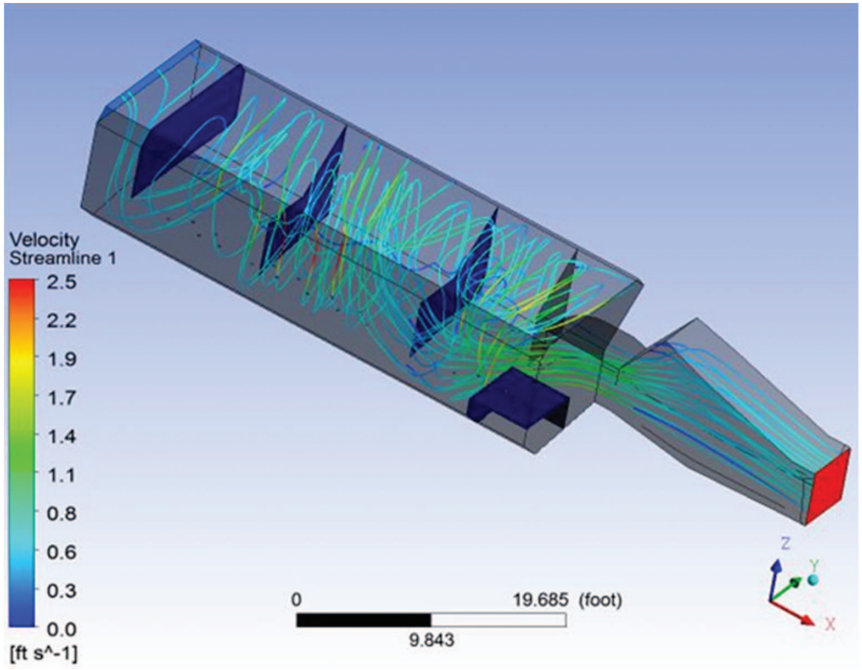

Figure 14-3. Baseline configuration path lines colored by velocity.

Alternative 2 configuration is similar to the Alternative 1 Configuration. Since it was not apparent whether the removal of the intermediate baffle walls would provide valued improvement, it was not recommended, considering the high

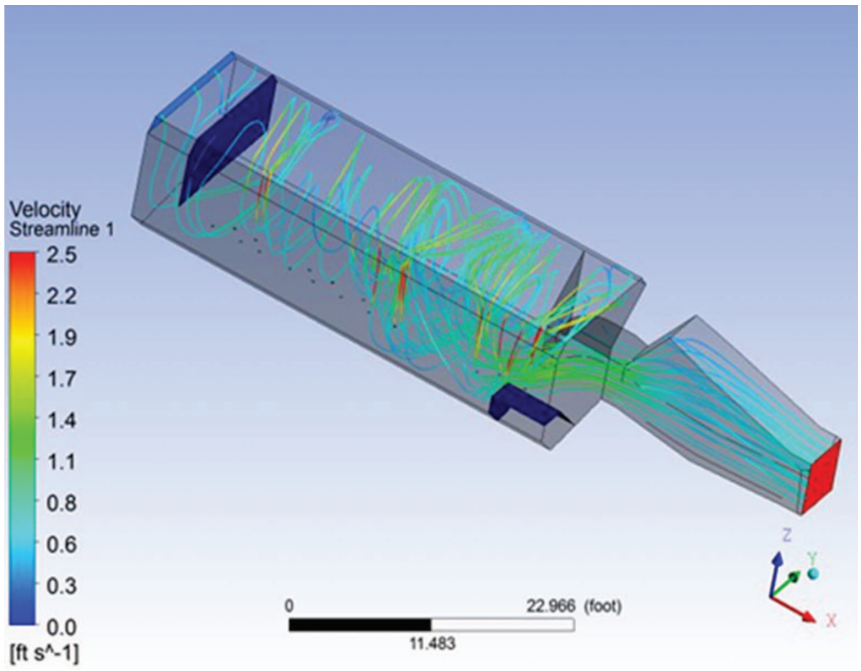

Figure 14-4. Alternative 1 configuration path lines colored by velocity.

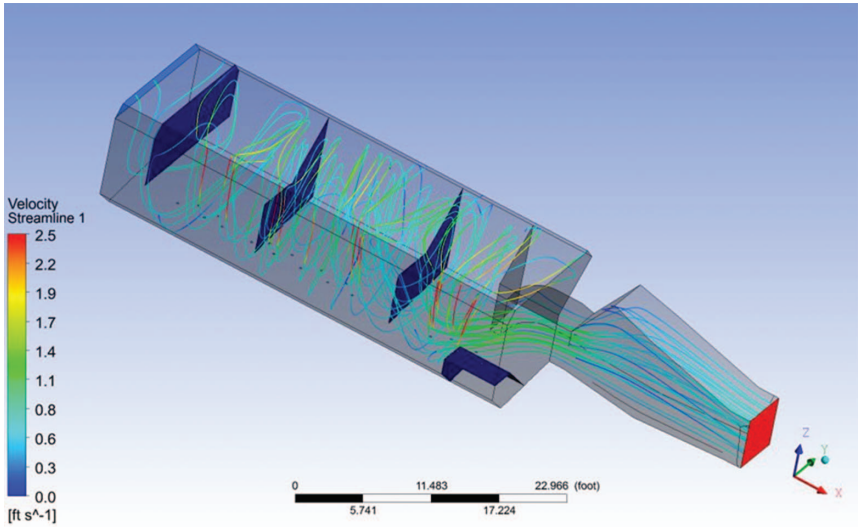

Figure 14-5. Alternative 2 configuration path lines colored by velocity.

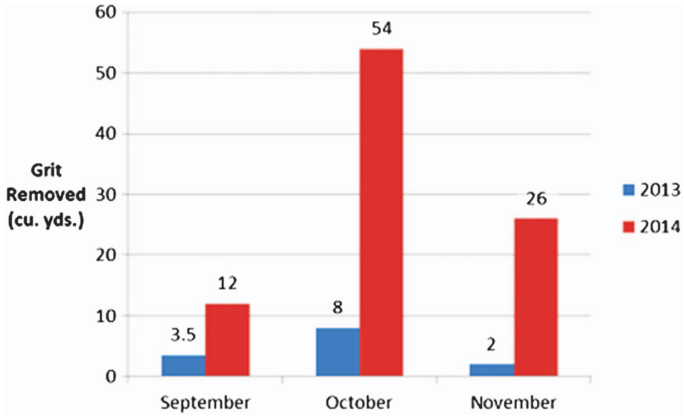

Figure 14-6. Grit removal before and after construction of modifications.

construction cost to remove the baffle walls. Therefore, the recommended improvements included the modified boxed baffle wall and increased airflow rate.

Demonstrated Benefit of the CFD Analysis: Figure 14-6 presents the grit removal data obtained before and after the modifications. The data show that seven times more cubic yards of grit was captured after construction, demonstrating the success of the improvements.

Reference

EPA. 2003. *Wastewater technology fact sheet screening and grit removal.* Washington, DC: EPA.

CHAPTER 15

Optimization of Residence Time Distribution in Small Water Treatment Systems

Jordan M. Wilson
Subhas Karan Venayagamoorthy

15.1 BACKGROUND

Many small public water treatment facilities lack the necessary financial and professional resources to meet standard disinfection requirements. A 2011 report by the US Environmental Protection Agency found that small treatment systems are responsible for 95% of the maximum contaminant level (MCL) violations, yet they serve only 18% of the population (EPA 2011). Increasing the knowledge on hydraulic efficiency of small contact tanks is crucial to provide operators with improved guidance to ensure compliance. Although the *Disinfection Profiling and Benchmarking Technical Guidance Manual* (EPA 2003) provides basic guidance on contact tank efficiency based on geometric characteristics, it does not address more complex tank configurations or influent and/or effluent piping configurations. These design elements can have a significant impact on the hydraulic disinfection efficiency of small contact tanks.

The objective of the presented case studies is to the highlight the capabilities of computational fluid dynamics (CFD) for improving hydraulic disinfection efficiency, as indicated by the baffling factor, *BF*, in small contact tank systems. The *baffling factor* is defined as the ratio of the time for 10% of the flow to pass through the system, or t_{10}, to the hydraulic residence time, which is the tank volume divided by the flow rate. The presented case studies were part of a multiyear joint research project between the Colorado Department of Public Health and Environment's Water Quality Division and Colorado State University's Department of Civil and Environmental Engineering, a project which generated the *Baffling Factor Guidance Manual* (CDPHE 2014). This manual provides guidance on preengineered systems and design modifications for existing systems to improve efficiency (Table 15-1).

Table 15-1. Information Related to the CFD Simulation

Flow conditions	Items		Reference
	System based on		
	Geometry	Figure 15-1	Wilson 2011
		Figure 15-2	Taylor 2012
		Figure 15-3	Wilson 2011
	Dimensions	Diameter = 1.22 m	
		Height = 1.7 m	
		Volume = 500 gal.	
	Flow rate	5–30 gal./min	
Model information	**Simulation**	**Method or Governing Equation**	**Reference**
	Type	RANS	
	Flow	Standard k-ε	
	Reaction system	————————	
Software used	**Type of software**	**Name of software**	**Availability**
	Meshing tool	Ansys Mesher v12.1	Commercial
	Solver	Fluent v12.1	Commercial
	Postprocessing tool	Fluent v12.1	Commercial
Computational information	**Items**	**Remarks**	
	Computational grid	Unstructured, 260,000 to 2.5 million cells	
	Computing device equivalent	Desktop workstation (4-core, 16 GB RAM)	
	Computing time	Varied from 6 to 24 h	

15.2 OBJECTIVES

1. Case Study 1
   a. Evaluate the hydraulic efficiency (which is the ratio: t_{10}/hydraulic residence time or HRT) for a nonpressurized, vertical 500-gal. polyethylene tank with a 90-degree inlet oriented 45 degrees down from the horizontal (Figure 15-1).
   b. Design and test low-cost inlet alternatives for hydraulic efficiency improvements (Figure 15-2).
2. Case Study 2
   a. Evaluate the hydraulic efficiency of 80 gal. pressurized fiberglass tanks individually and in 2-, 3-, 4-, 5-, and 6-tank series configurations (Figure 15-3).

15.3 RESULTS AND DISCUSSION

15.3.1 Case Study 1

The unmodified tank exhibits significant short-circuiting as the flow enters the tank, follows the perimeter of the tank briefly, and exits the tank, as shown in Figure 15-4. This observation is further validated by the residence time distribution (RTD) curve in Figure 15-5. The baffle factor for the unmodified configuration is 0.1.

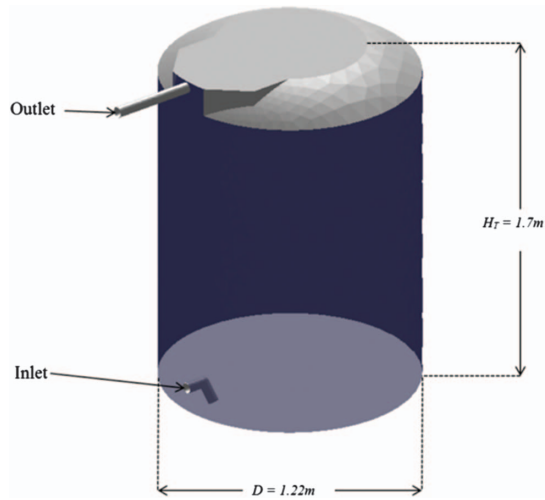

Figure 15-1. Case study 1—Unmodified nonpressurized tank configuration.

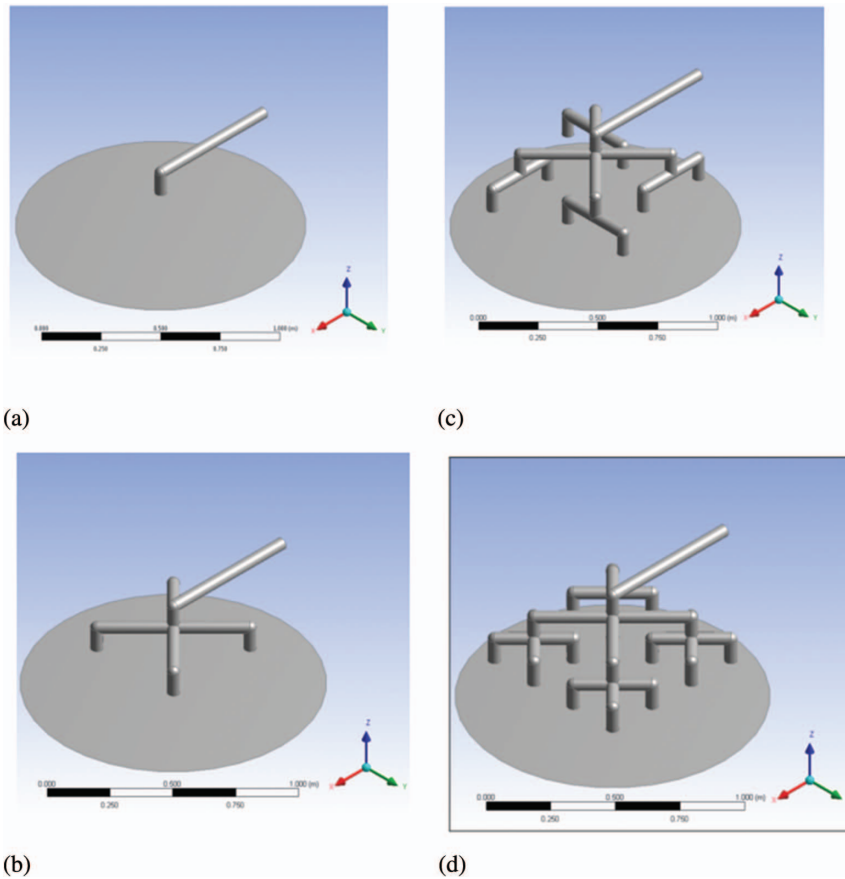

Figure 15-2. Case study 1—Inlet diffuser alternatives with (a) 1, (b) 4, (c) 8, and (d) 16 inlets.

By redistributing and dissipating some of the kinetic energy from the jet at the tank's original, unmodified inlet, the hydraulic efficiency can be improved. A parametric study was conducted that varied the number of inlets and the height of the inlets above the tank floor. The inlet diffusers were based on 4 in. PVC piping with inlets evenly spaced across the floor of the tank. The hydraulic efficiency was maximized for the 16-inlet configuration for both flow rates with the inlet location 0.1 times the height of the tank, or 0.18 m, from the floor (Figure 15-6). The configuration gives a final baffle factor of 0.5, improving the contact time almost fivefold, that is, from 1.7 to 8.35 min.

15.3.2 Case Study 2

Flow enters the tanks through an elevated piping inlet through the bottom of each tank carrying a significant amount of momentum as a jet, as displayed in

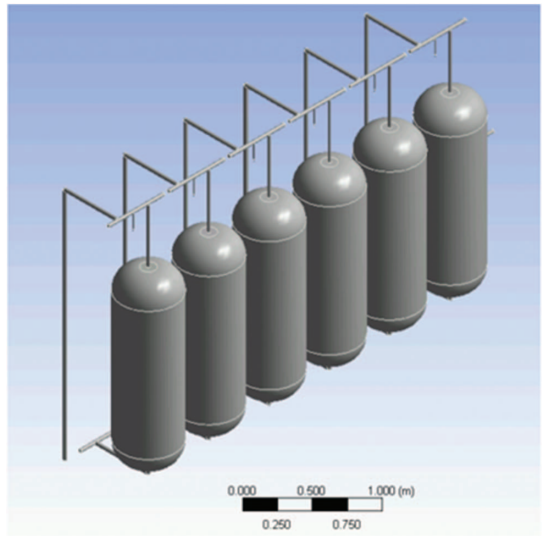

Figure 15-3. Case study 2—Pressurized tank system in series.

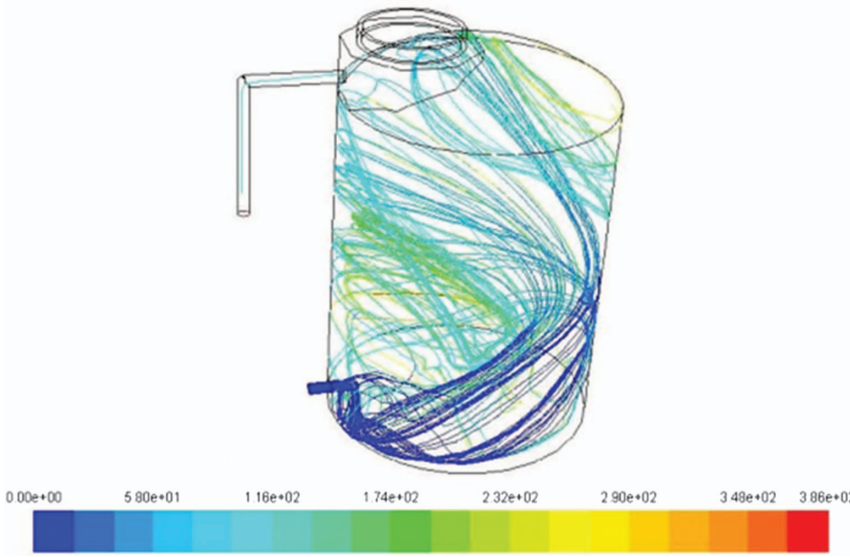

Figure 15-4. Path lines colored by particle time in seconds for unmodified tank operating at 15 gal./min.

Figure 15-7. Whereas a single tank has a baffle factor of only 0.2, each additional tank added in series provides an incremental increase in the total system baffle factor. This increase exhibits a linear trend for up to four tanks in series; the incremental increases in baffle factor decrease for five- and six-tank configurations

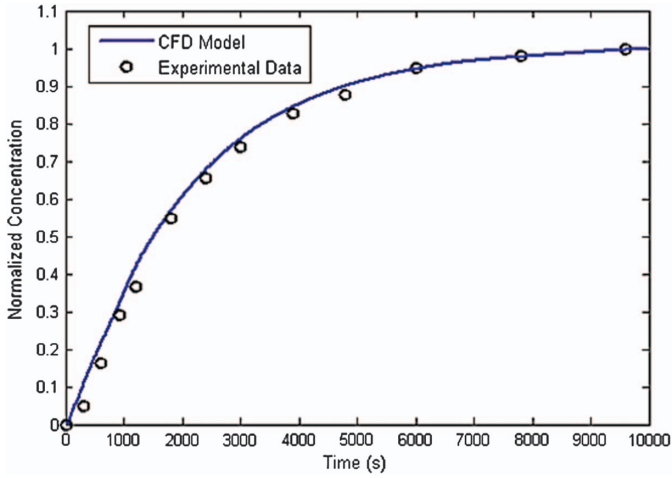

Figure 15-5. RTD curve for unmodified tank operating at 15 gal./min.

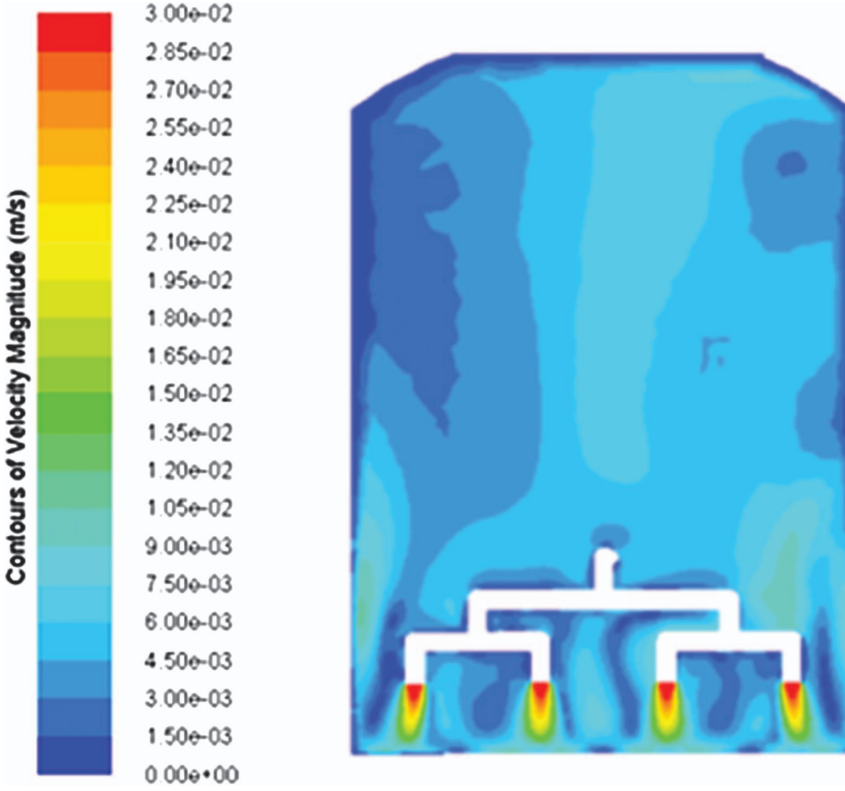

Figure 15-6. Velocity contours (m/s) in a vertical section through the tank for a 16-inlet configuration at 15 gal./min.

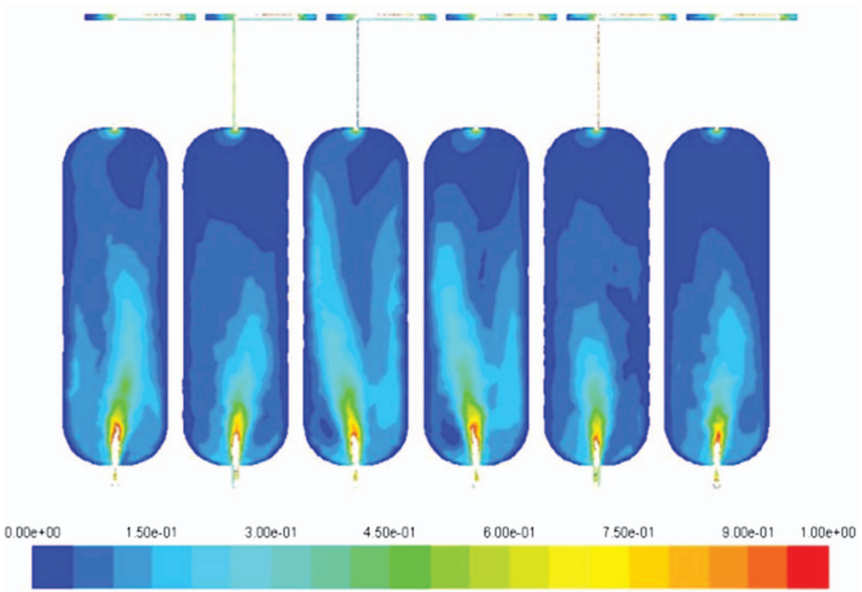

Figure 15-7. Velocity contours (m/s) in a vertical section through the 6-series pressurized tank system.

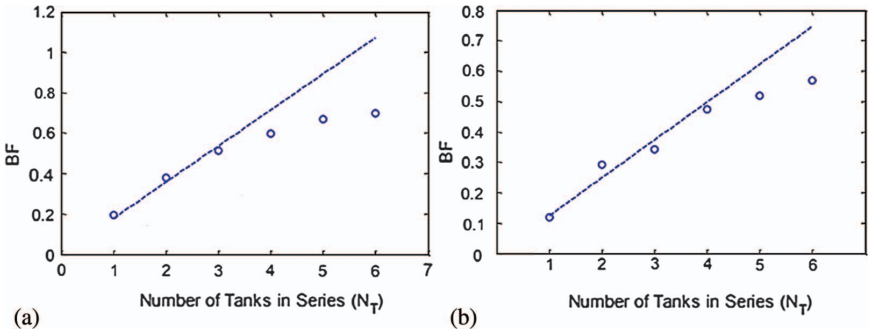

Figure 15-8. Comparison of baffle factor for (a) CFD model and (b) tracer study for pressurized series tank system.

(Wilson and Venayagamoorthy 2010, Wilson 2011). Physical tracer study results of a pilot system compared closely with the CFD model results over the range of tested flow rates, as illustrated in Figure 15-8.

References

CDPHE (Colorado Department of Public Health and Environment). 2014. *Baffling factor guidance manual: Determining disinfection capability and baffling factors for various types of tanks at small public water systems* Accessed April 19, 2019. https://

www.colorado.gov/pacific/sites/default/files/CDPHE%20Baffling%20Factor%20Guidance%20Manual.pdf.

EPA. 2003. *Disinfection profiling and benchmarking technical guidance manual*. Washington, DC: EPA.

EPA. 2011. *National characteristics of drinking water systems: Serving 10, 000 or fewer people*. Washington, DC: EPA.

Taylor, Z. H. 2012. *Towards improved understanding and optimization of the internal hydraulics of chlorine contact tanks*. Fort Collins, CO: Colorado State Univ.

Wilson, J. M. 2011. *Evaluation of flow and scalar transport characteristics of small public drinking water disinfection systems using computational fluid dynamics*. Fort Collins, CO: Colorado State Univ.

Wilson, J. M., and S. K. Venayagamoorthy. 2010. "Evaluation of hydraulic efficiency of disinfection systems based on residence time distribution curves." *Environ. Sci. Technol.* **44** (24): 9377–9382.

Part 4

Wastewater Treatment Technologies and CFD Application Case Studies

This page intentionally left blank

CHAPTER 16
Activated Sludge Tanks

Jie Zhang

16.1 BACKGROUND

Attempts to apply computational fluid dynamics (CFD) to aeration have been made since the 1990s (Karama et al. 1999). Early CFD applications focused on the hydraulics in aeration tanks (Karama et al. 1999; Gujer 2006, Barrio et al. 2015). Recent applications have attempted to directly estimate effluent water quality, such as chemical oxygen demand (COD) and ammonia, by combining CFD with biokinetics models, such as the series of activated sludge models (ASMs) (Le Moullec et al. 2010, Gresch et al. 2011).

This chapter introduces a case study of an activated sludge tank using a CFD-ASM1 model in which CFD and ASM1 are linked by a simplified relationship between dissolved oxygen (DO) concentration and air volume fraction (Yang et al. 2017). ASM1 is one of the ASM models developed by Henze et al. (2001). The CFD-ASM1 model is less computational-intensive than that developed by Le Moullec et al. (2010). A full-scale activated sludge tank operated by the Gaobeidian Wastewater Treatment Plant (WWTP), Beijing, China, was selected for the case study. Details of the simulation are listed in Table 16-1.

16.2 OBJECTIVE

Demonstrate the applicability of the CFD-ASM1 model to an industry-scale activated sludge tank (shown in Figure 16-1).

16.3 RESULTS AND DISCUSSION

The air volume fraction distributions for the cases with the minimum and the maximum airflow rates are shown in Figure 16-2a and b, respectively. Based on

Table 16-1. Information Related to the CFD Simulation

Flow conditions	Items		Reference
	Water treatment unit	A full-scale activated sludge tank operated by the Gaobeidian WWTP, Beijing, China	Yang et al. 2017
	Geometry	Figure 16-1	
	Dimensions	96 m × 7 m × 9.28 m	
	Flow rate	Water: 263 million gal./day Air: 1,620 m^3/min (minimum) 3,600 m^3/min (maximum)	
Model information	Simulation	Method or Governing Equation	Reference
	Type	RANSS with volume of fluid model	Chapter 5
	Flow	Navier-Stokes equations	
	Chemical and biological reaction	ASM1 model	Henze et al. 2001
Software used	Type of software	Name of software	Availability
	Meshing tool	Gambit	Commercial
	Solver	ANSYS Fluent 6.3	Commercial
	Post-processing tool	ANSYS Fluent 6.3	Commercial
Computational information	Items	Remarks	
	Computational grid	Structured, 17,316 cells	
	Computing device equivalent	1 CPU core + 8 G RAM	
	Computing time	~ 1 h	

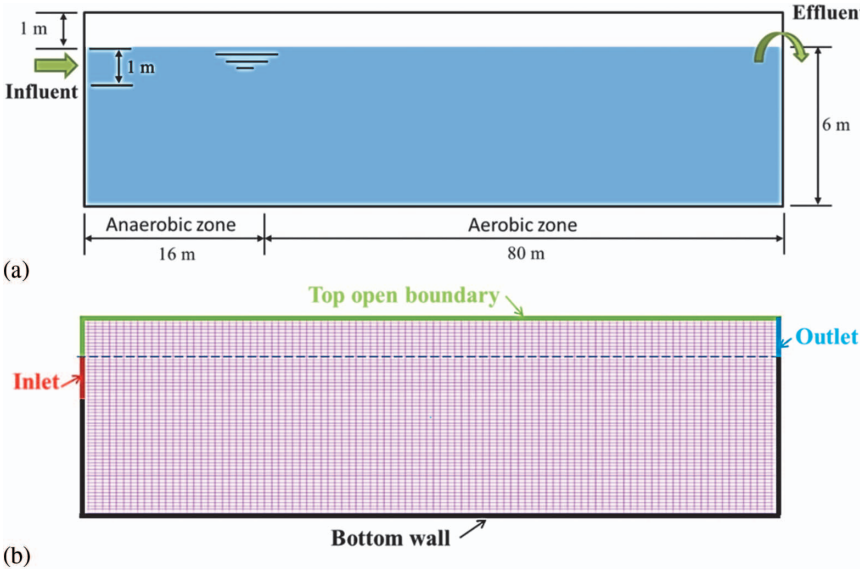

Figure 16-1. (a) Schematic, and (b) computational grid of the activated sludge tank in Gaobeidian WWTP, Beijing, China.
Source: Yang et al. (2017).

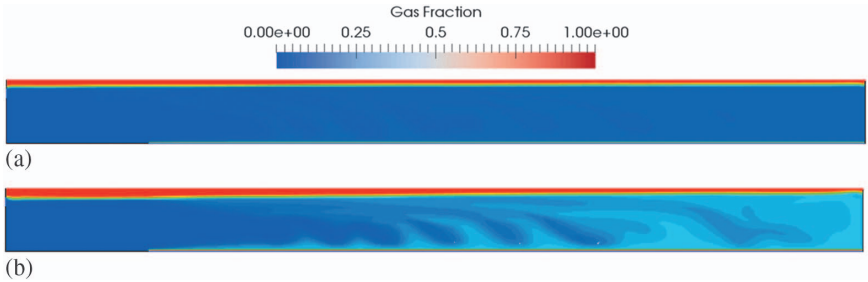

Figure 16-2. Gas fraction contours on the streamwise-vertical plane at midspan of the simulated full-scale ozone contactor. The flow direction is from left to right.
Source: Courtesy of ASCE; reproduced with permission.

the results of CFD simulations, the average air volume fraction for the cases with the minimum and the maximum airflow rates were calculated to be 6.4% and 11.9%, respectively. The DO concentrations for the cases with the minimum and the maximum airflow rates were calculated to be 5.84 and 6.59 mg/L, respectively. The predicted DO concentrations were used as input to the ASM1 for predicting the effluent concentration of COD, NO_3-N, and NH_3-N. The predicted concentrations were compared with measured data, as shown in Table 16-2. The predictions of COD concentrations are close to the measured

Table 16-2. Effluent Water Quality from the CFD-ASM1 and Experiments

	COD			*NO_3-N*			*NH_3-N*		
		CFD-ASM1			*CFD-ASM1*			*CFD-ASM1*	
Month	*Measured*	*DO = C_1*	*DO = C_2*	*Measured*	*DO = C_1*	*DO = C_2*	*Measured*	*DO = C_1*	*DO = C_2*
June	28.1	27.6	27.7	20.0	30.7	30.9	2.3	1.8	1.8
July	31.1	30.51	30.5	24.5	35.6	35.7	0.85	1.3	1.3
August	28.1	27.5	27.5	24.2	26.3	36.4	0.65	1.3	1.3

Source: Yang et al. (2017) Note: Units = mg/L.

data (relative error 1.4–2.2%). The predictions of NO_3-N concentrations are significant to the measured data (relative error 9–55%), and the predictions of NH_3-N concentrations are even worse (relative error 22–100%). The observed discrepancy between the predictions and the measured data of NO_3-N and NH_3-N in this study could be explained by an overestimated DO concentration, which is caused by neglecting the oxygen consumption by microorganisms in the CFD simulation. Although the accuracies of the predictions for NO_3-N and NH_3-N concentrations are relatively low, the CFD-ASM1 performed on par with the full CFD model in Le Moullec et al. (2010). In Le Moullec et al. (2010), the relative errors of the predictions from the full CFD model are around 19% for effluent concentration of COD, 27% for effluent concentration of NO_3-N, and 100% for effluent concentration of NH_3-N. Thus, the CFD-ASM1 developed in this study is still favorable since it has a much lower computational cost compared with the full CFD model (the computational cost of the CFD-ASM1 is estimated to be less than 10% of that of the full CFD model (Moullec et al. 2010)).

Note that for the cases with different airflow rates, the differences in predictions of COD, NO_3-N, and NH_3-N are insignificant. The primary reason is that, as demonstrated by the experiments, when the DO concentration is higher than 1 mg/L, the effluent water quality of the activated sludge tank hardly changes (Du 2010). Thus, we can conclude that DO concentration is insensitive to airflow rate if DO concentration is higher than a certain level (1 mg/L in this case).

References

Barrio, R., E. Blanco, J. Fernández, and M. Galdo. 2015. "The use of computational fluid dynamics to estimate fluid residence time and flow hydrodynamics in open digesters of wastewater treatment plants: A case study." *Desalin. Water Treat.* **53** (10): 2613–2622. Accessed April 19, 2019. https://www.tandfonline.com/doi/ref/10.1080/19443994.2013.868831?scroll=top#metrics-content.

Du, W. 2010. "Numerical simulation of wastewater biological treatment combined ASM1 with CFD." Department of Environmental Engineering, Master thesis, Beihang Univ.

Gresch, M., M. Armbruster, D. Braun, and W. Gujer. 2011. "Effects of aeration patterns on the flow field in wastewater aeration tanks." *Water Res.* **45** (2): 810–818.

Gujer, W. 2006. "Activated sludge modelling: Past, present and future." *Water Sci. Technol.* **53** (3): 111–119.

Henze, M., W. Gujer, T. Mino, and M. van Loosdrecht. 2001. *Activated sludge models ASM1, ASM2, ASM2d and ASM3*. London: IWA Publishing.

Karama, A. B., O. O. Onyejekwe, C. J. Brouckaert, and C. A. Buckley. 1999. "The use of computational fluid dynamics (CFD). Technique for evaluating the efficiency of an activated sludge reactor." *Water Sci. Technol.* **39** (10): 329–332.

Le Moullec, Y., C. Gentric, O. Potier, and J. P. Leclerc. 2010. "CFD simulation of the hydrodynamics and reactions in an activated sludge channel reactor of wastewater treatment." *Chem. Eng. Sci.* **65** (1): 492–498.

Yang, J., W. J. Du, and J. Zhang. 2017. "Rapid analysis of effluent water quality in activated sludge systems using computational fluid dynamics." In *Proc., World Environmental and Water Resources Congress 2017*, 12–23. Reston, VA: ASCE.

APPENDIX: MODELING INSTRUCTIONS

The detailed steps used to create and run the case in ANSYS Fluent are provided here. The ANSYS Fluent version used to set up and run the model is v6.3.

STEPS

1. Generate mesh using Gambit.
2. Import mesh into ANSYS Fluent.
3. Select modules (k-ε turbulence model; multiphase model).
4. Set up boundary and initial conditions.
5. Run the case until the flow solution is convergent.
6. Use the flow solution as the input of the ASM1 model to calculate chemical information.

Note that because of copyright laws, this primer provides the case file for solving flow solution only. Readers may develop the user-defined function (UDF) of the ASM model in ANSYS Fluent based on Henze et al. (2001).

CHAPTER 17

Computational Fluid Dynamics of Waste Stabilization Ponds

Faissal R. Ouedraogo
Jie Zhang
Andrés E. Tejada-Martínez

17.1 BACKGROUND

Waste stabilization ponds (WSPs) are constructed wetlands used throughout the world as wastewater treatment technology. They are economically viable (Mara 2004) and a more sustainable alternative to treatment plants because they offer the potential for agricultural reuse and nutrient recovery for crop growth (Cornejo et al. 2013). WSP systems are typically configured in series where treatments (biological and chemical) are performed with no input of chemicals or energy. The retention or residence time of a system (or a single pond) is the time the water spends in the system (or a single pond) before exiting. In this study, originally performed by Ouedraogo et al. (2016), several sludge accumulation profiles at the bottom of a WSP located in Bolivia are compared to isolate the effect of sludge geometry on the pond retention time and its overall hydraulic performance. Simulation Cases I and II correspond to no sludge and the measured sludge by Lizima (2013), respectively, and Cases III and IV are projected accumulations to 2016 as calculated by Ouedraogo et al. (2016) (Figures 17-1 and 17-2). Cases IIIA and IVA have the same sludge distributions as Cases III and IV, respectively, but greater water surface elevation (Figure 17-2 and Table 17-1). Figure 17-1a and b show the pond model. The pond has a length of 46 m, a width of 23.9 m, and a depth of 1.8 m. The inlet and outlet cross-sectional areas are 0.25 m^2 each. Figure 17-2 displays the sludge profiles considered in the study. Table 17-1 displays the sludge and water volumes and pond surface water elevation for the different scenarios. For brevity, the hydrodynamics of Cases I–IV are discussed in the Results and Discussion. Details of the hydrodynamics of Cases IIIA and IVA can be found in Ouedraogo et al.

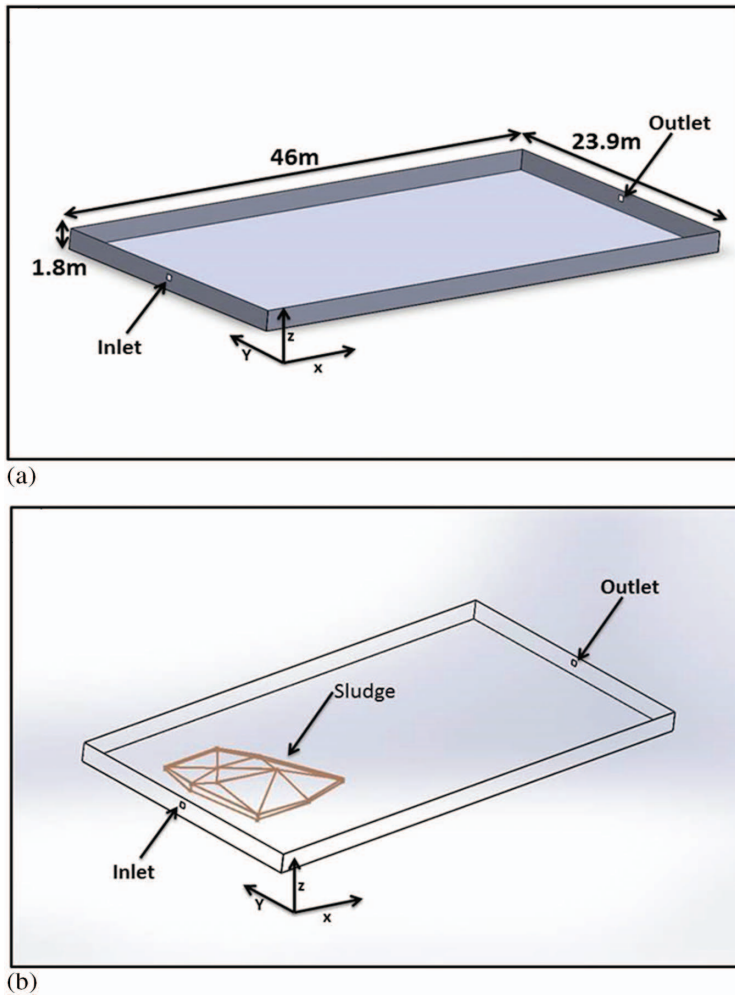

Figure 17-1. (a) Case 1—Pond in 2006 with no sludge. (Case I), and (b) Case II—Computational domain based on sludge profile physically measured in 2012 (Lizima, 2013).
Source: Ouedraogo et al. (2016), reproduced with permission from Elsevier.

(2016). The OpenFOAM files accompanying this chapter correspond to Case II. The details of the simulation are included in Table 17-2.

17.2 OBJECTIVES

- Analyze the flow fields and residence time distribution (RTD) of the WSP.
- Determine the effect of sludge geometry on hydraulic performance.

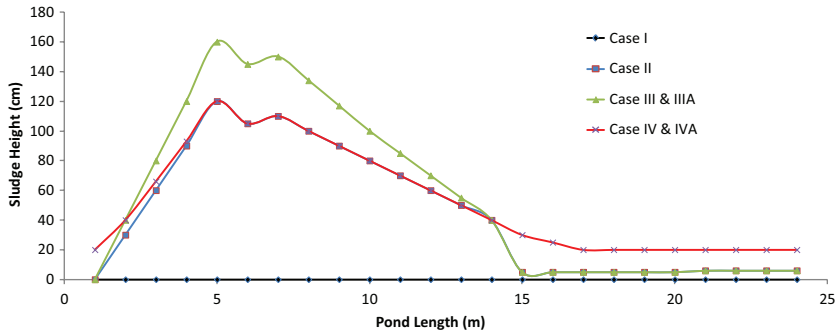

Figure 17-2. Comparison of the sludge profiles on x-z plane (following the coordinate system in Figure 17-1) for Cases I–IV. Case I corresponds to the WSP with no sludge (2006). Case II corresponds to the field measurements of Lizima (2013), and Cases III (IIIA) and IV (IVA) correspond to projected sludge accumulations in 2016.
Source: Ouedraogo et al. (2016), reproduced with permission from Elsevier.

Table 17-1. Water Volumes, Sludge Volumes, and Water Surface Elevations for Cases I–IV, IIIA, and IVA

Cases	*Sludge Volume (m^3)*	*Water Volume (m^3)*	*Water Surface Elevation (m)*
Case I	0	1,979	1.8
Case II	154	1,815	1.8
Case III	326	1,643	1.8
Case IV	326	1,643	1.8
Case IIIA	326	1,815	1.944
Case IVA	326	1,815	1.944

- Determine the effect of pond water level increase on hydraulic performance (described in detail by Ouedraogo et al. 2016).

17.3 RESULTS AND DISCUSSION

Flow: The flow in general for all cases is characterized by a high-speed inlet jet that weakens with distance from the inlet (Figure 17-3). In Cases II–IV at the water surface, the jet has higher velocity than in Case I (no sludge) (panels A–D). This difference is explained by the fact that water velocity is increased while the jet flows over the sludge. At the pond inlet depth (0.69 m), the water jet is obstructed by the sludge, causing the jet to be laterally and vertically diverted (around and over) the sludge (panels E–H). The flow in Case III is mainly diverted laterally

Table 17-2. Information Related to the CFD Simulation

Flow conditions	Items		Reference
	System based on	Single WSP in Bolivia	
	Geometry	Figure 17-1	Ouedraogo et al. (2016)
	Dimensions	46 m × 23.9 m × 1.8 m	
	Flow rate	66 m^3/day	
Model information	Simulation	Method or Governing Equation	Reference
	Type	RANS	
	Flow	N-S equation	
	Tracer	Transport equation for passive scalar	
	CT	Transport equation for CT	
Software used	Type of software	Name of software	Availability
	Meshing tool	Gambit	Commercial
	Solver	OpenFOAM	Free and open source
	Postprocessing tool	ParaView	Free software
Computational information	Items	Remarks	
	Computational grid	Unstructured, ~800,000 cells	
	Computing device equivalent	(4 CPU cores + 8G RAM) × 4	
	Computing time	~48 h	

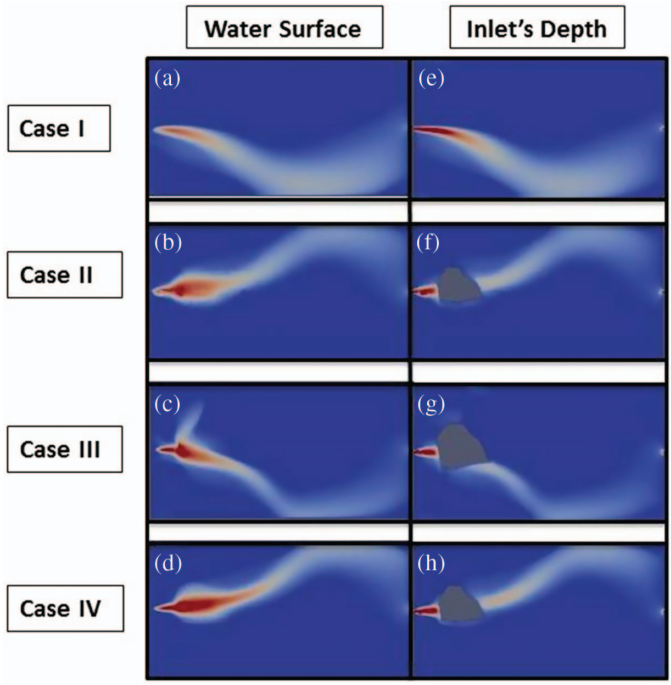

Figure 17-3. Water flow speed contours for Cases I–IV on x-y *(horizontal) planes at depth = 0 m (corresponding to the water surface) and depth = 0.69 m below the water surface (at the depth of the inlet). The sludge accumulation is color-coded gray. The speed range is 0–0.0005 m* s^{-1}.
Source: Ouedraogo et al. (2016), reproduced with permission from Elsevier.

because the sludge peak in that case reaches higher than the peak in Cases II and IV (Figure 17-2). This lateral diversion provides a baffling effect, increasing residence time.

Tracer: The height and location of the first peak of the tracer concentration time series at the outlet is indicative of the level of short-circuiting (Figure 17-4). Cases II and IV have the highest peaks; these cases have the same sludge peak height. Case III has the lowest first tracer peak and thus the weakest short-circuiting. This is caused by the baffling effect, which results from the greater sludge height in this case.

Hydraulic performance: The short-circuiting index ($0 < S < 1$) is a measure of the level of short-circuiting (Ouedraogo et al. 2016). The index is inversely proportional to short-circuiting. As shown in Table 17-3, Case III has the highest short-circuiting index (0.118), indicating that the sludge in that case improved the hydraulic performance of the pond. This result is further confirmed by the mean residence time predicted by computational fluid dynamics (CFD); Case III has the longest residence time (24.86 days).

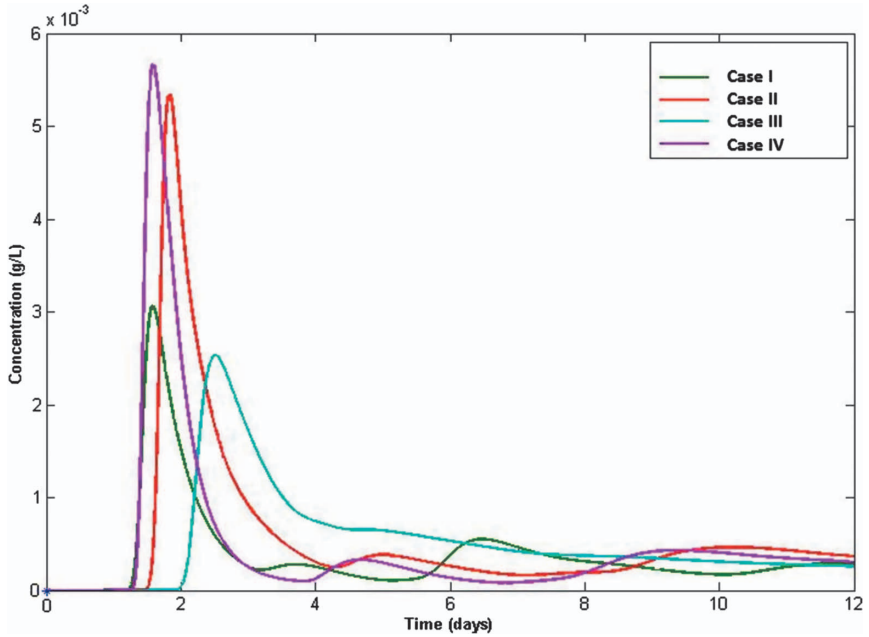

Figure 17-4. Tracer concentration time history.
Source: Ouedraogo et al. (2016), reproduced with permission from Elsevier.

Table 17-3. Comparison of Treatment Efficiency Indexes and Residence Times for Cases I–IV

Cases	S	*Theoretical Residence Time* τ *(days)*	*CFD-Predicted Mean Residence Time* $\bar{\tau}$ *(days)*
Case I	0.089	29.98	22.93
Case II	0.075	27.65	21.89
Case III	0.118	25.04	24.86
Case IV	0.07	25.04	20.36

17.4 CONCLUSION

Sludge accumulation in a WSP has been viewed by many as a negative. This study proved that some sludge geometries can act like baffles and therefore improve the hydraulic performance of the pond. The treatment capacity (volume) of a pond is decreased with sludge buildup, but not necessarily the treatment quality (Ouedraogo et al. 2016).

References

Cornejo, P. K., Q., Zhang, and J. R., Mihelcic. 2013. "Quantifying benefits of resource recovery from sanitation provision in a developing world setting." *J. Environ. Manage.* **131**: 7–15.

Lizima, L. 2013. "Hydraulic evaluation of a community managed wastewater stabilization pond system." Department of Civil and Environmental Engineering, Master's thesis, Univ. of South Florida.

Mara, D. D. 2004. *Domestic wastewater treatment in developing countries*. London: Earthscan Publications.

Ouedraogo, F. R., J., Zhang, P. K., Cornejo, Q., Zhang, J. R., Mihelcic, and A. E., Tejada-Martinez. 2016. "Impact of sludge layer geometry on the hydraulic performance of a waste stabilization pond." *Water Res.* **99**: 253–262.

This page intentionally left blank

CHAPTER 18
Algae Raceway Ponds

Jie Zhang

18.1 BACKGROUND

Algae farming technology is an approach to turn CO_2 and sewage into a valuable commodity through the cultivation of algae. Open ponds such as raceway-type ponds are commonly used commercial configurations for algae farming (Figure 18-1). Raceway ponds usually use channels with constant width and depth, hairpin bends, and one or more paddle wheels to circulate water through the system. In such systems, resistance to water circulation has two distinct parts: the straight sections and the hairpin bends (Green et al. 1995, Borowitzka 2005). Most of the energy loss occurs at the hairpin bends. A few modifications have been developed to minimize this energy loss, such as multiple-vane flow rectifiers (H. Shimamatsu and Y. Tominaga, US Patent No. 4,217,728 (1980), Shimamatsu 1987) and eccentric curved walls with baffles (Dodd 1986).

The objective of this case study is to demonstrate that computational fluid dynamics (CFD) can be used to evaluate the current raceway pond designs and produce new designs, which may reduce the energy loss in raceway ponds and thereby create more efficient algal growth systems. In this chapter, two raceway configurations, original and modified (by adding turning vanes at the hairpin bends) as shown in Figure 18-2, were studied using CFD. Details of the simulations are listed in Table 18-1.

18.2 RESULTS AND DISCUSSION

Figure 18-3 shows the distribution of relative pressure. Note that the pressure at the outlet (the front of the paddle wheel) is set to zero and the relative pressure shown here is divided by the density of water. Thus, to calculate the pressure drop from the inlet (the back of the paddle wheel) to the outlet, this formula should be used:

$$\Delta P = P_{\text{in}} - P_{\text{out}} \tag{18-1}$$

Figure 18-1. Typical raceway-type algae ponds (left) for pilot testing and (right) for full-scale biomass production or wastewater treatment facilities.
Source: Courtesy of MicroBio Engineering Inc., reproduced with permission.

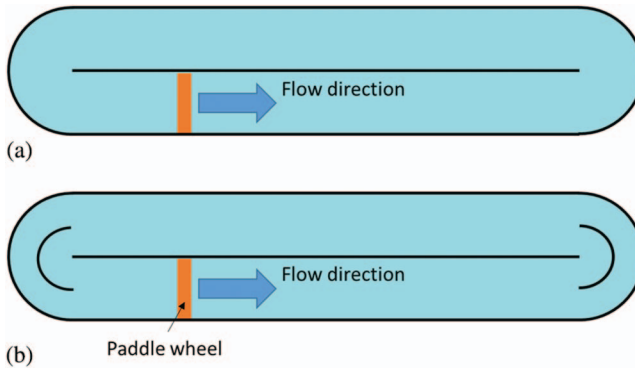

Figure 18-2. Schematics of (a) original and (b) modified algae raceway pond.

where ΔP is the pressure drop, P_{in} and P_{out} are pressures at the inlet and the outlet, respectively.

The power consumption, W_{cons}, is computed using this formula (Liffman et al. 2013):

$$W_{cons} = A\Delta P \times 0.3\ \mathrm{m/s} \tag{18-2}$$

where A is the cross-sectional area.

The pressure drops and power consumption of the two designs were calculated and listed in Table 18-2. The power consumption of the original design is 125 Watt, which is consistent with the result (i.e., 120 Watt) from Liffman et al. (2013). The power consumption of the modified design is 56 Watt, which is 55% lower than the original one.

The flow velocity uniformity could be the reason for reducing the power consumption. Figures 18-4 and 18-5 show the flow speed contours and streamlines, respectively, at the surface of the two designs. A relatively strong high-speed

Table 18-1. Information Related to the CFD Simulation

Flow conditions	Items		Reference
	System based on	A 96-m long raceway with a cross section of 4.9 m × 0.3 m (1.47 m^2), and a mean velocity of 0.3 m/s	Liffman et al. 2013
	Geometry	Figure 18-2	
	Dimensions	96 m × 4.9 m × 0.3 m	
	Average velocity	0.3 m/s	
Model information	Simulation	Method or Governing Equation	Reference
	Type	RANS	Chapter 5
	Flow	N-S equation	Chapter 1
	Turbulence model	Standard k-ε model	
	Boundary conditions	Inlet: velocity inlet (fixed 0.3 m/s) Outlet: pressure outlet	
Software used	Type of software	Name of software	Availability
	Meshing tool	Gambit	Commercial
	Solver	OpenFOAM	Open source
	Postprocessing tool	OpenFOAM	Open source
Computational information	Items	Remarks	
	Computational grid	Unstructured, 18,594 cells	
	Computing device equivalent	1 CPU core + 8G RAM	
	Computing time	~10 min	

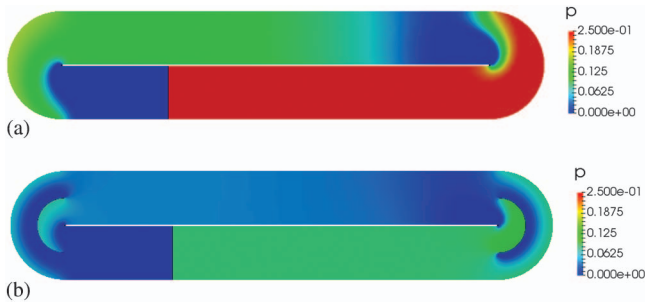

Figure 18.3. Relative pressure distribution.

Table 18-2. Pressure Loss of One Cycle and the Required Power of Paddle Wheel

	ΔP	W_{cons}
Original	284 Pascal	125 Watt
Modified	127 Pascal	56 Watt

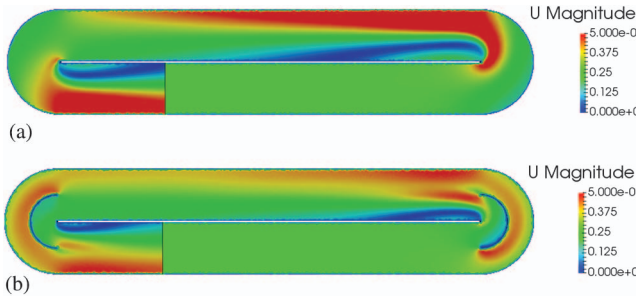

Figure 18-4. Speed contour at water surface.

flow can be found at the hairpin bends of the original design because of the separation of flow over the center wall. The flow became more uniform once the turning vane was added (Figure 18-4b). From the streamlines in Figure 18-5, dead zones can be observed (the region near the center wall in which no streamline is seen). The size of the dead zone in the original design is apparently larger than that in the modified design, indicating that more energy is consumed in the original design.

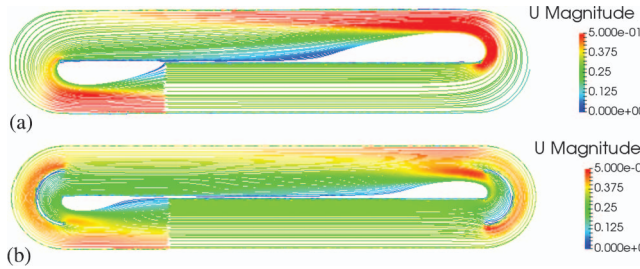

Figure 18-5. Streamline at water surface.

References

Borowitzka, M. A. 2005. "Culturing microalgae in outdoor ponds." In *Algal culturing techniques*, 205–218. Amsterdam, Netherlands: Academic Press.

Dodd, J. C. 1986. "Elements of pond design and construction." In *Handbook of microalgal mass cultures*, 265–84. Boca Raton, FL: CRC Press.

Green, F. B., T. J. Lundquist, and W. J. Oswald. 1995. "Energetics of advanced integrated wastewater pond systems." *Water Sci. Technol.* **31** (12): 9–20.

Liffman, K., D. A. Paterson, P. Liovic, and P. Bandopadhayay. 2013. "Comparing the energy efficiency of different high rate algal raceway pond designs using computational fluid dynamics." *Chem. Eng. Res. Des.* **91** (2): 221–226.

OpenCFD Ltd. 2010. "OpenFOAM user guide version 1.7.1." Accessed May 04, 2015. http://www.openfoam.com/docs/user/.

Shimamatsu, H. 1987. "A pond for edible Spirulina production and its hydraulic studies." *Hydrobiologia* **151** (1): 83–89.

APPENDIX: MODELING INSTRUCTIONS

The detailed steps to create and run the case in OpenFOAM are provided here. Before starting the case, it is recommended that the user become familiar with the basic directory structure in OpenFOAM, which contains the minimum set of files required to run an application. The reader is encouraged to read carefully Section 4.1 of the *OpenFOAM Users Guide* (2010). Ensure that OpenFOAM is properly installed in your machine. The OpenFOAM version used to set up and run the model is v2.2.

STEPS

1. Generate mesh using OpenFOAM utility blockMesh, or snappyHexMesh, or commercial software (e.g., Gambit, Gridgen).

2. Optional: Convert the mesh into OpenFOAM format if it came from another software.
3. Ensure that the boundary names in the files of initial variables (in folder "0") are consistent with those in the "boundary" file in /constant/polymesh/.
4. Modify the control parameters (endTime, timeStep; writeInterval) in /system/controlDict.
5. Run the case by using the command (the name of the solver defined in the /system/controlDict) in the Linux command window.

CHAPTER 19
UV Disinfection

Subbu-Srikanth Pathapati
Ed Wicklein

19.1 BACKGROUND

Disinfection using ultraviolet (UV) radiation has gained favor in the past few decades, primarily because of the advantage of generating little to no harmful by-products. The efficiency of a UV reactor is linked to several factors, such as flow distribution, fluence rate field, microbial inactivation kinetics, and thus, optimal reactor geometry. This chapter focuses on using computational fluid dynamics (CFD) to model the flow field, fluence rate, and effluent log inactivation of the geometry of a simple UV reactor. Results indicate the importance of choosing the correct turbulence model and show good agreement of the predicted flow field with particle image velocimetry (PIV) data. Results also indicate good agreement of predicted log inactivation with measured bioassay data. The overall modeling method is summarized in Table 19-1.

19.2 PROBLEM DESCRIPTION

UV radiation is a widely accepted technology for disinfection. It is particularly advantageous in that no harmful by-products, such as trihalomethanes (THMs), typically formed by other processes such as chlorination, are created as a result. UV is also more effective against protozoan pathogens, which are less sensitive to chlorine. The disadvantage of UV disinfection largely stems from the cost involved in comparison to chlorination, particularly for large-scale applications. However, the technology is cost-competitive when chlorination-dechlorination is used (Solomon et al. 1998).

The performance of a UV reactor is directly related to optimal reactor geometry—one that promotes good flow distribution. This chapter describes CFD modeling of a UV reactor to determine the flow field, fluence rate field, and microbial inactivation, including effects of wall reflection (Chen et al. 2011).

To optimize disinfection using UV, an integrated model was developed that includes flow field modeling, fluence rate modeling, and microbial inactivation

Table 19-1. Information Related to the CFD Simulation

Flow conditions	Items		Reference
	System based on	A pilot scale UV reactor	Chen et al. (2011)
	Geometry	Figures 19-1 and 19-2	
	Dimensions	The total length and diameter of the pipe were 3 m and 0.315 m, respectively. The interior of the pipe was 0.477 m	
	Flow velocity	0.83 m/s	
Model information	Simulation	Method or Governing Equation	Reference
	Type	RANS	Chapter 5
	Flow	N-S equation	Chapter 1
	Radiation	P-1	
	Biological inactivation	Chick-Watson user-defined function	
Software used	Type of software	ANSYS Fluent 6.2/18.2	Commercial
	Meshing tool	Gambit/ANSYS mesher	Commercial
	Solver	ANSYS Fluent 6.2/18.2	Commercial
	Postprocessing tool	ANSYS Fluent 6.2/18.2	Commercial
Computational information	Items	Remarks	
	Computational grid	Unstructured, 1.4 million cells	
	Computing device equivalent	4 CPU cores, Intel Xeon, 16 GB RAM	
	Computing time	8–12 h per simulation	

modeling. The reactor consisted of UV lamps set in a specific configuration in a simple closed conduit. The flow velocity through the pipe was 0.83 m/s. The goals of the CFD model were to predict fluence rate, to determine the appropriate turbulence model for flow modeling, and to predict microbial inactivation. Flow modeling results and microbial inactivation were compared to experimental data.

19.3 MODEL DESCRIPTION

Figure 19-1a and b depicts the geometry of the simple closed conduit reactor. The total length and diameter of the pipe were 3 m and 0.315 m, respectively. The interior of the 0.477-m long reactor with four cylindrical lamps and three cleaning rods is shown in Figure 19-2. The lamps had a diameter of 0.039 m, and the three cleaning rods had diameters of 0.023, 0.016, and 0.023 m. Rods used for cleaning fouling were assumed to be stationary for modeling purposes. Only half of the reactor was modeled, using a symmetry boundary condition. The final grid consisted of an unstructured mesh made of 1.41 million tetrahedral cells, with local refinement. Figures 19-3 and 19-4 depict the mesh.

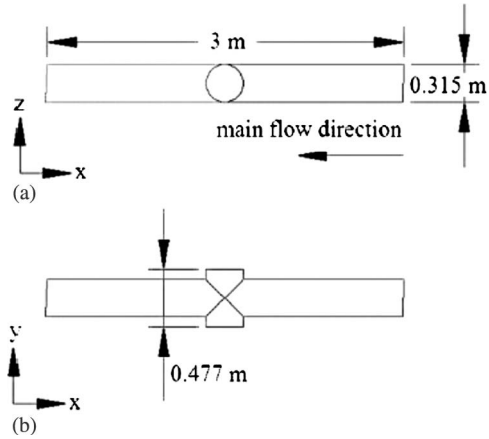

Figure 19-1. Model geometry: (a) side view, and (b) plan view.

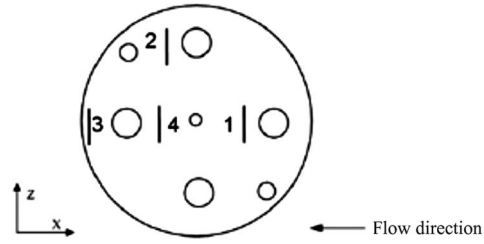

Figure 19-2. Layout of UV lamps and cleaning rods.

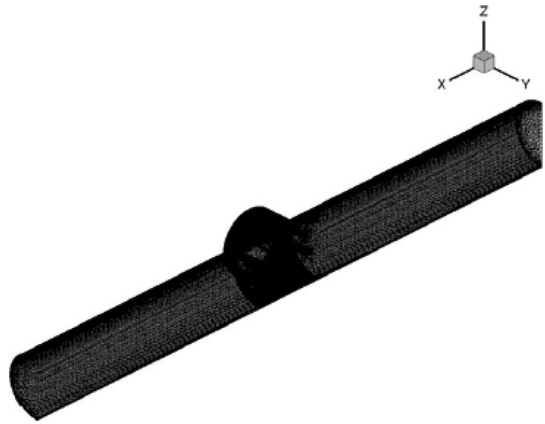

Figure 19-3. Overall unstructured mesh of the UV reactor.

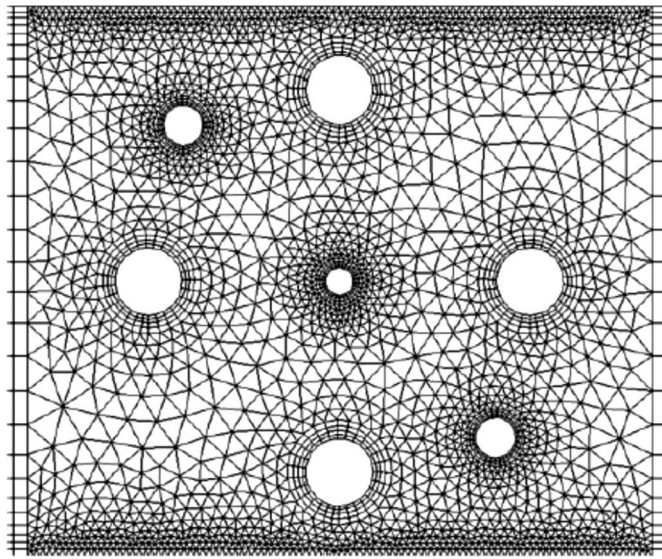

Figure 19-4. Cross section of the mesh showing local refinement.

The 3D CFD model was implemented in ANSYS Fluent 6.3. A low Reynolds number k-ε model (Abe et al. 1994) was used for turbulence modeling. A modified P-1 radiation model was used to predict the fluence rate, and scattering effects were assumed to be negligible. Any UV radiation transmission inside the lamps was not modeled; only the transmission of UV in the water was modeled. A user-defined function was utilized to set boundary conditions for fluence rate. At all opaque or diffusively reflecting surfaces, the value of reflectivity was set as a function of the emissivity. At all nonreflecting surfaces, emissivity was set to a

value of 1. A mass-weighted Eulerian disinfection model (Ducoste et al. 2005) was used to model microbial inactivation. The source term in the disinfection model describes the inactivation of microbes; the first-order Chick-Watson model was utilized by means of a user-defined function. Solution methods included the SIMPLE algorithm for pressure–velocity coupling, second-order upwinding for momentum equations, and the central difference scheme for all diffusion terms. Iterative convergence limits were set at 1×10^{-4} and 1×10^{-5} for continuity and momentum equations, respectively; convergence limits for fluence rate and concentrations were set at 1×10^{-7}.

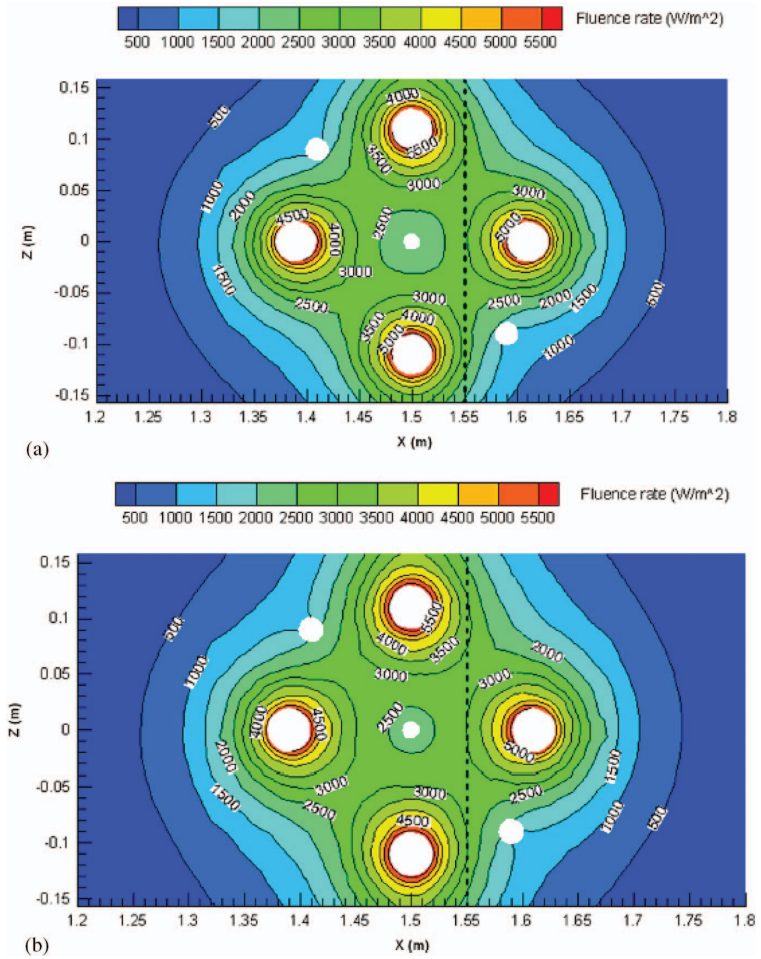

Figure 19-5. Contours of fluence rate distribution along a central plane. Plot (a) depicts results with wall reflectivity r = 0, and plot (b) depicts results with r = 0.2.

19.4 RESULTS AND DISCUSSION

The results of this work show the effects of wall reflection on fluence rate and concentration distribution.

Figure 19-5 depicts the distribution of a fluence rate as a function of a reflectivity, in particular, the distribution of fluence rate along a cross-sectional

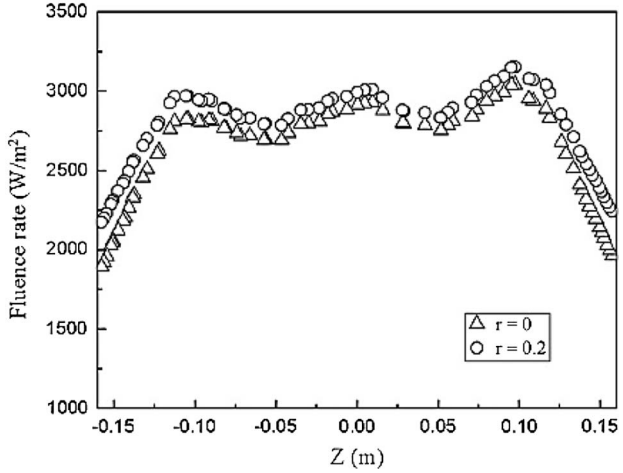

Figure 19-6. Fluence rate along representative line x as a function of wall reflectivity.

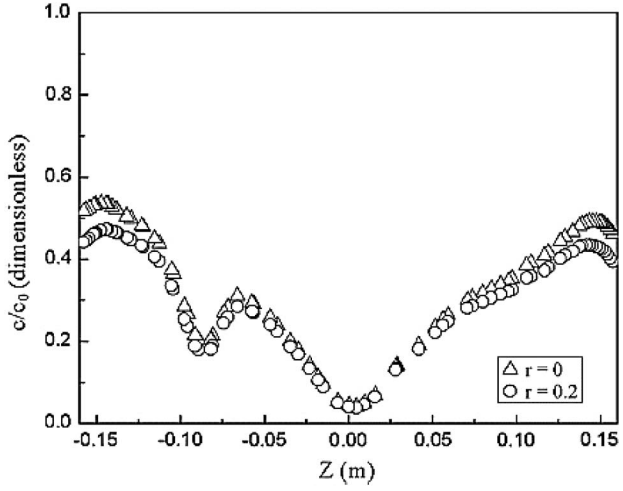

Figure 19-7. Microbial concentration along representative line x as a function of wall reflectivity.

plane along the width of the lamp enclosure. There was an overall increase in fluence rate close to the walls, with increase in reflectivity from $r = 0$ in plot (a) to $r = 0.2$ in plot (b). Figures 19-6 and 19-7 depict the fluence rate and concentration of microorganisms along a representative line in the domain. There is a direct indication of lower microbial concentration in regions with increased fluence rate.

References

Abe, K., T. Kondoh, and Y. Nagano. 1994. "A new turbulence model for predicting fluid-flow and heat-transfer in separating and reattaching flows. I: Flow-field calculations." *Int. J. Heat Mass Trans.* **37** (1): 139–151.

Chen, J., B. Deng and C. N. Kim. 2011. "Computational fluid dynamics (CFD) modeling of UV disinfection in a closed-conduit reactor." *Chem. Eng. Sci.* **66** (21): 4983–4990.

Ducoste, J. J., D. Liu, and K. Linden. 2005. "Alternative approaches to modeling fluence distribution and microbial inactivation in ultraviolet reactors: Lagrangian versus Eulerian." *J. Environ. Eng.* **131** (10): 1393–1403.

Solomon, C., P. Casey, C. Mackne, and A. Lake. 1998. *Ultraviolet disinfection fact sheet*. Morgantown, WV: Environment Technology Institute, West Virginia Univ.

APPENDIX: MODELING INSTRUCTIONS

The detailed steps to create and run the case in ANSYS Fluent are provided as follows.

1. Generate mesh using ANSYS Workbench and export a mesh file compatible with Fluent.
2. Open mesh with Fluent.
3. Choose "Viscous" from the "Models" pane and set to standard *k*-epsilon.
   a. Manually change *k*-epsilon model constants to low Reynolds number constants.
4. Enable radiation model and choose P-1 model.
5. Choose material "water-liquid" from "Materials" panel.
6. Enable user-defined scalar from "Define" tab. Select one scalar.
7. Set "cell zone" to water-liquid.
8. In cell zone, check "source terms" and choose user-defined function for user scalar. Read in function describing Chick's law.
9. Set boundary conditions to velocity inlet and pressure outlet.
   a. Set velocity and concentration gradients to zero at the outlet.
   b. Set turbulent intensity and length scale.
   c. Set appropriate value for user define scalar flux

10. At all flow walls, choose the "no-slip" boundary condition. At all reflective walls, click on the "thermal" tab, select "radiation" and set emissivity by reading in user-defined function. At nonreflective walls, set emissivity to zero. At lamps, select "thermal" tab, "radiation," and set heat generation rate.
11. Choose solution method "SIMPLE" and set spatial discretization methods.
    a. Use "Least Squares Cell Based for Gradient."
    b. Use PRESTO for pressure.
    c. Set momentum, turbulent kinetic energy, and dissipation rate to second-order upwind.
12. Set underrelaxation factors for pressure to 0.2, momentum to 0.5, k and epsilon to 0.5 to start. These numbers will need to be adjusted as the solution proceeds to aid convergence.
13. Initialize the solution.
14. Run the calculation until appropriate residuals are reached for continuity, momentum, fluence rated, and user-defined scalar concentration.

Part 5

Stormwater Treatment Technologies and CFD Application Case Studies

This page intentionally left blank

CHAPTER 20
Stormwater Collection

Yovanni A. Cataño-Lopera

20.1 BACKGROUND

A detention pond is a particular collection stormwater treatment technology primarily designed to store and purify polluted waters. Other stormwater collection devices are pipes, cisterns, in- or on-line storage tanks, and rain gardens. Detention ponds provide general flood protection during extreme rainfall events in areas where newly developed, impervious surfaces generate excess runoffs. The rate at which flow exits the pond is limited by using a control device that maintains the predevelopment flow rate. The volume of the permanent pool is set by a desired residence time to allow microbes and vegetation in the water to consume nutrients and to allow suspended pollutants to settle while enhancing outflow water quality.

Computational fluid dynamics (CFD) has been established as a common tool for stormwater pond design and evaluation (Khan et al. 2012). Kuoyi et al. (2010) used CFD to study the flow structure in a large stormwater pond. Albers and Amell (2010) used CFD modeling to investigate the discharge characteristics of traditional stormwater pond designs against a new pond design termed the Nautilus Pond. The simulation results showed that the traditional pond design is prone to short-circuiting flow during a significant storm. The Nautilus Pond, on the other hand, has shown to be less prone to short-circuiting while better approximating plug flow behavior.

20.2 OBJECTIVES

The objectives of this experiment include the following:

- Analyze the flow field patterns in the pond and verify the reduction of hydraulic short-circuiting in order to maximize the outflow water quality,
- Compare inflow and outflow hydrographs, and
- Evaluate zones prone to sediment and/or pollutant deposition.

20.3 PROBLEM DESCRIPTION

Although stormwater inflows have a highly transient nature, the key features of the Nautilus Pond are designed to passively enable the development of a spiral flow pattern without mechanical intervention. The modular design of the Nautilus Pond is better suited for constrained or discontinuous sites, where traditional designs are particularly susceptible to short-circuiting and dead zone formation.

20.4 MODEL DESCRIPTION

Herein, OpenFOAM is used to implement the CFD model of the flow hydrodynamics in the pond. The model solves for turbulent flow with a shear stress transport (SST) k-ε turbulence closure scheme and uses a body-fitted mesh consisting of hexahedral elements.

20.5 MODEL GEOMETRY

Figure 20-1 shows the schematics of a slightly modified version of the Nautilus Pond proposed by Albers and Amell (2010). Table 20-1 lists the dimensions of the Pond along information associated to the CFD Simulation. The pond is designed to temporarily collect and treat storm flows generated under heavy rainfall events. The rain-generated inflow hydrograph is input through a short canal with bottom elevation of 1.5 m on the southwest of the pond; the width of the inlet canal is 3.5 m. At x = 40 m, the bottom of the inlet canal drops to an elevation of −0.8 m, matching the elevation of the bottom of the pond. The flow is conducted along a canal toward the north side of the pond. The inflow canal is separated from the interior of the pond by a guiding wall with a top elevation of 2.0 m, and the exterior boundaries of the pond are walls with a top elevation of 4.0 m. The resident water elevation is set at z = 1.5 m, and the total volume of the pond is approximately 14,000 m^3. The flow exits the pond through an orifice 0.7 m in diameter located at the center of the pond. The outflow is then conducted toward the north end of the pond through a pipe that is also 0.7 m in diameter running under the pond.

20.6 RESULTS AND DISCUSSION

Figure 20-2 shows vectors of free-surface velocity magnitude of inflowing stormwater in the pond at t = 850 s. The orientation of the velocity vectors around the

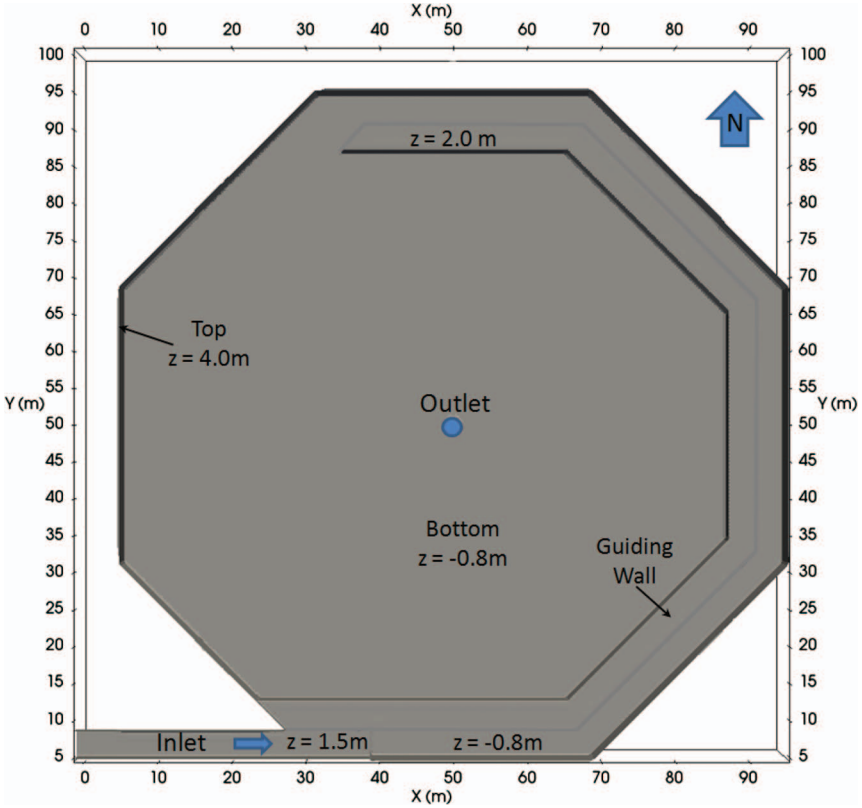

Figure 20-1. Plan view of the pond configuration.

outlet demonstrates the spiral flow pattern induced by the shape of the pond. The flow pattern increases the stormwater treatment efficiency by providing generally longer retention times when compared to typical designs of equivalent footprint areas. Furthermore, the spiral flow pattern minimizes the formation of recirculation zones, which negatively affect water treatment efficiency. The entire pond volume is effectively flushed from the perimeter toward the central outlet.

The simulated inflow and outflow hydrographs are plotted in Figure 20-3. Note the oscillation in the outflow hydrograph, induced by local flow turbulence, and instabilities induced by the passage of the peak of the inflow hydrograph. The shape and size of the pond are directly responsible for a substantial hydraulic flow attenuation because peak inflow, 8 m^3/s, is more than four times the outflow, about 1.8 m^3/s. The inflow and outflow hydrographs reach maxima at $t = 216$ min and about $t = 650$ min, respectively. The outflow decays at a much lower rate than the inflow and reaches zero (not shown) long after the inflow has ceased.

Zones prone to pollutant and/or sediment accumulation in the pond can be evaluated by plotting the magnitude of the wall shear stress (τ_ω) distribution at

Table 20-1. Information Related to the CFD Simulation

Flow conditions	Items		Reference
	System based on	A full-scale Nautilus detention pond	
	Geometry	Figure 20-1	
	Dimensions	96 m × 91 m × 8.4 m	
	Flow rate	Inflow: 0 to 8 m^3/s	
Model information	Simulation	Method or Governing Equation	Reference
	Type	RANSS	Chapter 5
	Flow	N-S equations	Chapter 1
Software used	Type of software	Name of software	Availability
	Meshing tool	blockMesh and snappyHexMesh	Free and open source
	Solver	OpenFOAM v4.x	Free and open source
	Postprocessing tool	ParaView	Free software
Boundary conditions	Boundary	Description	
	Inlet	Variable flow rate described by an inflow hydrograph resulting from an intense storm event with a total duration of about 45 min applied across the bottom area of the inlet, representing the water phase. The upper region of the inlet was set as air with 0 inlet velocity, and 0 static pressure (representing atmospheric conditions)	
	Walls	Interior walls of the pond and the drainpipe were modeled as no-slip boundary conditions with a high-Reynolds rough wall function. No fluid was allowed to pass through the walls. A roughness height corresponding to concrete was used as wall material	

	Top of domain	Atmospheric boundary condition was set at the top of the pond. Air or water can freely leave the domain with zero gradients
	Outlet	A continuative boundary condition with zero static pressure and zero head boundary condition was set at the outlet face

Computational information	Items	Description
	Computational grid	Boundary fitted, unstructured with 144,000 cells Cell size range: 0.001 m^2 to 1.9 m^2
	Computing device equivalent	(6 CPU cores + 32 GB RAM)
	Computing time	~30 h

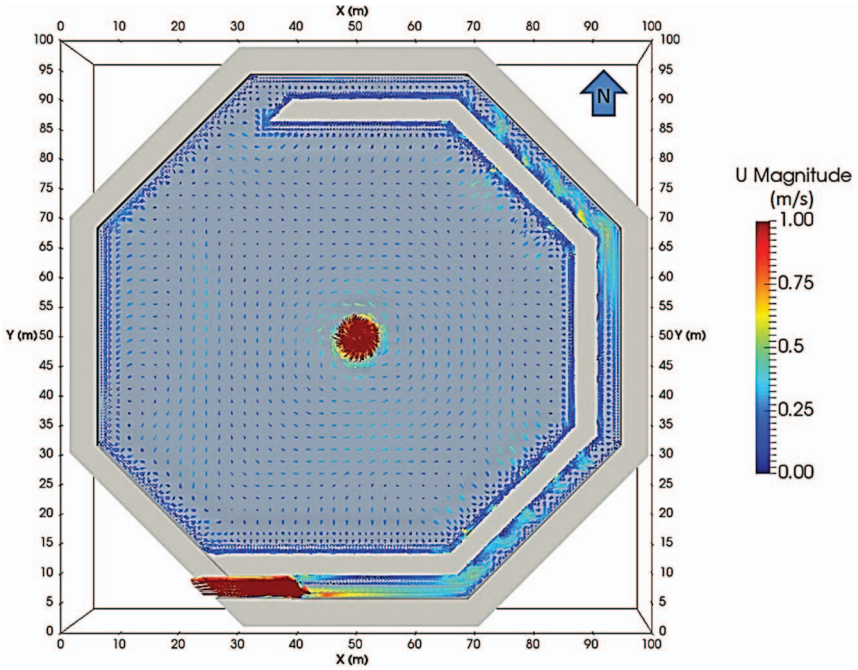

Figure 20-2. Vectors of surface velocity magnitude at t = *850 s.*

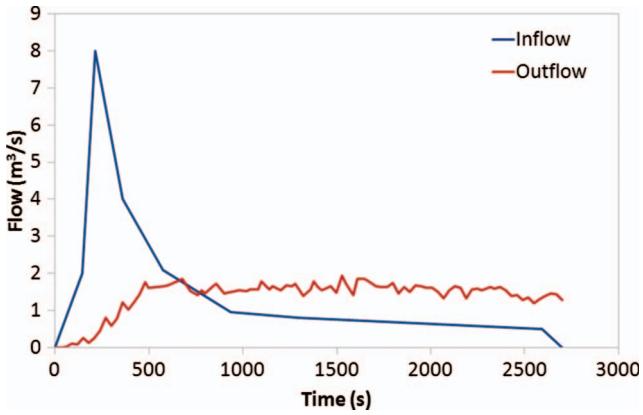

Figure 20-3. Inflow and simulated outflow hydrographs.

different times. For example, Figure 20-4 shows simulated wall shear stress magnitude distribution at time t = 2,760 s. Sediment and/or pollutants tend to accumulate in the regions of lower shear stresses (darker blue), such as at the interior of the 45-degree wall corners, and are concentrically arranged in the vicinity of the outlet orifice.

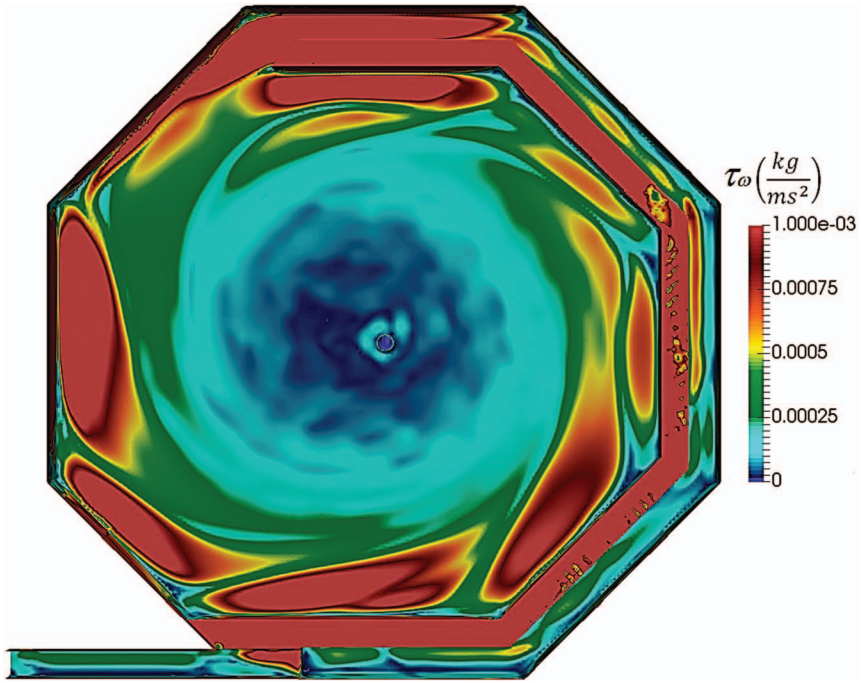

Figure 20-4. Simulated wall shear stress magnitude distribution at t = *2,760 s.*

References

Albers, C., and B. Amell. 2010. "Changing the stormwater pond design game." [In French.] In *Proc., 7th Int. Conf. on Sustainable Techniques and Strategies in Urban Water Management*, Session 3.5, pp 1–10, GRAIE, Lyon, France. Accessed October 19, 2018. http://documents.irevues.inist.fr/handle/2042/35816.

Khan, S., B. W. Melville, A. Y. Shamseldin, and C. Fisher. 2013. "Investigation of flow patterns in storm water retention ponds using CFD." *J. Environ. Eng.* **139** (1): 61–69.

Kuoyi, G. L., L. Arias, S. Barraud, and J.-L. Bertrand-Krajewski. 2010. "CFD modeling of flows in a large stormwater detention and settling pond." [In French.] In *Proc., 7th Int. Conf. on Sustainable Techniques and Strategies in Urban Water Management NOVA-TECH*, Session 3.5, pp 1–10. GRAIE, Lyon, France. Accessed April 19, 2019. http://documents.irevues.inist.fr/bitstream/handle/2042/35753/23503-162LIP.pdf?s..

OpenFOAM. 2016. "The open source CFD toolbox: User guide, v4.x." December 2016. OpenFOAM Foundation. Accessed April 19, 2019. https:openfoam.org.

APPENDIX: MODELING INSTRUCTIONS

The detailed steps used to create and run the case in OpenFOAM are provided as follows. Before starting the case, it is recommended that the user become familiar

with the basic directory structure in OpenFOAM, which contains the minimum set of files required to run an application. The reader is encouraged to read carefully Section 4.1 of the *OpenFOAM User Guide* (2016). Ensure that OpenFOAM is properly installed in your machine. The OpenFOAM version used to set up and run the model is v4.x.

STEPS

1. Generate the mesh, using OpenFOAM utility blockMesh or snappyHexMesh, or any other software (e.g., Gambit or Gridgen);
2. Optional: Convert the mesh into OpenFOAM format if results came from another software;
3. Make the boundary names in the files of initial variables (in folder "0") consistent with those in the "boundary" file in /constant/polyMesh/;
4. Modify the control parameters (e.g., endTime, timeStep, and writeInterval) in /system/controlDict;
5. Run the case by using the solver and/or application specified in /system/controlDict, in the Linux command window.

CHAPTER 21
Stormwater Filtration

Subbu-Srikanth Pathapati

21.1 BACKGROUND

Stormwater runoff carries with it an entrained mixture of particulates that range from large-diameter sediments to dissolved constituents. Filtration using granular media is a treatment option, particularly useful for removal of fine particulates and associated nutrients. The packed granular media has two functions: removal of particulates and associated adsorbed nutrients (e.g., phosphorus) and aiding removal of dissolved constituents by prolonging residence time of influent in the system, thereby increasing contact between metal oxide coating and dissolved nutrients.

Filtration with granular media occurs via one or more of the following mechanisms: surficial straining, sedimentation, interception, inertial impaction, diffusion, and hydrodynamic and electrostatic interaction (Wakeman and Tarleton 2005). The objective of this chapter is to demonstrate that computational fluid dynamics (CFD) modeling can be used to simulate flows through filter media and to predict particle removal by the filter media and containment system. The overall modeling method is summarized in Table 21-1.

21.2 PROBLEM DESCRIPTION

Although stormwater flows and pollutant loadings have a highly transient nature, this chapter focuses on modeling specified steady flow rates with loading of predetermined steady influent particulate matter. The pilot-scale radial cartridge filter (RCF) system has a volume of approximately 73 L and is packed with media coated with aluminum oxide. The media are enclosed in a cylindrical container and are held together by a tightly wound coarse screen, as depicted in Figure 21-1. Flow enters radially through the circumference, passes through the porous media, enters a perforated pipe located in the center, and exits the system through the bottom. The goal of the CFD model is to predict particulate matter removal and

Table 21-1. Information Related to the CFD Simulation

Flow conditions	Items		Reference
	System based on	A pilot-scale radial cartridge media filter	Pathapati and Sansalone 2009
	Geometry	Figure 21-1	
	Dimensions	Total volume of 73 L, cylindrical filter cartridge diameter of 0.45 m, height of 0.56 m	
	Flow rate	9–90 L/min	
Model information	Simulation	Method or Governing Equation	Reference
	Type	RANS	Chapter 5
	Flow	N-S equation	Chapter 1
	Porous media	Inertial and viscous resistance coefficients	
	Particle tracking	Discrete phase model	
Software used	Type of software	ANSYS Fluent 6.2/18.2	Commercial
	Meshing tool	Gambit/ANSYS mesher	Commercial
	Solver	ANSYS Fluent 6.2/18.2	Commercial
	Postprocessing tool	ANSYS Fluent 6.2/18.2	Commercial
Computational information	Items		Remarks
	Computational grid	Unstructured, 3.1 million cells	
	Computing device equivalent	4 CPU cores, Intel Xeon, 16 GB RAM	
	Computing time	8–12 h per simulation	

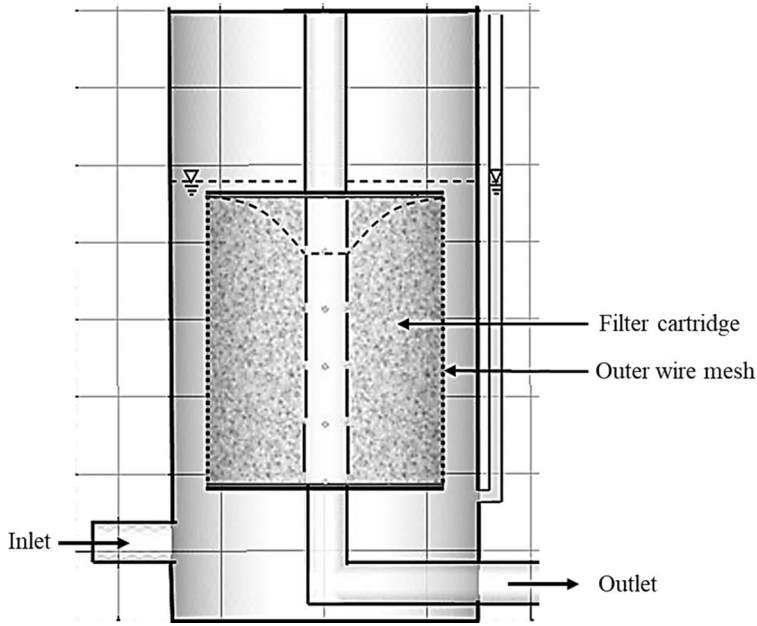

Figure 21-1. Geometry of filtration system.

head loss by the filtration system and to compare it to experimentally measured data for a clean filter bed. Filter clogging was not modeled.

21.3 MODEL DESCRIPTION

The model geometry is described as follows. The total volume of RCF was 73 L, and the additional volume of the test tank around the RCF was approximately 57 L to the top. The diameter and height of the RCF were 0.4572 m and 0.5588 m, respectively. The media were contained between an outer mesh and impervious polypropylene caps on the top and bottom of the cartridge. The flow path through the cartridge filter is through the outer screen followed by the filter media, into the central perforated pipe, and out through a downflow pipe. The testing schematic is shown in Figure 21-2.

The 3D CFD model was implemented in ANSYS Fluent. A standard k-ε model was used for turbulence modeling. A microscopic approach is impractical and often unnecessary, unless the goal is to investigate localized physical and chemical processes. The filter was thus modeled with a lumped, macroscopic approach-this was achieved by adding a momentum sink term, which was used to model viscous and inertial losses due to the porous media (assumed to be isotropic) and

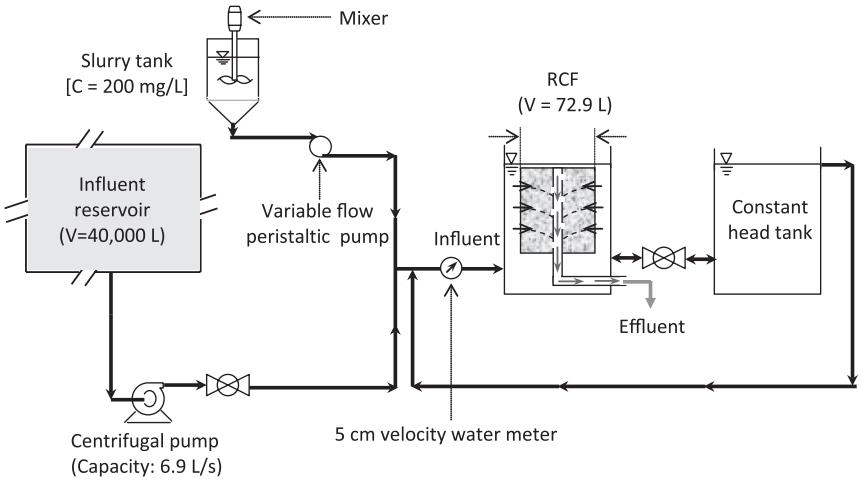

Figure 21-2. Testing schematic and geometry of single radial cartridge filter.
Source: Pathapati and Sansalone (2009).

effective porosity. The dominant flow regime is laminar to transitional in the RCF. The suggested method is to calibrate to one measured pressure loss data point and to validate across the rest of the data.

The Ergun equation (Ergun 1952), an extension of Blake-Plummer and Carman-Kozeny for turbulent flows in filter media, was used to derive macroscopic constants and is expressed as follows:

$$\frac{|\Delta p|}{L} = \frac{150\mu}{d_m^2}\frac{(1-\eta)^2}{\eta^3}v_s + \frac{1.75\rho}{d_m}\frac{(1-\eta)}{\eta^3}v_s^2 \tag{21-1}$$

where

Δp = Pressure drop across the media,
L = Length of the packed bed,
μ = Fluid viscosity,
d_m = Media particle diameter,
η = Total porosity of the packed bed,
ν = Superficial velocity through the packed bed, and
ρ = Fluid density.

The viscous resistance term α and the inertial resistance term C_2 are expressed as follows:

$$\alpha = \frac{d_m^2}{150}\frac{\eta^3}{(1-\eta)^2} \tag{21-2}$$

$$C_2 = \frac{3.5}{d_m}\frac{(1-\eta)}{\eta^3} \tag{21-3}$$

The actual values of α and C_2, though they have physical significance, require calibration within each model. The suggested method is to calibrate to one measured pressure loss data point and to validate across the rest of the data.

The Lagrangian discrete phase model (DPM) for particle tracking is derived from force balances based on classical Newton's (turbulent and transitional regimes) and Stokes (laminar regimes) laws describing particle motion. Particles

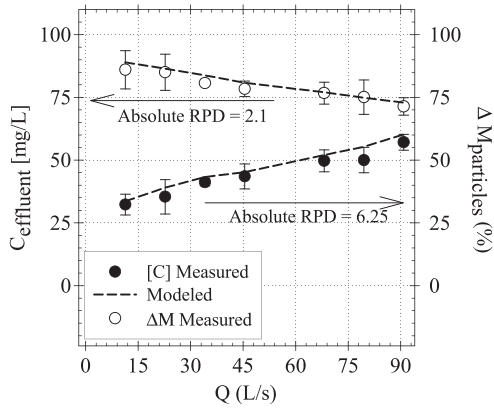

Figure 21-3. Comparison of measured versus modeled results as a function of Q *([L^3T^{-1}]) for noncohesive sandy silt influent particle gradation. RPD stands for relative percent difference between measured and modeled data.*
Source: Pathapati and Sansalone (2009).

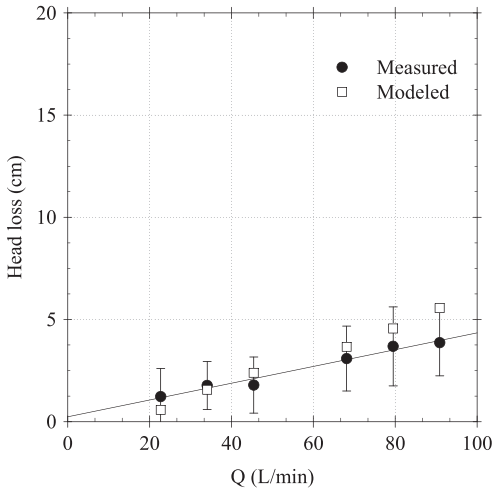

*Figure 21-4. Comparison of measured versus modeled filter head loss (*ΔH*) as a function of influent flow rate (*Q*).*
Source: Pathapati and Sansalone (2009).

were tracked for a specific length for each flow rate, based on hydraulic residence times calculated by injecting neutrally buoyant submicron tracer particles. Particles that remained in the RCF after integrating over the specified length were considered to have been separated or removed by the RCF.

21.4 RESULTS AND DISCUSSION

Grid independence was achieved at a mesh size of 3.01 million cells. CFD predictions of particle removal efficiency on the basis of effluent concentration, as well as effluent mass load are depicted in Figure 21-3. Measured and modeled head loss is presented

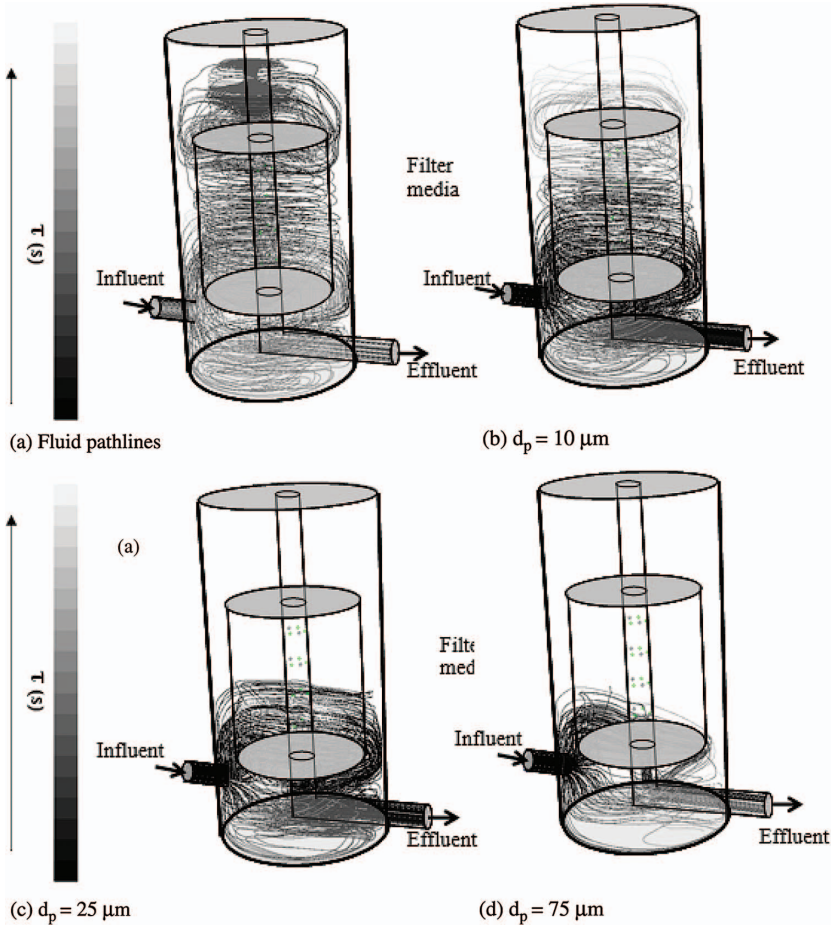

Fig. 21-5. CFD predictions of trajectories of fluid and particles inside the RCF, shaded on the basis of residence time, τ.
Source: Pathapati and Sansalone (2009).

in Figure 21-4. The difference between modeled and measured results is quantified using the absolute relative percent difference, expressed as follows:

$$\text{Absolute RPD} = \left| \frac{(\text{Measured data} - \text{Modeled data})}{\text{Measured data}} \right| \times 100 \qquad (21\text{-}4)$$

A Lagrangian DPM approach was used to track inert spherical silica particles in the filter. Results from particle tracking are depicted in Figure 21-5 and visually show a nonuniform loading as a function of particle diameter. The implication of this finding is that even in a completely submerged, pressurized filtration system, the surface area available for adsorption, particularly for finer particles and their associated chemical contaminants, requires careful evauluation in order to ensure that the target removal efficiencies are achieved.

References

Ergun, S. 1952. "Fluid flow through packed columns." *Chem. Eng. Prog.* **48** (2): 89–94.

Pathapati, S., and J. Sansalone. 2009. "CFD modeling of particulate matter fate and pressure drop in a stormwater radial filter." *J. Environ. Eng.* **135** (2): 77–85.

Wakeman, R., and S. Tarleton. 2005. *Solid/liquid separation: Principles of industrial filtration*. 1st ed., 38–43. Oxford, UK: Elsevier.

APPENDIX: MODELING INSTRUCTIONS

The detailed steps to create and run a simplified case study in ANSYS Fluent are provided here:

1. Generate mesh using ANSYS Workbench or Gambit and export a mesh file compatible with Fluent.
2. Open mesh with Fluent.
3. In the "General" pane, turn on gravity in the appropriate direction and set the value.
4. Choose "Viscous" from the "Models" pane and set to standard *k*-epsilon.
5. Choose material "water-liquid" from "Materials" pane.
6. Set "cell zone" to water-liquid.
7. Select "porous" in "cell zone." Set appropriate values of inertial and viscous resistance coefficients in *x*, *y*, and *z* directions.
8. Set boundary conditions to mass flow inlet and pressure outlet.
9. Choose solution method "SIMPLE."
    a. Set spatial discretization methods.
        i. Use Least Squares Cell Based for Gradient.

ii. Use PRESTO for pressure.

iii. Set momentum, turbulent kinetic energy, and dissipation rate to second-order upwind.

10. Set underrelaxation factors for pressure to 0.2, momentum to 0.5, k and epsilon to 0.5 to start. These values need to be adjusted as the solution proceeds to aid convergence.
11. Initialize the solution and set the monitors at inlet and outlet to monitor the mass flow rate difference.
12. Run the calculation until residuals of at least1×10^{-3} are reached.
13. In the "Models" panel, select Discrete Phase.
    a. Specify "maximum number of steps" and "length scale."
    b. Set injections.
        i. Choose material (repeat step 5 and create new inert material "sand" with the specific gravity 2.65 g/cm^3.
        ii. Select surface injection and choose inlet as surface.
        iii. Set the particle diameter.
        iv. Set the particle mass flow rate.
14. In the "Results" panel, select "Particle Tracks." Choose the injection and track particles. Particles that do not escape the domain are considered to be removed by the filtration system.

CHAPTER 22
Stormwater Separation

Subbu-Srikanth Pathapati

22.1 BACKGROUND

Stormwater runoff is difficult to treat, particularly because of variable hydraulic and particulate loads. The treatment of stormwater runoff with retention and/or detention ponds often proves difficult because of prohibitive land and infrastructure requirements. Several small-footprint devices have emerged in the past two decades for control of particulate pollution from stormwater runoff. These devices, broadly classified as hydrodynamic separators (HSs), typically function by using centrifugal and inertial separation, thus elongating particulate trajectories per unit surface area, and are particularly suited for removal of particle sizes ranging from coarse (>75 μm) to settleable (25–75 μm) particles.

The objective of this chapter is to demonstrate that computational fluid dynamic (CFD) modeling can be used to simulate particle-laden flows through hydrodynamic separators. The overall modeling method is summarized in Table 22-1.

22.2 PROBLEM DESCRIPTION

Although stormwater flows and pollutant loadings have a highly transient nature, this chapter focuses on modeling steady flow and steady particulate loads through a screened hydrodynamic separator (SHS). As shown in Figure 22-1, the SHS consists of two concentric cylindrical chambers separated by a static screen. The flow inlet is tangential to the inner cylindrical chamber. The static screen consists of a regular array of apertures that allows vortexing flow to exit the inner screen chamber and enter the outer volute chamber. The inner cylindrical chamber, along with the screen and the sump chamber, are designated the *screen area*. The outer, less turbulent annular area is termed the *volute area*. Particle separation by this HS configuration is primarily a function of the discrete particle settling velocity, particle diameter, volumetric flow rates, hydraulic residence time, and diameter of the screen apertures. Type I settling is assumed in this case: dilute, nonflocculent, and free settling. (Tchobanoglous et al. 2002).

Table 22-1. Information Related to the CFD Simulation

Flow conditions	Items		Reference
	System based on	Field-scale screened hydrodynamic separator	Pathapati and Sansalone 2009
	Geometry	Fig. 21.1	
	Dimensions	Total volume of 1,580 L, cylinder with diameter of 1.524 m, height of 1.82 m	
	Flow rate	1.5–19.9 L/s	
Model information	Simulation	Method or Governing Equation	Reference
	Type	RANS	Chapter 5
	Flow	N-S equation	Chapter 1
	Porous screen	Inertial and viscous resistance coefficients	
	Particle tracking	Discrete phase model	
Software used	Type of software	ANSYS Fluent 6.2/18.2	Commercial
	Meshing tool	Gambit/ANSYS mesher	Commercial
	Solver	ANSYS Fluent 6.2/18.2	Commercial
	Postprocessing tool	ANSYS Fluent 6.2/18.2	Commercial
Computational information	Items	Remarks	
	Computational grid	Unstructured, 1.96 million cells	
	Computing device equivalent	4 CPU cores, Intel Xeon, 16 GB RAM	
	Computing time	8–12 h per simulation	

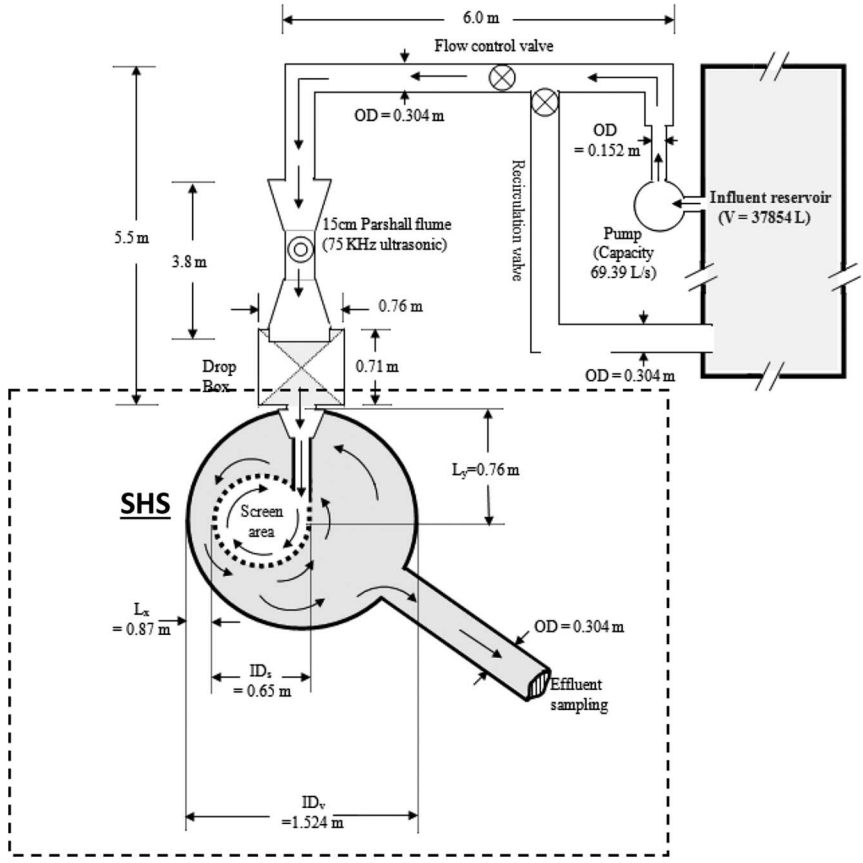

Figure 22-1. Plan view and approximate geometry of experimental testing setup for the SHS.
Source: Pathapati and Sansalone (2009).

The goal of the CFD model is to predict particulate matter removal by the SHS and to compare it to experimentally measured data to ascertain if a CFD approach is indeed capable of producing reasonable and realistic results. The model was then used to investigate the hydrodynamic profile and particle velocities in order to note their deviation, if any, from those predicted by Newton and Stokes laws.

22.3 MODEL DESCRIPTION

Figure 22-1 illustrates the schematic plan view and geometry of the experimental setup for testing the SHS. The overall diameter of the HS is 1.524 m, and the diameter of the inner screened area is 0.65 m. The height of the unit is 1.82 m. The empty HS sump storage volume is approximately 1,580 L. The design hydraulic

operating volumetric flow rate (Q_d) is 15.89 L/s. The static cross-flow screen consists of 2.4 mm-diameter apertures. A known and constant gradation of influent particles is injected immediately upstream of the SHS.

The 3D CFD model was implemented in ANSYS Fluent. The dominant flow regime is fully turbulent in the SHS from the calculated value of the Reynolds number. The standard k-ε turbulence model (Launder and Spalding 1974) was used to predict turbulence intensity in the HS. Its use follows previous studies with hydrocyclones (Nowakowski et al. 2004, Statie et al. 2001, Petty and Parks 2001). The screen was modeled via a momentum sink in the form of a porous zone. The pressure drop through the screen was measured experimentally with pressure transducers, and it was found that the head loss was less than 150 mm, even at higher flow rates, across the static screen (aperture diameter = 2.4 mm). Therefore, the viscous resistance term was assumed to be negligible and the source term was then modeled considering only the inertial resistance term; the inertial resistance factor per unit thickness of the plate was calculated for the x, y, and z directions. The Lagrangian discrete phase model (DPM) was used to predict removal efficiency as a function of particle diameter.

The DPM for particle tracking is derived from force balances based on classical Newton's (turbulent and transitional regimes) and Stokes (laminar regimes) laws describing particle motion.

Once the flow simulation is completed, particles are injected from specified surfaces in the domain; in this case, particles were injected uniformly across the inlet of the SHS. The DPM predicts the trajectory of particles of specified diameter and specific gravity in the SHS based on the solved flow field. The calculation of the particle trajectory depends on the length scale and the number of steps tracked.

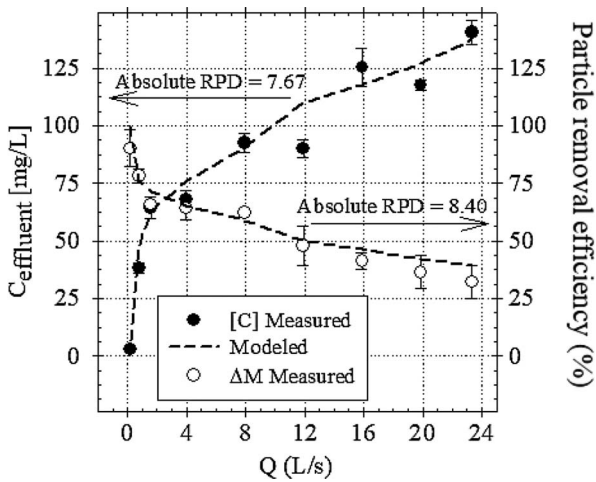

Figure 22-2. Comparison of measured versus modeled results as a function of influent flow rate.
Source: Pathapati and Sansalone (2009).

The length scale is the distance the particle travels before the equations of motion are solved again and the trajectory is updated. The length scale should be as small as possible for good accuracy—a length scale close to the individual cell size is suggested. Particles that exit the SHS after the tracking process are considered to have *escaped* and therefore not removed by the SHS. Particles that remain in the SHS after the tracking process are considered *incomplete* or not removed by the SHS. The number of steps that the particles are tracked for is adjusted until there is no change in the results for the number of particles that escape or are incomplete. A good starting point for the total tracking length is to determine the number of steps it takes for neutrally buoyant tracer particles to pass through the SHS. This is done by injecting particles with the same density as water and tracking them across the SHS. The user can repeat this process for different particle diameters separately or inject a particle size distribution at the inlet.

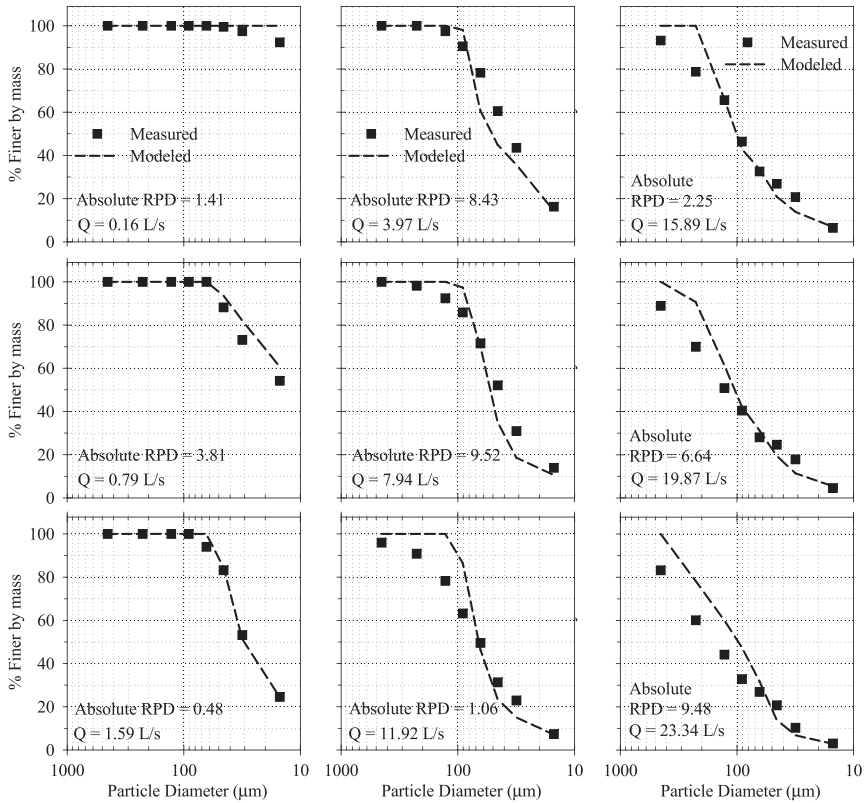

Figure 22-3. Measured versus modeled particle separation by the HS expressed as percent finer by mass as a function of flow rate, at an influent concentration of 200 mg/L.

Source: Pathapati and Sansalone (2009).

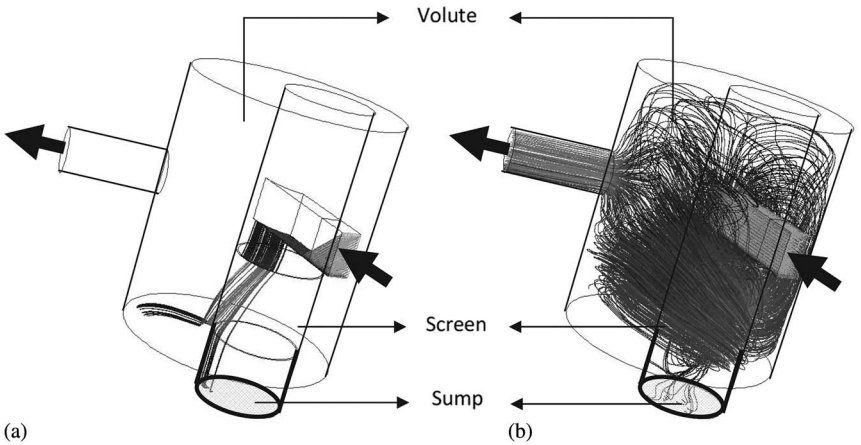

Figure 22-4. Particle trajectories inside the screened HS. Plot (a) depicts particle trajectories for a particle with a diameter (d_p) of 450 μm. Plot (b) depicts particle trajectories for a particle with a d_p of 25 μm
Source: Pathapati and Sansalone (2009).

22.4 RESULTS AND DISCUSSION

CFD predictions of particle removal efficiency on the basis of effluent concentration, as well as effluent mass load, are depicted in Figure 22-2. A comparison of measured and modeled effluent particle size distributions is depicted in Figure 22-3.

The difference between modeled and measured results is quantified using the absolute relative percent difference, expressed as follows:

$$\text{Absolute RPD} = \left| \frac{(\text{Measured data} - \text{Modeled data})}{\text{Measured data}} \right| \times 100 \qquad (22\text{-}1)$$

CFD model results are in close agreement with measured overall particle removal efficiency. In addition, the CFD model predicts particle separation behavior effectively across the entire particle size distribution. The reader may refer to Pathapati and Sansalone (2009) for detailed explanation of the results.

Figure 22-4 illustrates predicted particle trajectories within the screened HS as a function of particle diameter.

References

Launder, B. E., and D. B. Spalding. 1974. "The numerical computation of turbulent flows." *Comput. Method. Appl. Math.* **3** (2): 269–289.

Nowakowski, A. F., J. C. Cullivan, R. A. Williams, and T. Dyakowski. 2004. "Application of CFD to modeling of the flow in hydrocyclones—Is this a realizable option or still a research challenge?" *Miner. Eng.* **17** (5): 661–669.

Pathapati, S., and J. Sansalone. 2009. "CFD Modeling of a stormwater hydrodynamic separator." *J. Environ. Eng.* **135** (4): 191–202.
Petty, C. A., and S. M. Parks. 2001. "Flow predictions within hydrocyclones." *Filtr. Sep.* **38** (6): 28–34.
Statie, E. C., M. E. Salcudean, and I. S. Gartshore. 2001. "The influence of hydrocyclone geometry on separation and fibre classification." *Filtr. Sep.* **38** (6): 36–41.
Tchobanoglous, G., F. L. Burton, and H. D. Stensel. 2002. *Wastewater engineering: Treatment, disposal, and reuse*. 4th ed. New York: McGraw Hill.

APPENDIX: MODELING INSTRUCTIONS

The detailed steps to create and run a simplified case study in ANSYS Fluent are provided here:

1. Generate mesh using ANSYS Workbench or Gambit and export a mesh file compatible with Fluent.
2. Open mesh with Fluent.
3. In the "General" pane, turn on gravity in the appropriate direction and set value.
4. Choose "Viscous" from the "Models" pane and set to standard k-epsilon.
5. Choose "Water-liquid" from "Materials" pane.
6. Set "Cell zone" to "Water-liquid."
7. Select "Porous" in "Cell Zone." Set appropriate values of inertial and viscous resistance coefficients in x, y, and z directions for the porous screen.
8. Set boundary conditions to mass flow inlet and pressure outlet.
9. Set interfaces between porous screen cell zone, inner cylinder, and outer cylinder as interior faces.
10. Choose solution method "SIMPLE."
    a. Set spatial discretization methods.
        i. Use Least Squares Cell Based for Gradient.
        ii. Use PRESTO for pressure.
        iii. Set momentum, turbulent kinetic energy, and dissipation rate to second-order upwind.
11. Set underrelaxation factors for pressure to 0.2, momentum to 0.5, k and epsilon to 0.5 to start. These values need to be adjusted as the solution proceeds to aid convergence.
12. Initialize solution and set monitors at inlet and outlet to monitor mass flow rate difference.
13. Run calculation until residuals of 1×10^{-3} are reached.

14. In the "Models" panel, select "Discrete Phase."
    a. Specify maximum number of steps and length scale.
    b. Set injections.
        i. Choose material (repeat step 5, create new inert material "sand" with specific gravity 2.65 g/cm^3.
        ii. Select surface injection and choose inlet as the surface.
        iii. Set particle diameter.
        iv. Set particle mass flow rate.
15. In the "Results" panel, select "Particle Tracks." Choose the injection and track particles. Particles that do not escape the domain are considered to be removed by the hydrodynamic separator.

CHAPTER 23

Geysering

Biao Huang
Jue Wang
Jose Vasconcelos

23.1 INTRODUCTION

Intense rain events can create conditions for the transition between free-surface and pressurized flow regimes in a stormwater drainage network. As inflows in closed conduits become pressurized, a variety of processes can lead to the formation of entrapped air pockets (Li and McCorquodale 1999, Vasconcelos and Wright 2006). As entrapped air pockets are formed and travel within sewers and tunnel reaches, these pockets may undergo surging (Zhou et al. 2002, Vasconcelos and Leite 2012), or they may be suddenly released through water-filled vertical shafts. The water displacement created by the rise of large air pockets may lead to geyser events in stormwater systems (Vasconcelos and Wright 2011, Wright et al. 2011, Muller et al. 2017, Huang 2017). Whereas a single-phase mass oscillation in vertical shafts can also trigger geysering (Guo and Song 1991), the magnitude of these events is much more severe when these discharges are associated with two-phase flows.

Because of its large geometric complexity and the required computational times, it is still not feasible to use computational fluid dynamics (CFD) to represent the whole stormwater system during rapid filling conditions. Rather, one-dimensional (1D) formulations based on mass and momentum equations are often applied to simulate flows in stormwater systems (Song et al. 1983, Vasconcelos et al. 2006, Leon et al. 2006, Politano et al. 2007). Such models can be useful in determining whether transition to pressurized flows can exist and whether air pockets can appear between ventilation points. These models can also be useful in determining if the vertical displacement of air in vertical shafts can lead to damaging pressures (Klaver et al. 2016). Fewer 1D models, however, can account for air phase in its formulation; they are exemplified by Vasconcelos and Wright (2003, 2009) and Leon et al. (2010).

Such 1D models can provide useful data (e.g., initial conditions) to be used in CFD models to represent flow conditions in sewers before the release of air pockets. Yet there are limited studies involving geysers, both in terms of physical

and numerical modeling. CFD modeling, with free-surface tracking algorithms such as the volume of fluid (VoF) method (Hirt and Nichols 1981), can help estimate the displacement of water within vertical towers. This outcome is important because it could help determine the geometric changes in hydraulic structures that could mitigate geysering issues. Moreover, CFD can also determine fractions of air that are not eliminated in a vertical shaft and could become an issue in a subsequent vertical structure.

23.2 STRUCTURE AND OBJECTIVES

This chapter is structured around two different examples, illustrating how CFD tools can provide insights regarding geysering processes created by the uncontrolled release of air pockets. The first simulation example, performed with ANSYS CFX, uses the two-dimensional (2D) domain and focuses on the release of a relatively large fraction of air through a small-diameter and short vertical tower. The study objectives are to assess the two-phase, vertical flows associated with geysering processes, compute vertical displacements, and analyze pressure oscillations in this process.

The second example studies the effect of multiple air pocket releases through water-filled shafts. The study was performed with OpenFOAM in a three-dimensional (3D) domain. This study's goal was to compare the differences of geysering events between a single, large air pocket being released versus a sequence of smaller pockets with spatial separation. Both examples used Reynolds-averaged Navier-Stokes equations, two-equation turbulent models, and the VoF method.

23.3 FIRST GEYSERING SIMULATION

The simulations were conducted using ANSYS CFX v 18.0 in the High Performance Computing Center of Zhengzhou University. The homogeneous two-phase model using the VoF method was adopted in the present study, which solves a single set of momentum equations and tracks the volume fraction of each fluid throughout the domain. The shear stress transport (SST) k-ω turbulence model used here is a robust two-equation eddy-viscosity model that combines the strength of the k-ω and k-ε models (Table 23-1).

It should be noted that the 2D case here is used only for demonstration purposes. It does not reflect the geometrical and physical properties of any stormwater system. For example, the 2D geometry in this case does not model the 2D slice in a cylindrical coordinate system.

The geometry and boundary conditions of the 2D model are described in Figure 23-1. The height D of the main tunnel was 0.8 m, and L_1 and L_2 were 4.0 m and 2.0 m, respectively. The width d_s and length L_s of the vertical shaft were 0.1 m and 3.0 m, respectively. A box with open boundaries were added on the top of the vertical pipe in the model to visualize the geysering after overflow (Figure 23-1), of

Table 23-1. Parameters Used in the First Geysering Simulation

Flow conditions	Items		Reference
	System based on	Large-scale lab model	Huang (2017)
	Geometry	Figure 23-1	
	Dimensions	6.1 m × 5.8 m	
	Water level	2 m	
	Air pressure head	2 m	
Model information	Simulation	Method or Governing Equation	Reference
	Type	RANS	ANSYS CFX theory guide
	Flow	N-S equation	
	Turbulence model	SST *k*-omega	
	Two-phase flow model	VoF	
Software used	Type of Software	Name of Software	Availability
	Geometry building tool	Workbench Geometry	Commercial
	Meshing tool	Workbench Mesh	Commercial
	Solver	ANSYS CFX	Commercial
	Postprocessing tool	ANSYS CFD POST	Commercial
Computational information	Items		Remarks
	Computational grid	Multiple-block, about 32,000 nodes and 15,000 cells	To capture the characteristics of film flow around the vertical pipe wall, grids need to be refined
	Time step	Adaptive time step, max. 10^{-4} s, min. 10^{-5} s	If the time step is larger than 10^{-4} s, the converged solution may be far from physical results
	Computing device	Intel Xeon E5-2680 v4, 32 cores	
	Computing time	~23 h	

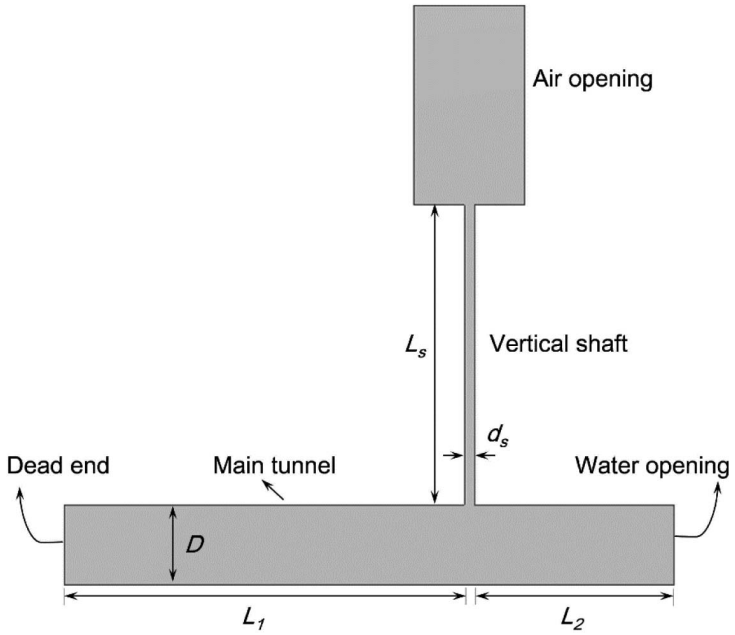

Figure 23-1. Schematic drawing of the CFD model.

which the width and height were 1 m and 2 m, respectively. The left end of the main tunnel was set as a no-slip wall, and the right opening was set for water with a certain pressure distribution. No-slip conditions were set for other solid walls. The initial height of the water column in the vertical shaft was set as 2 m.

23.4 RESULTS AND DISCUSSION

23.4.1 Air-Water Kinematics

For cases with continuous air release under a constant pressure head, the front shape of the entrapped air approximates the Taylor bubble (large bubbles rising through liquids in vertical tubes, which roughly has a velocity equal to $0.35\sqrt{gD}$ where g is the gravitational acceleration and D is the diameter of the tube, as reported in Davies and Taylor (1950), as shown in Figure 23-2. The air–water interface almost maintains that profile, along with the release process, until the interface breaks. However, asymmetry can be observed in Figure 23-2, which indicates the slight difference between film flows on each side.

The comparison of air–water movements between a short-column model in Huang (2017) and the present CFD model is given in Figure 23-3. Because the second short-column model (SCM2) of Huang (2017) was developed on the

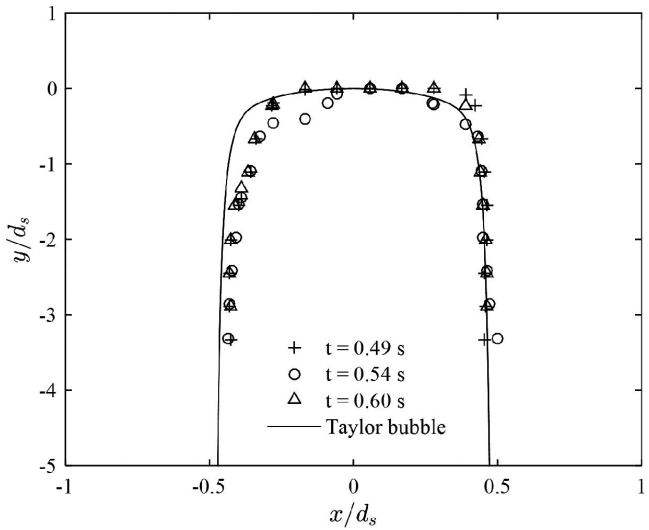

Figure 23-2. Comparison between the air–water interface and the Taylor bubble for a case with continuous air release.

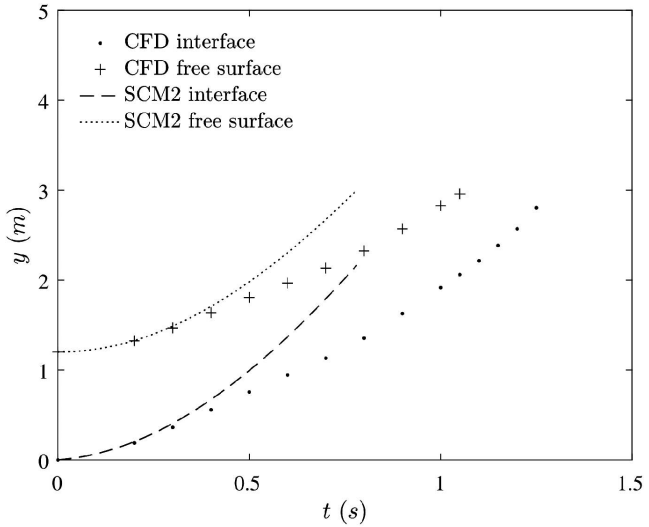

Figure 23-3. Comparison of the free surface and the air–water interface movements between the short-column model from Huang (2017) and the CFD model.

assumption that the entrapped air in the main tunnel was under a constant driving pressure and with a volume adequately large, the velocities of the free surface and the air–water interface were notably larger than those computed by the CFD model.

Thus, there is a certain gap between the duration from the air rising at the bottom to the water overtopping. Figure 23-3 shows clearly that in both these models the water column length reduces over the geysering process, which can be attributed to film flows. Nevertheless, the influence of film flows on the air–water movements should be related to the initial length of the water column within the vertical shaft and the driving pressure head of the entrapped air. Geyser heights can be estimated from the final interface velocity as a first approximation. It follows that the geyser height can be estimated as $H_g = V_f^2/(2g)$, where V_f = the final velocity of the air–water interface, and g = gravity acceleration.

The evolution of geysering induced by air release is illustrated in Figure 23-4. The initial condition is shown in Figure 23-4a, with entrapped air of length $L_{a0} = 3$ m in the main tunnel. The flow moves like gravity currents initially, and when the air pocket arrives at the base of the vertical shaft, it rises. A first geyser event can be observed in Figure 23-4d, which shows the short column jets in Huang (2017). After the air–water interface breaks, the pressure drops within the air pocket, causing water acceleration downstream, which introduces inertia surge to the flow system. Inertia-surge-induced jets, as shown in Figure 23-4f, could be related to transient pressure values and the air–water mixture. Because of the contribution of air–water mixing effects during the air release process described here, air–water mixture jets can be generated (Figure 23-4h). The mechanism of this kind of geysering is similar to that of an air-lift pump, as proposed in Huang (2017).

23.4.2 Pressure Oscillations

During the geysering process, the system undergoes pressure oscillations, as shown in Figure 23-5. For the case with a constant pressure head upstream, the initial pressure is conserved until air rises along the vertical shaft. After the air–water interface breaks, the pressure decreases significantly because of air flow. Pressure oscillations follow because of the inertia surge of water, and damping behaviors are observed then. It is worth noting that pressure peaks over such processes may contribute to geysers of great height.

23.5 SECOND GEYSERING SIMULATION

The second geysering model was created with an open-source CFD platform, OpenFOAM, in versions of both 4.0 (OpenFOAM Foundation 2016) and 1606 (OpenCFD 2016). To describe the unsteadiness and compressibility of geysering events, the compressibleInterFOAM solver in OpenFOAM was used to solve the Reynolds-averaged Navier-Stokes equations. The air–water interface was tracked with the VoF method, and the k-ε model was adopted to resolve the turbulence.

The geometry and boundary conditions of the current 3D models are described in Figure 23-6. The horizontal tunnel has a length of 62 m and a diameter (D) of 1 m, containing the upstream inlet and the downstream outlet. A vertical ventilation shaft, with the diameter (D_s) of 0.5 m, is located 30 m

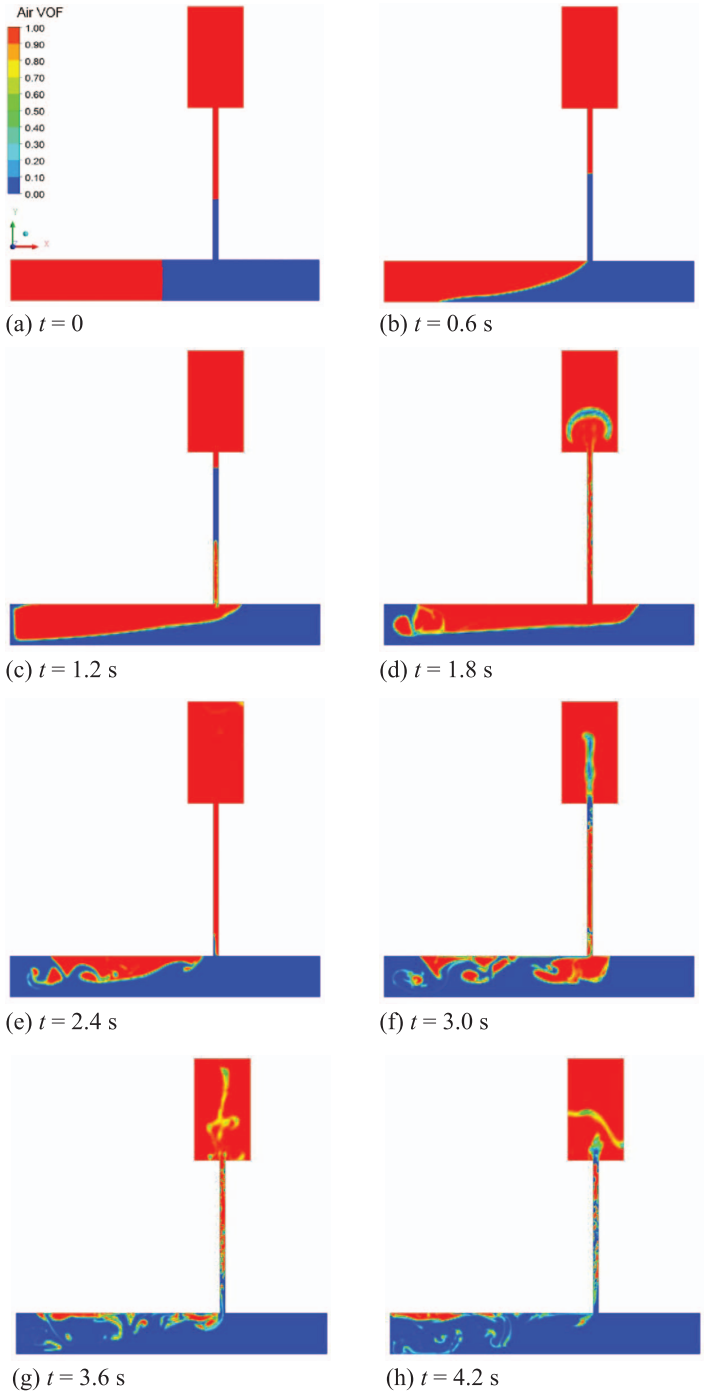

Figure 23-4. The geysering process induced by air expulsion through the vertical shaft (the color represents the air volume fraction).

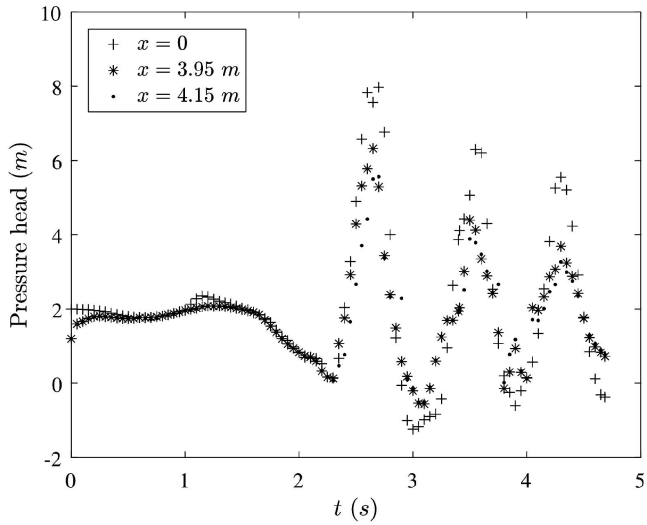

Figure 23-5. Pressure oscillations examined at different locations of the main tunnel crown for the case with air pocket length $L_{a0} = 3$ *m (x is measured from the leftmost point of the model).*

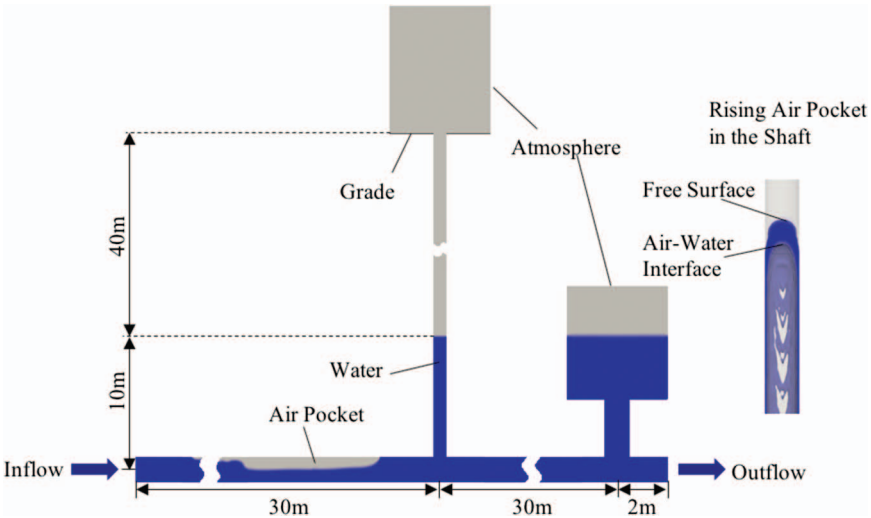

Figure 23-6. CFD model geometry and boundary conditions.
Source: Wang and Vasconcelos (2018).

downstream from the tunnel inlet. Above the vertical shaft, a 4 m diameter, 15 m height cylindrical open boundary was added to investigate geysering after overflow. A 4 m diameter downstream reservoir, open to the atmosphere, is located 2 m upstream from the tunnel outlet to maintain pressure. To reduce

computational costs, a 1 m diameter vertical pipe is used to connect the tunnel and the reservoir. All the wall boundaries are set up with the same roughness as smooth concrete. The initial water elevation in both the vertical shaft and the reservoir is at 10 m. A constant ambient flow velocity (V_a) in the tunnel is set up as 1.566 m/s, which corresponds to $0.5\sqrt{gD}$.

This series of simulations aim to investigate the flow characteristics when a single air pocket is released versus a sequence of smaller pockets with spatial separation. In the current model, a total volume of air pocket of 20 m^3 is released from the inlet with various patterns for different scenarios, including one air pocket of 20 m^3, two air pockets of 10 m^3 each, and four air pockets of 5 m^3 each, following these steps:

1. The inlet boundary is set up as the air phase inlet for a duration of t_0 to release the first air pocket;
2. The inlet boundary is then set up as the water phase inlet for a duration of t_1 to separate the first and the second air pockets with a distance of $L_1 = t_1 \times V_a$, while the first air pocket develops as gravity current and propagates downstream;
3. Repeat Steps 1 and 2 until the total volume of air pocket is completely released and the inlet boundary is then set up as a constant water phase.

The details of the flow condition setup are listed in Table 23-2.

The mesh of the current models was generated with blockMesh and snappyHexMesh utilities in OpenFOAM. The former is a basic mesh generation utility for creating mesh with blocks, and the latter is a polyhedral mesh generation utility that creates mesh by cutting and morphing existing mesh to fit the calculation boundaries. To reduce the computation costs, a symmetric model was used so that the total mesh number was decreased by a factor of two. The simulations were

Table 23-2. Flow Condition Setup of the Second Geysering Simulation

Scenarios	*V5*	*V10*	*V20*
Total volume of air pocket (m^3)		20	
Volume of single air pocket (m^3)	5	10	20
Number of air pockets being released	4	2	1
Ambient flow velocity (V_a) (m/s)		1.566	
Duration (t_0) of the releasing of each air pocket (s)	4.07	8.14	16.28
Duration (t_1) between every two air pockets being released (s)	8.14	16.28	NA
Distance separation (L_1) between every two air pockets (m)	12.75	25.49	NA
Initial water elevation in the system (m)		10	

Source: Wang and Vasconcelos (2018).

conducted in the High Performance Community Computing Cluster at Auburn University. The details of the model setup are listed in Table 23-3.

23.6 RESULTS AND DISCUSSION

23.6.1 Air-Water Kinematics

Figures 23-4g and h and 23-5 show that after the release of an air pocket, the ventilation shaft is filled with a complex air–water bubbly mix, accompanied by an inertial surge of water. After a single air pocket is released, the discrete bubbles keep migrating upward and finally are completely released without any interaction with a new air pocket release. In comparison, when a sequence of air pockets is released, the bubbly mix and inertial surge of water may get a chance to interact with a newly released air pocket. The current model aims to investigate the flow characteristics of such interactions.

Figures 23-7 and 23-8 present the displacement and velocity evolution of the air–water interface, denoted by IF, and water free surface, denoted by FS, in the ventilation shaft, respectively. Time $t = 0$ corresponds to the moment when the first air pocket arrives at the shaft junction. The air–water interface and the water free surface can only be clearly tracked for the release of the first air pocket because of the bubbly mix of water and air after the first release. Intuitively, it is possible to guess that for larger air pockets released, volumes of the free surface will be further displaced upward. Also, for the release of larger air pockets, it is anticipated that the air–water interface and the water free surface would achieve higher displacement velocities. However, the fact of no significant difference between the scenarios V10 and V20 in Table 23-2 indicates that air pocket volumes have impacts on the water displacement up to a certain point, after which the air pocket size is sufficiently large compared to the displaced water volume in the tower.

Figure 23-9 shows the evolution of maximum elevation of the water phase, among which the water mist with a volume fraction greater than 0.1 is considered. The result of scenario V5 in Table 23-2 shows that the water and water mist can be displaced only up to 38.8 m by the first air pocket, yet the displacement can be 57.1 m for the second release, 53.4 m for the third one, and 49.3 m for the fourth one. Such observation can be attributed to the smaller inertia and the existence of more water mist after the first air pocket is released. However, the highest water and water mist elevation induced by the second air pocket release is lower than the one induced by the first one for scenario V10 in Table 23-2 because the longer separation of air pockets results in more expelling of bubbles from the water phase. Figure 23-10 shows a 3D snapshot of a simulated geyser triggered by the release of an air pocket.

23.6.2 Pressure Oscillations

Figure 23-11 presents the pressure oscillation results of a variety of air pocket release simulations. Comparing the results of scenarios V10 and V20, we notice

Table 23-3. Parameters Used in the Second Geysering Simulation

Flow conditions	Items		Reference
	Geometry	Figure 23-6	Wang and Vasconcelos (2018)
Model information	Simulation	Method or Governing Equation	Reference
	Type	RANS	Svenungsson (2016), OpenFOAM User Guide (2016)
	Flow	N-S equation	
	Two-phase flow model	VoF	
	Turbulence model	k-ε	
Software used	Type of Software	Name of Software	Availability
	Geometry building tool	FreeCAD and MeshLab	Open source
	Meshing tool	blockMesh and snappyHexMesh utilities	
	Solver	compressibleInterFOAM	
	Postprocessing tool	Probe utility and ParaView	
Computational information	Items		Remarks
	Computational grid	Polyhedral mesh with about 1.87 million cells	Cells in the shaft and close to the boundary are refined
	Time step	Adaptive time step	Most between 10^{-6} and 10^{-5} s
	Computing device	Hopper Cluster at Auburn University	
	Number of processors	200	
	Computing time	~12 days	

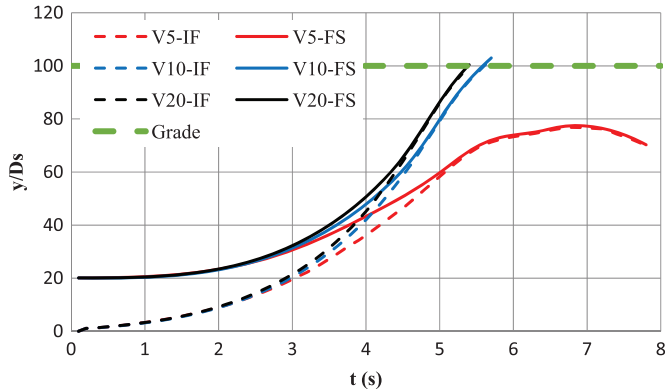

Figure 23-7. Evolution of a normalized air–water interface (IF) and water free surface (FS) displacements.
Source: Wang and Vasconcelos (2018).

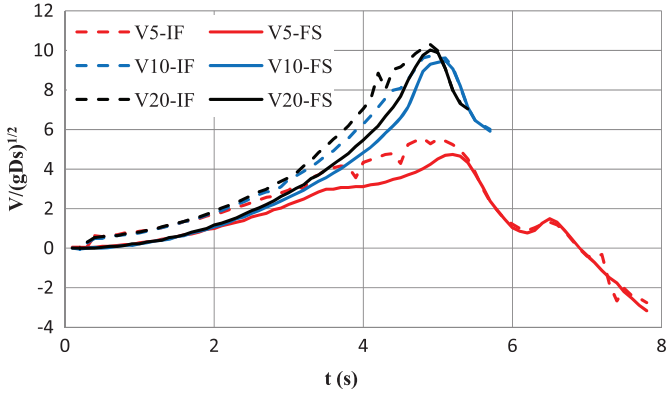

Figure 23-8. Evolution of a normalized air–water interface and water free surface velocities.
Source: Wang and Vasconcelos (2018).

that the release of the first air pocket generates a similar pressure oscillation pattern. However, it cannot be explained that a pressure spike appears at $t = 7.1$ s for scenario V10. It is interesting to find that in scenario V5, the magnitude of the pressure oscillation is magnified by the sequence of the air pocket release, whereas the first air pocket can cause only about half the value of the pressure oscillation magnitude caused by the following ones. In contrast, the pressure oscillation magnitude of scenario V10 was not magnified by the second released air pocket, which can also be attributed to the longer separation of the two air pockets. Clearly, this conclusion cannot be generalized because it is conditioned on the geometry that was evaluated in this work.

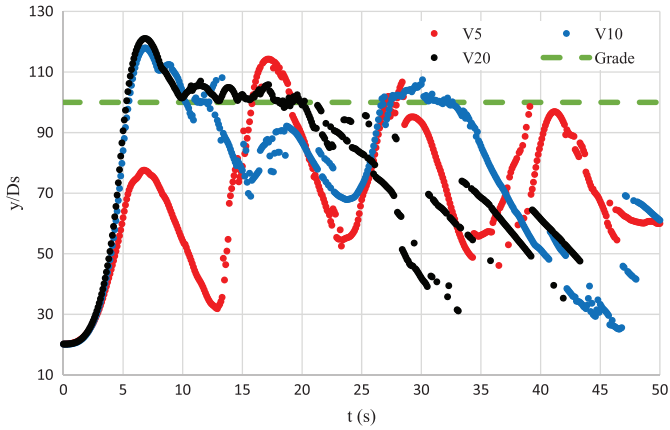

Figure 23-9. Evolution of normalized maximum elevation of water and water mist.
Source: Wang and Vasconcelos (2018).

Figure 23-10. Geyser overflow created by the release of an air pocket (volumetric fraction greater than 0.1).

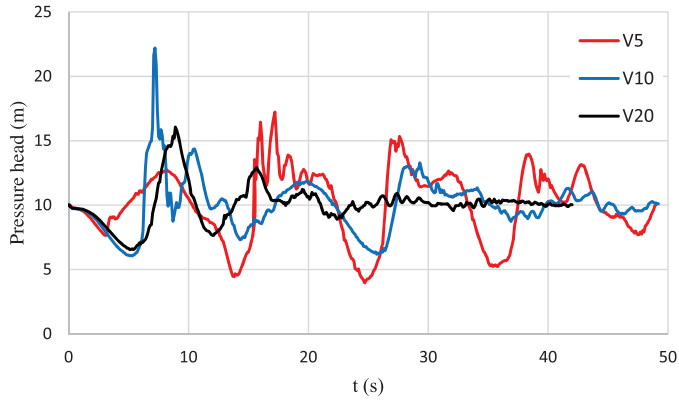

Figure 23-11. Pressue oscillations monitored at the bottom of the ventilation shaft.
Source: Wang and Vasconcelos (2018).

23.7 CONCLUSIONS AND FUTURE STEPS

Given all the geometric constraints associated with this work, the following conclusions are supported by the findings of the first simulation for sewer geysering:

- A detailed evolution process of sewer geysering was obtained using CFD techniques, of which air–water interactions were captured because they are useful to advance our understanding of geyser events. A few types of geysering jets were observed, which might be driven by various mechanisms, not proposed in earlier studies using 1D models.
- Extreme conditions can be conveniently implemented in CFD models, and pressure transients can be registered at almost all available points in the model. These variabiles provide the possibility to monitor the system pressure over the geysering process.
- Retrofit measures should be easily tested using CFD tools for existing urban drainage systems.

Likewise, the following conclusions are supported by the findings of the second model:

- The release of a single large air pocket can cause significant water displacement in the shaft and can create a geyser, accompanied by a large magnitude of pressure oscillation, and the release of a sequence of smaller air pockets is able to generate a sequence of geyser events.
- When the volume of each air pocket is small, but the separation of the air pockets is not too significant, the water displacement and pressure oscillation can be magnified by a sequence of air pocket releases. Since geysers are often visualized as a sequence of events (Wright et al. 2011) similar to scenario V5,

it is promising to use the CFD approach to study geysers for real stormwater management practice.

All of these conclusions are based on the simulated geometries in this work. It is difficult to achieve general conclusions on geyser occurrences since geometry is of paramount importance in these occurrences. Currently, various efforts are ongoing to obtaining further insights on geysering processes involving physical and numerical modeling. CFD tools have been helping to obtain a better understanding of these events. This type of numerical modeling assists designers to achieve safer design for stormwater structures, particularly vertical inflow and ventilation shafts, to prevent negative effects of uncontrolled air pocket release and geysering events.

References

Davies, R. M., and G. I. Taylor. 1950. "The mechanics of large bubbles rising through extended liquids and through liquids in tubes." *Proc. R. Soc. London Ser. A* **200** (1062): 375–390.

Guo, Q., and C. C. S. Song. 1991. "Dropshaft hydrodynamics under transient conditions." *J. Hydraul. Eng.* **117** (8): 1042–1055.

Hirt, C. W., and B. D. Nichols. 1981. "Volume of fluid (VOF) method for the dynamics of free boundaries." *J. Comput. Phys.* **39** (1): 201–225.

Huang, B. 2017. "Hydraulics of Geysering flow in urban drainage systems." Ph.D. dissertation, Nanjing, China: Department of Hydraulic Engineering, Nanjing Hydraulic Research Institute.

Klaver, P., D. Collins, K. Robinson, and S. Bell. 2016. "Modeling of transient pneumatic events in a combined sewer overflow storage tunnel system." *J. Water Manage.* Model, V25:C409. Accessed April 19, 2019. https://doi.org/10.14796/JWMM.C409

Leon, A. S., M. S. Ghidaoui, A. R. Schmidt, and M. H. García. 2006. "Godunov-type solutions for transient flows in sewers." *J. Hydraul. Eng.* **132** (8): 800–813.

Leon, A. S., M. S. Ghidaoui, A. R. Schmidt, and M. H. Garcia. 2010. "A robust two-equation model for transient-mixed flows." *J. Hydraul. Res.* **48** (1): 44–56.

Li, J., and A. McCorquodale. 1999. "Modeling mixed flow in storm sewers." *J. Hydraul. Eng.* **125** (11): 1170–1180.

Muller, K. Z., J. Wang, and J. G. Vasconcelos. 2017. "Water displacement in shafts and geysering created by uncontrolled air pocket releases." *J. Hydraul. Eng.* **143** (10): 04017043.

OpenCFD. 2016. OpenFOAM User Guide, v.1606+, July. Bracknell, UK: ESI Group.

OpenFOAM Foundation. 2016. OpenFOAM User Guide, v. 4.0, June, London: OpenFOAM Foundation.

Politano, M., A. J. Odgaard, and W. Klecan. 2007. "Case study: Numerical evaluation of hydraulic transients in a combined sewer overflow tunnel system." *J. Hydraul. Eng.* **133** (10): 1103–1110.

Song, C. C. S., J. A. Cardie, and K. S. Leung. 1983. "Transient mixed-flow models for storm sewers." *J. Hydraul. Eng.* **109** (11): 1487–1504.

Svenungsson, J. 2016. *Solving electric field using Maxwell's equations and compressibleInterFOAM solver*. Göteborg, Sweden: Chalmers Univ. of Technology.

Vasconcelos, J. G., and G. M. Leite. 2012. "Pressure surges following sudden air pocket entrapment in storm-water tunnels." *J. Hydraul. Eng.* **138** (12): 1081–1089.

Vasconcelos, J. G., and S. J. Wright. 2003. "Surges associated with air expulsion in near-horizontal pipelines." In *Proc., ASME JSME Joint Fluids Engineering Conf.*, 2897–2905. New York: American Society of Mechanical Engineers.

Vasconcelos, J. G. and S. J. Wright. 2006. "Mechanisms for air pocket entrapment in stormwater storage tunnels." In *Proc., World Environmental and Water Resource Congress 2006: Examining the Confluence of Environmental and Water Concerns*, 1–10. Reston, VA: ASCE.

Vasconcelos, J. G., and S. J. Wright. 2009. "Investigation of rapid filling of poorly ventilated stormwater storage tunnels." *J. Hydraul. Res.* **47** (5): 547–558. Accessed April 19, 2019. https://www.tandfonline.com/doi/pdf/10.3826/jhr.2009.3390?needAccess=true.

Vasconcelos, J. G., and S. J. Wright. 2011. "Geysering generated by large air pockets released through water-filled ventilation shafts." *J. Hydraul. Eng.* **137** (5): 543–555.

Vasconcelos, J. G., S. J. Wright, and P. L. Roe. 2006. "Improved simulation of flow regime transition in sewers: Two-component pressure approach." *J. Hydraul. Eng.* **132** (6): 553–562.

Wang, J., and J. G. Vasconcelos. 2018. "Geysering episodes created by the release of a sequence of discrete air pockets in vertical shafts." In *Proc., 2018 ASCE-EWRI Congress*. Reston, VA: ASCE.

Wright, S. J., J. W. Lewis, and J. G. Vasconcelos. 2011. "Physical processes resulting in geysers in rapidly filling storm-water tunnels." *J. Irrig. Drain. Eng.* **137** (3): 199–202.

Zhou, F., F. E. Hicks, and P. M. Steffler. 2002. "Transient flow in a rapidly filling horizontal pipe containing trapped air." *J. Hydraul. Eng.* **128** (6): 625–634.

APPENDIX: MODELING INSTRUCTIONS

Modeling using ansys CFX

ANSYS CFX v18.0 was used in this study, and detailed descriptions of governing equations for the homogeneous VoF method and the SST model can be found in the CFX theory guide.

Steps

1. Design the geometry in Workbench Geometry or build one using other tools (e.g., SpaceClaim);
2. Generate mesh using Workbench Mesh or another software; check the mesh quality to ensure no error messages when it is used to compute;
3. Set up all the boundary and initial conditions in ANSYS CFX-Pre, use CFX Command Language (CCL) if necessary; set up monitoring points and other options of interest; save data at specified time intervals for unsteady simulations;
4. Run the case in CFX Solver; double check with the prompt messages;
5. Perform postprocessing with CFX Post; visualize the results and export a report about the simulation.

Modeling using OpenFoam

To perform the simulation of a geyser in this chapter with OpenFOAM, the following steps can be used:

1. Create a simulation case by copying the compressibleInterFOAM tutorial;
2. Adjust the boundary condition, initial condition, and turbulence model, as well as the algorithms and other parameters, such as Courant Number;
3. Create a 3D geometry of the interested system with the CAD modeler in STL format, and split the geometry into several files, each one containing one type of the flow field boundary;
4. Generate the background mesh with blockMesh utility and then create the mesh with snappyHexMesh utility by using the STL files from step 3;
5. Double check and modify (if needed) the boundary types for the generated mesh;
6. Run the simulation with compressibleInterFOAM solver, during which the Courant number may need to be adjusted;
7. Perform postprocessing with OpenFOAM utilities, such as the probe utility for pressure monitoring, and in ParaView's application for visualization.

This page intentionally left blank

Index